THE UNIVERSITY *of* EDINBURGH

First-principles studies of gas hydrates and clathrates under pressure

Pattanasak Teeratchanan

Doctor of Philosophy
The University of Edinburgh
November 2017

Abstract

Gas hydrates are molecular host-guest mixtures where guest gas species are encapsulated in host water networks. They play an important role in gas storage in aqueous environments at relatively low pressures, and their stabilities are determined by weak interactions of the guest species with their respective host water frameworks. Thus, the size and the amount of the guest species vary, depending on the size of the empty space provided by the host water structures. The systems studied here are noble gas (He, Ne, Ar) and diatomic (H_2) hydrates. Because of the similarity of the guests' sizes between the noble gases and the di-atomic gases, the noble gas hydrates act as simple models for the di-atomic gas hydrates. For example, He, Ne and H_2 have approximately the same size.

Density functional theory calculations are used to obtain the ground state formation enthalpies of each gas hydrate, as a function of host network, guest stoichiometry, and pressure. Dispersion effects are investigated by comparing various dispersion corrections in the exchange-correlation functionals (semi-local PBE, semi-empirical D2 pair correction, and non-local density functionals i.e. vdW-DF family). Results show that the predicted stability ranges of various phases agree qualitatively, although having quantitative difference, irrespective of the methods of the dispersion corrections in the exchange-correlation functionals. Additionally, it is shown in gas-water dimer interaction calculations that all DFT dispersion-corrected functionals overbind significantly than the interaction acquired by the coupled-cluster calculations, at the CCSD(T) level, which is commonly accepted to provide the most accurate estimation of the actual interaction energy. This could lead to an overestimation of the stability of the hydrate mixtures. Further study in the gas-water cluster indicates that less overbinding effect is found in the cluster than in the dimer. This implies that the overbinding energy caused by DFT might become less pronounce in the solid phase.

Graph invariant topology and a program based on a graph theory are used to assign protons based on the "ice rule" to fulfill the incomplete experimental structural data such as unknown/unclear positions of protons in the host water lattices. These methods help constructing host water networks for computational calculations. Several configurations of the host water structures are tested. Those configurations having lowest enthalpies are used as the host water networks in this research. Furthermore, the enthalpic spread between the configurations having the highest and the lowest enthalpy in the pure water ice network is very small (about 10 meV per water molecule). Nevertheless, it is still unclear to conclude that this protonic effect is also trivial in the gas-water compound. Therefore, this study also calculates the enthalpies of the gas-water mixtures having various proton configurations in the host water networks. Results indicate that very small enthalpic distributions among the proton configurations are found in the compounds as well. Furthermore, the enthalpic spread is almost constant as pressure increases. This suggests there is no pressure effect in the enthalpy gap amoung the proton distributions in both pure water ice and the gas-water compounds.

Predicted stable phases for the noble gas compound systems are based on four host water networks, namely, ice I_h, II and I_c, and the novel host water network S_χ. The He-water system adopts ice I_h, II and I_c network upon increasing pressure. In the Ne-water system, a phase sequence of S_χ/ice-I_h, II and I_c with a competitive hydrate phase in the S_χ host network at very low pressure is found. This is similar to the phase evolution of the H_2-water system. For the Ar-water mixture, only a partially occupied hydrate in the S_χ host network is found stable. This S_χ phase becomes metastable if taking the traditional clathrates (sI and sII) into account. This result agrees very well with the experiment suggesting only two-third filling is found the large guest gases i.e. CO_2.

For the diatomic guest gas compound systems, the traditional clathrate structure (sII) that found to be existed experimentally in the H_2-H_2O system is also included in this study together with those four host water networks. Predicted phase stability sequence as elevated pressure is as follows: S_χ, ice-I_h, II and I_c. This computationally prediction agrees very well with experiment. Results in this work suggest that the compound based on the traditional clathrate structure II (sII) host water framework is found to be metastable with respect to the decomposition constituents - in this case, they are pure water ice and the S_χ. The metastability of the hydrogen hydrates based on the sII structure might due

to zero-point motions or other dynamic/entropic mechanisms uncovered in this research.

Dynamic studies concerning the transition states of the hydrogen guest molecules in three competitive phases at very low pressure (less than 10 kbar), based on S_χ, ice-I_h, and ice-II host water network, are considered. The energy barriers required by the hydrogen guest molecules in those three host frameworks are calculated by using Nudged Elastic Band (NEB) method. Results suggest that the hydrogen molecules are more mobile in the S_χ than the other two host structures significantly. In the S_χ host water network, the energy barrier is about 25 meV/hydrogen molecule. This energy is about the room temperature suggesting that the hydrogen guest molecules are easily mobile in the S_χ host water network if there is an empty site adjacent to them.

Declaration

I declare that this thesis was composed by myself, that the work contained herein is my own except where explicitly stated otherwise in the text, and that this work has not been submitted for any other degree or professional qualification except as specified.

Parts of this work have been published in [153].

(*Pattanasak Teeratchanan, November 2017*)

Acknowledgements

First and foremost, I would like to express my immeasurable appreciation and deepest gratitude to my supervisor Dr. Andreas Hermann for all his support, guidance, and encouragement over the years. All of these have contributed in making this Ph.D. study possible.

I am also grateful to all the staffs of the University of Edinburgh, especially, Dr. Graeme Ackland, Dr. Ingo Loa, and Dr. Miguel Martinez-Canales, for their comments and suggestions over the years.

I am profusely thankful to Dr. John Loveday and Dr. Mary-Ellen Donnelly for sharing their experimental data and innovative ideas on the gas hydrates.

I would also like to thank colleagues and friends at the University of Edinburgh. In particular, my office mates and research mates, Victor Naden Robinson and Harry Keen for their chats and making the office lively.

I am extremely thankful to the members of the commitee for the viva. Dr. John Loveday and Dr. Stewart Clark for their comments and ideas during the interview.

I am particularly indebted to my parents and sister, who always support and encourage me during my study.

Special thanks to Rory Mckenzie, who helps me proofread this thesis.

Last but not least, I would like to express the foremost gratitude to the Royal Thai Government for providing the sponsorship during my Ph.D. study.

Contents

List of Figures

List of Tables

Chapter 1

Aim of Thesis

This thesis mainly focuses on the water-gas compounds under pressure, in particular small guest gases such as noble gases (helium, neon and argon) and hydrogen. The outline of this thesis is as follows:

Chapter 2 presents general overviews of the known host water networks. These host structures are suitable to accommodate the guest gas species. Two different types of host water networks are introduced. First, the water structures, which are based on pure ice structures. Second, the "host-guest" frameworks named "clathrate", which form "cage-like" structures.

Chapter 3 describes the fundamental theories, especially in computational methods. Both wavefunction-based and density-based methods are explained in details in order to solve the complicated many-body equations. Additionally, several vdW-corrected DFT functionals are also discussed.

Chapter 4 focuses on more details on the electronic structure calculations in a periodic system, i.e. plane wave basis set, cutoff energy, k-point sampling, pseudopotentials. Parameters used in the calculations in this thesis are presented.

Chapter 5 concerns about the effect of different proton configurations in water ice networks. Two graph-based programs used to assign protons to form a complete ice network are described. Enthalpy results of different protonic configurations in various water ice phases are analysed.

Chapter 6 contains the results of the noble gas hydrates (He, Ne, and Ar). DFT is used to calculated the enthalpy of each phase in the noble gas hydrate

compounds. Stoichaiometry tests are conducted by varying the guest occupancy number. Finally, several vdW-corrected functionals available in VASP code are tested and compared.

Chapter 7 is dedicated to the computational works on the H_2-H_2O system. Both static and dynamic studies are performed in this chapter. In the static part, enthalpies of various hydrogen-water phases in this system are calculated. Thus, for each DFT functional, we can propose the predicted phase diagram based on these enthalpy results. For the dynamic study, NEB calculations are performed to obtain the energies required for moving hydrogen guest molecules in certain pathways in different host water ice structures.

Chapter 2

Different ice and clathrate phases

This chapter describes two main types of host water networks. One is based upon the currently known water (ice) phases. Owing to the varieties of water ice polymorphs, different cavity sizes are formed. The cavity size determines on which species the guest gases can be. Small guest gas species such as hydrogen, helium, neon are commonly found to adopt the host water ice networks. However, larger guest gas species require bigger cavity sizes and hence they cannot accommodate in the empty space created by the water ice frameworks. Thus, another type of the host water network in the gas-water compound system, which has larger cavity sizes, is needed.

The other type of the host water network adopts the open cage-like structures called "clathrate", in which the host lattices are water molecules. Cavities formed by these host water molecules are capable of encapsulating certain guest gas species such as methane, ammonia and argon. Clathrate hydrates having empty cavities are typically unstable compared to other polymorphs of ice, the presence of the guest gases inside the cavities help stabilising the overall interactions resulting in the stability of the water-gas compounds.

2.1 Water Ice Phases

Water is ubiquitous and is vital to all forms of life. Up to 60% of the human adult body is water. The Earth is a watery planet, around 71% of the Earth's surface is water-covered. Despite we commonly experience water in all three states of

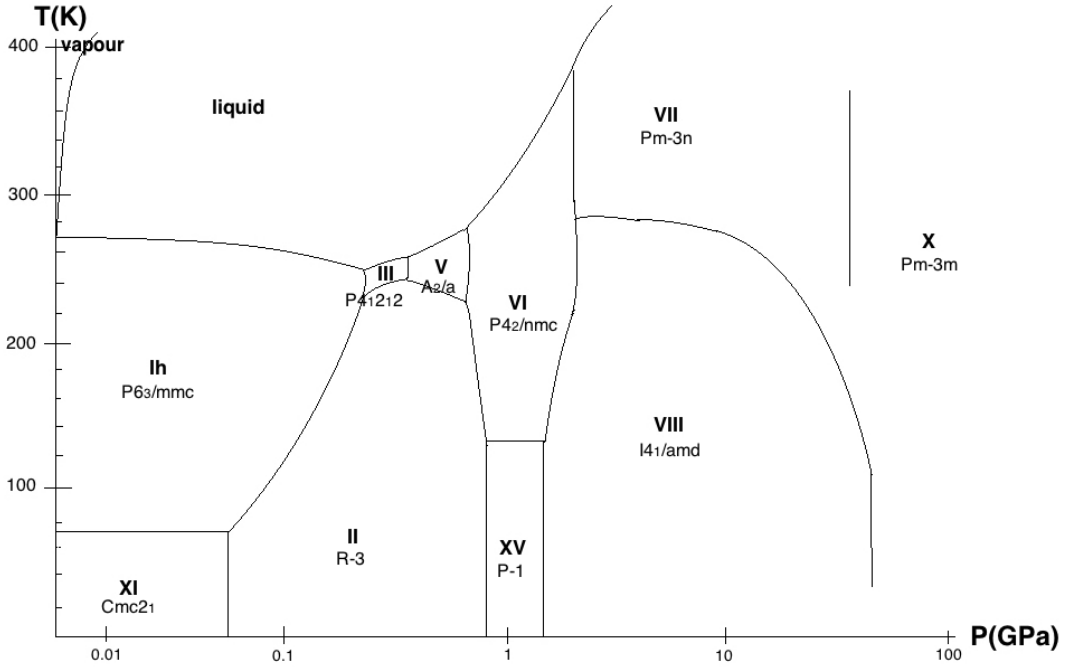

Figure 2.1 *Phase diagram of stable water phases as a function of pressure in (logarithmic scale) and temperature (in linear scale). For the solid state, ten ice polymorphs are represented in Roman numerals, their space groups are displayed underneath. The liquid and gas phase are shown on the top left. Metastable polymorphs are omitted in this picture. Adapted from the lecture note by Fuentes-Landete et al. [46].*

matter: solid, liquid, and vapour at a relatively narrow range of temperature and pressure, many of its properties have remained elusive, especially at extreme conditions. A pressure-temperature (P-T) phase diagram of water is depicted in Figure 2.1. As illustrated in Figure 2.1, the solid-liquid-vapour triple point occurs at T = 273.16 K, P = 612 Pa. The liquid and gas phase of water are separated by a coexistence line, which starts from the solid-liquid-vapour triple point (mentioned earlier) and ends in the liquid-vapour critical point at T = 647.10 K and P = 22.1 MPa [70]. Whilst there is only one vapour phase, it is still unclear how many solid phases of water can be distinguished. Vast varieties of solid state phases have been explored and introduced to the idea of polymorphism [14].

Emerging from the solid-liquid-vapour triple point, the melting line of water has a negative slope. When the melting curve is negatively sloped, the process of pressure-induced melting happens, i.e. the ice cube (ice I_h) will melt when applying pressure. At higher pressure, the melting line suddenly becomes

positively sloped at T = 251 K, P $\sim$ 210 MPa, hence from this point on the process of presure-induced crystallization takes place. A previously pressure-molten ice cube kept at T = 255 K will refreeze again if applying pressure exceeds 300 MPa. However, it will not crystallize to common hexagonal ice (ice I_h), another polymorph of water ice (ice III) will form instead [81, 101, 111]. Similarly, another polymorph of ice (ice V) will form if pressurising an ice cube (ice I_h) kept isothermally at T = 263 K. This ice cube will melt at P 100 MPa, and will eventually refreeze to ice V at P $\sim$ 450 MPa [6, 101].

Other ice polymorphs are found at higher pressure when the water phases undergo a pressure-induced transition. The crystallization of ice VI occurs when pressurising liquid water at ambient temperature to P $\sim$ 900 MPa [78]. Ice VII is found at P $\sim$ 20-40 GPa via the compression of hot stream at constant temperature, T = 800 K [73, 79, 86]. Finally, ice X or a superionic state, where the protons of ice VII are dynamically disordered, is discovered at T $>$ 1000 K, P $>$ 50 GPa [138]. For the ice X, the water molecules lose their molecular characters entirely. The protons situate exactly at the middle between the two oxygen atoms.

In summary, along the melting line of water, five solid-solid-liquid triple points have been clearly identified. The melting line of water is very well understood [19]. Hence, by tracing the abrupt change of the melting curve's slope, six different phases of ice are evidently indicated. Those six distinct phases of ice are ice I_h, Ice III, ice V, ice VI, ice VII, and ice X .

Additionally, below the melting line of water, there exist some solid-solid-solid triple points. Three solid polymorphs can coexist with the previously mentioned polymorphs. In particular, ice II [42, 44, 77, 80], ice VIII [35, 95], ice XI [52, 142, 152], ice XIII [134, 135], ice XIV [92, 134, 135], and ice XV [87, 133, 135] are found to exist in thermodynamic equilibrium with other polymorphs of ice.

Those solid-solid transitions, which are not involved in the transformation to an intermediate liquid state, must involve in either the rearrangement of the oxygen atoms' lattice (e.g. ice I_h transforms to ice II when pressurizing) [9] or be driven by the entropy to proton-ordering phases e.g. ice III transforms to ice IX when cooling [88, 101].

In Figure 2.1, there are other ice phases that are not included in the phase diagram of stable phases. These phases are metastable and may occur when the thermodynamically stable phases cannot be accessed easily due to kinetic

constraints. For example, the metastable ice IV [38] phase can be found from the pressurized liquid instead of the stable ice V phase and the metastable ice XII [92] phase can be formed when pressurising an amorphous solid state instead of the stable ice VI phase.

Cubic ice I_c, which is metastable, may be formed in the Earth's atmosphere [16] or may be obtained by heating other high-pressure ice-polymorphs at ambient pressure [54]. Both cubic ice I_c and the hexagonal ice I_h have very close free energies, approximately the same density of 0.92 g/cm^3 [162], the same interatomic distances. Thus it is very difficult to distinguish them when using a method sensitive to the local short-range molecular environment, i.e. vibrational spectroscopy. Therefore, both share the same name of ice "I" but have different subscripts. Diffraction techniques e.g. XRD or NRD can differentiate these two ice phases because they have different stacking sequences.

The ice phases are represented by Roman numerals in chronological order. All the previously mentioned ice phases are located within positive pressure regions. If the phase diagram is extended into the negative pressure range, there still exist some other ice polymorphs.

At present, three more ice phases are proposed under negative pressure. However, only two are experimentally proven namely ice XVI (which is equivalent to the empty structure of the sII clathrate hydrates [41]) and ice XVII (which is equivalent to the empty S_χ network [99]). Ice XVI was experimentally discovered by removing the neon gas molecules from a neon clathrate, based on the sII clathrate structure, under vacuum at temperature below 147 K [41]. Similarly, ice XVII was synthesized by removing the hydrogen gas molecules from a hydrogen hydrates, based on the S_χ structure, under vacuum at temperature $\sim$ 120 K [99].

More than eighteen phases of ice are reported so far. However, not all the ice phases are suitable for being the host structure in the gas-water compounds. Only the phases that have the cavity size large enough to accommodate the guest gas species comfortably can be the host water structures. At present, only ice I_h, ice I_c, and ice II are experimentally confirmed as the host networks in the gas hydrates, where their guest gases are hydrogen [165, 166], helium [102, 104, 105], and neon [176]. The guest gases having larger size than these require other types of host structure that can form larger cavity size, i.e. clathrate structures.

2.2 Clathrate Hydrates

Clathrate structure I (sI), and clathrate structure II (sII) are the most common forms of the host water networks in the gas hydrates. Both sI and sII are cubic. The sI structure has two different types of cages, 5^{12} and $5^{12}6^2$, which can be arranged to form a cubic sI structure (spacegroup $Pm\bar{3}n$, a $\sim$ 11.9 Å). The sI structure is composed of two 5^{12} and six $5^{12}6^2$ cages per unit cell, 46 water molecules. The water: guest ratio equals 46:8 or 5.75:1. Large gas species like CO_2 [75, 106] and CH_4 [75, 106] are typically found to adopt this sI structure, while mid-size and smaller guest gases like O_2 [159] and N_2 [96] and H_2 [103] are commonly found to form in the sII structure. Some guest gases, especially small ones, are observed to have multiple occupancy in the cages [96, 103, 140].

The sII structure is comprised of two different types of cages: 5^{12} and $5^{12}6^4$. These two types of cages are arranged so that they form a cubic sII structure (spacegroup $Pm\bar{3}n$, a $\sim$ 17.1 Å). The sII structure can be constructed by using sixteen 5^{12} cages and eight $5^{12}6^4$ cages, 136 water molecules per unit cell. The sII has a water: guest ratio of 136:24 or 5.66:1. Note that the water: guest ratios listed here are based on a single occupancy per cage within the structure.

Hexagonal clathrate structure (sH) and tetragonal clathrate (sT) structure are the two clathrate structures that have often been observed at high pressure [106]. The sH structure has three different types of cages: 5^{12}, $4^3 5^6 6^3$, and $5^{12}6^8$, which are arranged to form a hexagonal structure (spacegroup P6/mmm, a $\sim$ 12.2 Å, c $\sim$ 10.1 Å). The sH can be formed from three 5^{12}, two $4^3 5^6 6^3$, and one $5^{12}6^8$. There are 52 water molecules per unit cell. However, the $5^{12}6^8$ cage is very huge so that it can contain the guest species as up to eight atoms/molecules. Thus, the water: guest ratio is 3.5-4.0:1 [106]. Mid-size and large guest species are observed in this sH structure, e.g. N_2 and CH_4 [106]. Although, one of the cages in the sH structure is very huge ($5^{12}6^8$), not all large guest gas species can form in this structure. For example, there is no indications of CO_2 hydrate based on sH structure at pressure up to 4 GPa [2, 28, 66].

The sT structure has only one type of cage that is $4^2 5^8 6^4$. Its spacegroup is $P4_2mnm$ with lattice parameters a $\sim$ 6.3 Å and c $\sim$ 10.6 Å. The sT structure contains two cages and 12 water molecules per unit cell. Each cage can accommodate two guest species, resulting in the water:guest ratio of 12:4 or 3:1. Unlike the sH, which has been observed in the systems that adopt both sI and

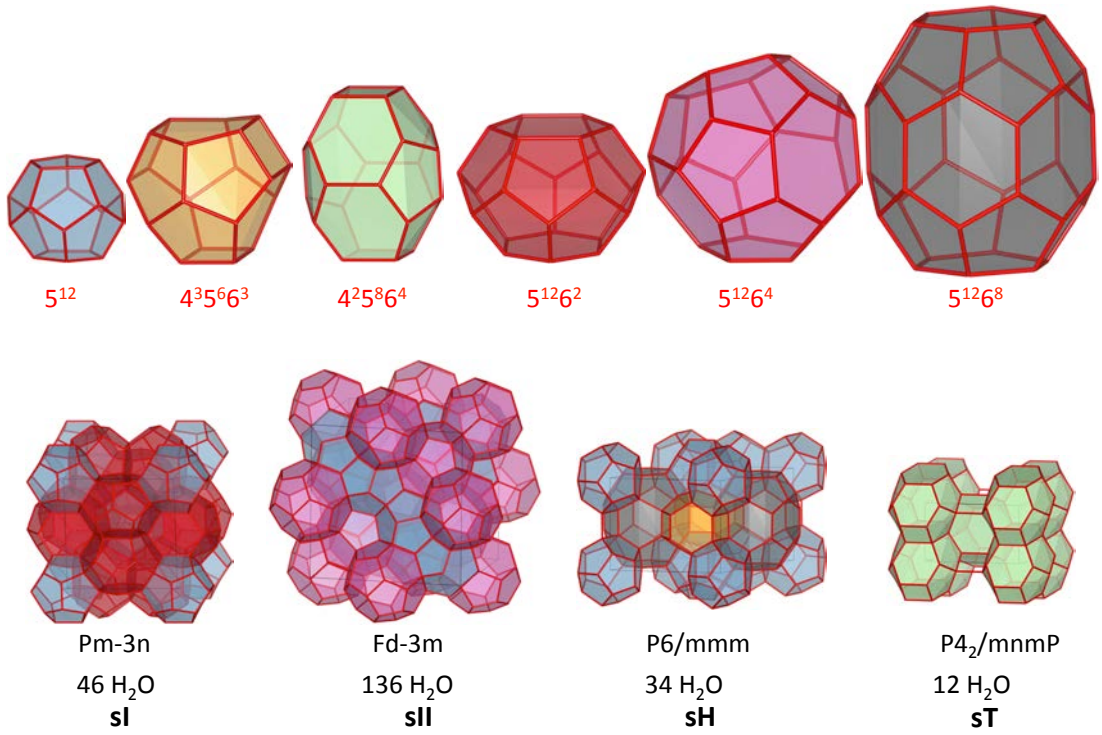

Figure 2.2 ***Top:*** *Empty cage structures of different sizes and shapes. The numbers listed below the empty cages indicate how many squares, pentagons, and hexagons are utilized in order to construct that particular cages, e.g.* 5^{12} *means 12 pentagons are used.*

Bottom: *Four known clathrate structures (sI, sII, sH, and sT), forming by a combination of the above empty cages, are presented in a colour-coded manner. For example, sI is composed of two* 5^{12} *and six* $5^{12}6^2$ *cages per unit cell. Their space groups and the total number of the water molecules in a unit cell are listed underneath*

sII, the sT has only been found to form in the system that adopts only sII e.g. Ar and N_2 [28]. These four clathrate structures (sI, sII, sH, and sH) are shown in Figure 2.2. For clarity, the cages are displayed in different colours.

Chapter 3

Background Theory

3.1 Physics at High Pressure

Pressure surrounds us and we commonly experience it. However, we may not have yet realized its effects on the properties of materials. Like other thermodynamic variables, pressure is one of the terms controlling the stability of materials. When a material is compressed, its constituent atoms are brought closer. This causes an overlap of electronic orbitals. Thus, upon increasing pressure, the materials undergo the changes in their chemical bondings. This leads to the modifications of their crystal structures and electronic states, resulting in new stable phases that cannot be found at ambient pressure.

Both experimental and theoretical methods have been developed in order to explore the unusual behaviour of materials under high pressure. One of the most important tasks is to obtain the crystal structures of materials and construct their phase diagrams.

3.1.1 Experimental Methods

This subsection focuses on the experimental methods used in high-pressure laboratories. The pioneer work in this field was accredited to Bridgman, who developed the first high-pressure apparatus and set a foundation for a so-called "static compression" method. His successful invention enabled the high-pressre experiment to be performed at pressure up to 10 GPa. Nowadays, the static high-

pressure experiment can be performed at the pressure as high as 1 TPa, which is several times higher than the pressure at the centre of the Earth [30]. Another approach to study materials under high pressure is called "dynamic compression". In this method, the pressure is created by shock waves, which can be generated by chemical, electrical, or optical means.

Static Pressure

The history of the first experimental static pressure study is traced back to the 18th century [175]. It has developed hugely since then. Nowadays, high-pressure research can be performed at the pressure up to 1 TPa. The invention of static high-pressure apparatus will be presented in this topic in chronological order.

Under 2 GPa, the compressed fluid is the main source to create the pressure to the sample [170]. This pressure source can be intensified by using a cylinder of fluid with a piston for compression as pressure = force/area. Controlling the temperature by connecting to a heat bath helps the fluid-based techniques successfully measure the properties of materials under pressure. However, this compressed-fluid system requires no leakage of the fluid tube and the limit of the controlled temperature is governed by the mechanical strength of the chamber meterials.

Above 2 GPa, the increase in the fluid's viscosity prohibits the usage of the fluid pressure. Therefore, the sample is directly compressed by the solid surface, i.e. a piston is driven into a hollow cylinder with the sample inside [172]. The piston is often made by tungsten carbide because of its high compressive strength. Surrounded by a mechanically weak medium, the sample then almost experiences a hydrostatic condition. The piston-cylinder apparatus can detect the phase transitions of materials by measuring the electrical resistance or by differential thermal analysis (DTA), which measures the change in the latent heat. Nevertheless, the cylinder-piston apparatus is not suitable for optical or x-ray diffraction measurements. Additionally, the upper pressure limit of this apparatus is around 8 GPa due to the piston's fracture at higher pressure [175].

For experiments higher than 8 GPa, an anvil-based apparatus is commonly used. Two anvils make contact to a gasket, containing the sample, at a very small surface area. This creates a higher pressure to the sample than the originally applied pressure. Since the anvil is usually made of diamond, the name "diamond

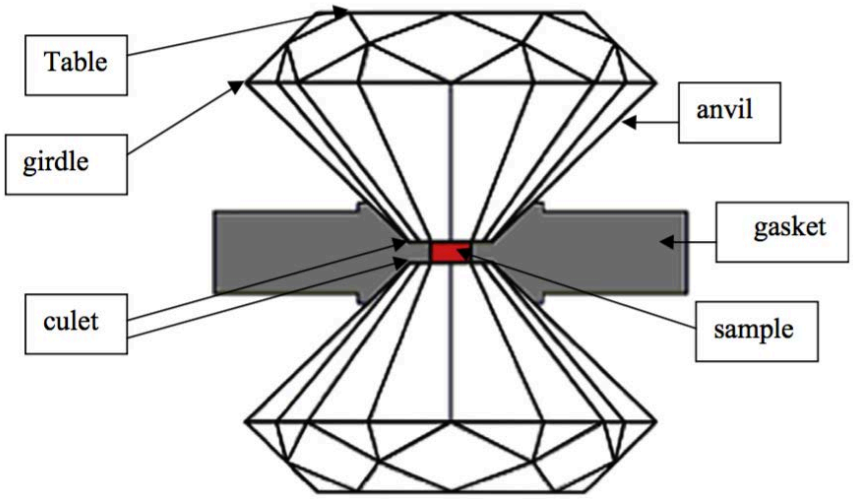

Figure 3.1 *A schematic picture of a diamond anvil cell (DAC). A tiny sample is compressed between the culets of two gem-quality diamonds [160].*

anvil cell (DAC)" is commonly known in the high pressure field. The DAC is shown schematically in Figure 3.1. The benefit of this diamond anvil cell is the accessibility of the optical and x-ray diffraction techniques. However, pressure calibration in anvil devices is very difficult. This is due to the nonhydrostatic nature, caused by non uniform stress across the sample under small contact area. The shift in the Ruby fluorescence line becomes the standard technique to measure the sample's pressure. However, above 100 GPa, the fluorescene line of diamond anvils is getting stronger and obscures the ruby line [157, 175].

There are various modifications of the DAC in order to maximize the attainable pressure. One of these is a double-stage DAC. In the double-stage DAC, a sample is place between two microscopic semishperes of superhard nanodiamond, which in turn are placed inside a conventional DAC. The double-stage DAC can produce a pressure as high as 1 TPa [31, 59].

3.2 Fundamental Theory

This section concentrates on the theorical background used in the calculations. Both quantum chemistry approaches and density functional theory are to be

discussed in details.

To investigate the materials under pressure, one possible way is to study computationally. Its main advantage over experiment is the ability to constrain the studied parameters so that the calculations can be easily done. The development of this field provides reliable results. There are several computational methods depending on the degree of accuracy. In this section, I will focus on a rather highly accurate approach in order to solve many-body interactions.

Supposing that no external force is acting to the system, the Hamiltonian is composed of only the kinetic and potential energy terms. Therefore, the Hamiltonian of the system (in atomic units) becomes

$$\hat{\mathcal{H}} = -\frac{1}{2M_m}\sum_m \nabla^2_{R_m} - \frac{1}{2}\sum_i \nabla^2_{r_i} - \sum_{im}\frac{Z_m}{|\vec{R}_m - \vec{r}_i|} + \frac{1}{2}\sum_{ij(i\neq j)}\frac{1}{|\vec{r}_i - \vec{r}_j|} + \frac{1}{2}\sum_{mn(m\neq n)}\frac{Z_m Z_n}{|\vec{R}_m - \vec{R}_n|}$$

$$= T_n + T_e + V_{en} + V_{ee} + V_{nn}$$

This Hamiltonian composes of five terms; the first and second term are the nulear and electronic kinetic energy. The last three terms represent the electron-nuclear, electron-electron, and nuclear-nuclear potential energy, respectively.

The time-independent Hamiltonian of the system can be written as

$$\hat{\mathcal{H}}\psi(\vec{R}_m, \vec{r}_i) = E\psi(\vec{R}_m, \vec{r}_i)$$

, where R is the nuclear position, r represents the electron position, m and i are the indices of the nuclei and electron, respectively.

The electronic relaxation is much faster than the nuclear motion because eletrons are much lighter than the nuclei. This huge difference in the relaxation timescale implies that the electron wavefunctions instantaneously adjust themself to the nuclear positions as if the nuclei are stationary. Therefore, the electonic and nuclear motion can be treated separately. The wavefunction of the system is assumed to be separable to the product of two wavefunctions (one depends only on electron co-ordinates and the other depends only on nuclear co-ordinates). This approximation is also known as the Born-Oppenheimer approximation.

$$\psi(\vec{R},\vec{r}) = \theta(\vec{R})\phi(\vec{r})$$

Thus, if taking the Born-Oppenheimer approximation into account, the previous Hamiltonian can be simplified to have only three terms. The first and the last term, which contains nuclear-nuclear interaction, can be neglected for the electronic wavefunction' calculations.

$$\hat{\mathcal{H}}_e = -\frac{1}{2}\sum_i \nabla^2_{r_i} - \sum_{im} \frac{Z_m}{|\vec{R}_m - \vec{r}_i|} + \frac{1}{2}\sum_{ij(i\neq j)} \frac{1}{|\vec{r}_i - \vec{r}_j|}$$

The Hamiltonian is the summation of the electronic part and the ionic part as

$$\hat{\mathcal{H}} = \hat{\mathcal{H}}_e + \hat{\mathcal{H}}_i$$

There are two main approaches to treat the complicated quantum mechanical equation. One is based on electronic wave function, so called "quantum chemistry approach", and the other is based on the electronic density, "density functional theory". Both methods require some assumptions in order to simplify the actual complicated many-body interactions.

3.2.1 Quantum Chemistry Approach

Hartree Method

Varieties of methods have been developed to handle the approximated solution for the simplified Hamiltonian. The oldest and simplest approach to treat the many-body equation is Hartree Method [55, 56].

By assuming that electrons are non-interacting particles, the wavefunction can be written as the product of the individual electron's orbital (the electron at each state) as

$$E^H = \min_{\{\phi_i\}} \langle\psi| H_e |\psi\rangle$$

$$\psi(\vec{r}) = \prod_{i=1}^{N} \phi_i(\vec{r}_i)$$

The Hartree equations for the single-particle orbitals can be written as:

$$H^H \phi_i(\vec{r}) = [T_e + V_{en} + V_i^H]\phi_i(\vec{r}) = \epsilon_i \phi_i(\vec{r})$$

$$V_i^H(\vec{r}) = V^H(\vec{r}) - \int \frac{|\phi_i(\vec{r})|^2}{|\vec{r} - \vec{r'}|} d^3\vec{r'}$$

$$V^H(\vec{r}) = \int \frac{n(\vec{r'})}{|\vec{r} - \vec{r'}|} d^3\vec{r'}, \quad n(\vec{r}) = \sum_{i=1}^{N} |\phi_i(\vec{r})|^2$$

, where $V^H(\vec{r})$ is the Hartree potential, which is the Couloumb interaction of the total electron density $n(\vec{r})$. The effective potential $V_i^H(\vec{r})$ acts on the orbital ϕ_i instead of the full electron-electron potential. This effective potential $V_i^H(\vec{r})$ corresponds to the interaction of the electron at orbital ϕ_i and the average mean-field contribution from all electrons,

However, it is not straightforward to solve the Hartree Hamiltonian H^H because it depends on its own solutions. In order to solve the Hartree Hamiltonian H^H, the effective potential $V_i^H(\vec{r})$, must be known. Nonetheless, the effective potential $V_i^H(\vec{r})$ depends on the orbital ϕ_i through an integral term, which is, in turn, corrected by an electron's interaction with itself.

A numerical method called "self-consistent field" is introduced in order to solve the Hartree equations. Its schematic diagram is shown in Figure 3.2. As illustrated in Figure 3.2, initial guess for the molecular orbitals ϕ_i is is used to solve the Hartree equation. The computed density $n(\vec{r})$ is then compared with the initial guess orbital's density. If they are not the same, the initial guess orbitals are updated with the calculated orbitals. This process continues until the final and the updated density agree, i.e. converge.

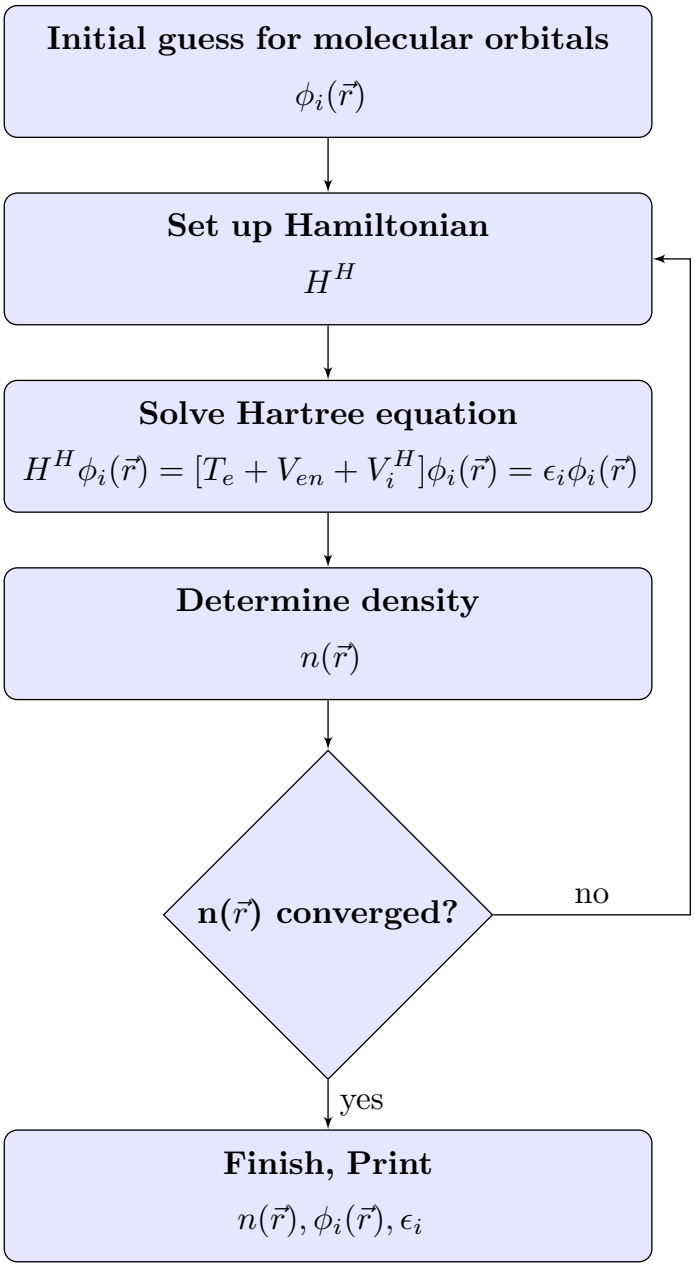

Figure 3.2 *A schematic diagram for the SCF method in order to solve the Hartree equation. Initial guess for the molecular orbitals corresponding to the initial atomic positions is set up. These orbitals are used in the Hartree equation. Self-consistent field (SCF) method is applied to obtain the correct orbitals by measuring the convergence of the electronic density $n(\vec{r})$. If the SCF converges, the program stops. This implies the final orbitals are suitable to represent the orbitals of the system within the limit of convergence parameters.*

Hartree-Fock Method

The main issue for the Hartree method is its assumption that electrons are distinguishable, hence ignores Pauli's exclusion principle. In fact, electrons are fermions so that they do not share the same quantum states. Therefore, the Fock wavefunction representing the electrons previously is needed to be modified to preserve the ansi-symmetric property of fermionic particles.

In order to solve this issue, Fock [43] and Slater [144] independently introduced a method to determine the wavefunction, which fulfills Pauli's exclusion principle, by constructing a co-called Slater determinant.

The wavefunction constructed by the Slater determinant is

$$\psi(r) = \frac{1}{\sqrt{N!}} \begin{vmatrix} \phi_1(r_1) & \phi_2(r_1) & ... & \phi_N(r_1) \\ \phi_1(r_2) & \phi_2(r_2) & ... & \phi_N(r_2) \\ . & . & ... & . \\ . & . & ... & . \\ . & . & ... & . \\ \phi_1(r_N) & \phi_2(r_N) & ... & \phi_N(r_N) \end{vmatrix}$$

, where N represents a total number of electrons and $\sqrt{N}$ is the normalising factor in order to preserve the orthonormality condition of the wavefunction.

Thus, the wavefunction determined by the Slater determinant can be written as

$$\psi(\vec{r}) = \frac{1}{\sqrt{N!}} \sum_{P} (-1)^P \prod_{i=1}^{P} \phi_i(\vec{r})$$

, where P is a permutation group of rank N which counts the numbers of permutations. P equals to 1 if having even permutations and is -1 for odd permutations.

Recalling that, the electronic Hamiltonian is

$$\hat{\mathcal{H}_e} = -\frac{1}{2} \sum_i \nabla_{r_i}^2 - \sum_{im} \frac{Z_m}{|R_m - r_i|} + \frac{1}{2} \sum_{ij(i \neq j)} \frac{1}{|r_i - r_j|}$$

$$\hat{\mathcal{H}}_e = T_e + V_{en} + V_e$$

This Hamiltonian can be re-written in terms of one-electron and two-electron representation as

$$\hat{\mathcal{H}}_e = \sum_i \hat{\mathcal{H}}_1(\vec{r}_i) + \frac{1}{2}\sum_{i \neq j} \hat{\mathcal{H}}_2(\vec{r}_i, \vec{r}_j)$$

, where the one-electron Hamiltonian $\hat{\mathcal{H}}_1$ represents the electonic kinetic energy T_e and the electron-nuclear potential energy operator V_{en}, the two-electron Hamiltonian $\hat{\mathcal{H}}_2$ is the electronic potential energy operator V_e.

For a given Hamiltonian, its expectation value can be obtained via

$$E_H = \langle\psi| \hat{\mathcal{H}}_e |\psi\rangle .$$

Hence, the expectation value for the Hamiltonian written in a form of one-electron and two-electron representation is

$$\langle\psi| \hat{\mathcal{H}}_e |\psi\rangle = \sum_i \langle\phi_i| \hat{\mathcal{H}}_1 |\phi_i\rangle + \frac{1}{2}\sum_{i \neq j} [\langle\phi_i\phi_j| \hat{\mathcal{H}}_2 |\phi_i\phi_j\rangle - \langle\phi_j\phi_i| \hat{\mathcal{H}}_2 |\phi_i\phi_j\rangle$$

The best possible estimation of the expectation value can be obtained by applying a variational principle with a set of Lagrange multipliers λ_{ij}.

$$\delta F = \delta[\langle\phi| \hat{\mathcal{H}}_e |\phi\rangle - \sum_{i,j} \lambda_{ij}(\langle\phi_i|\phi_j\rangle - \delta_{ij})] = 0$$

This leads to the Fock operator and the well-known Hartree-Fock equations for ϕ_i.

$$\hat{\mathcal{H}}^{HF} = \hat{\mathcal{F}} = \hat{\mathcal{H}}_1 + \sum_i (\hat{\mathcal{J}}_i - \hat{\mathcal{K}}_i)$$

$$\hat{\mathcal{F}} |\phi_i\rangle = [\hat{\mathcal{H}}_1 + \sum_i (\hat{\mathcal{J}}_i - \hat{\mathcal{K}}_i)] |\phi_i\rangle = \epsilon_i |\phi_i\rangle$$

, where

$$\hat{\mathcal{H}}_1 = T_e + V_{en}$$

$$\hat{\mathcal{J}}_j |\phi_i\rangle = \langle\phi_j| \upsilon |\phi_j\rangle |\phi_i\rangle$$

$$\hat{\mathcal{K}}_j |\phi_i\rangle = \langle\phi_j| \upsilon |\phi_i\rangle |\phi_j\rangle$$

The Fock operator $\hat{\mathcal{F}}$ contains the one-electron operator and a summation of the difference in the Coulomb operator $\hat{\mathcal{J}}$ and the exchange operator $\hat{\mathcal{K}}$. The Coulomb operator $\hat{\mathcal{J}}$ represents the classical Coulombic electron-electron repulsion energy and the operator $\hat{\mathcal{K}}$ corresponds to the exchange energy due to the antisymmetry of the total n-electron wavefunction.

Many-body Perturbation Theory

In Hartree-Fock method, although the exchange interaction is properly well defined, the electronic correlation interactions are left unconsidered. This is due to its assumptions of treating the electrons as non-interacting particles and concerning only the ground state properties of the wavefunctions. One way to cope with this issue is to perturb the system to excited states such that the wavefunctions cover in both the occupied and excited states, resulting in the recovery of the electron-electron correlation interactions. The equation of the many-body perturbation [113] is written in a form of the exact Hartree-Fock Hamiltonian plus the perturbed term as

$$\hat{\mathcal{H}} = \hat{\mathcal{H}}^{HF} + \lambda V$$

$$V = V_{ee} - \sum_{i=1}^{N} (\hat{\mathcal{J}}_i - \hat{\mathcal{K}}_i)$$

This many-body perturbation theory is also known as Moller-Plesset (MP) theory. The degree of perturbations is denoted by the power of the coupling constant λ.

$$|\psi\rangle = |\psi_{HF}\rangle + \lambda |\psi_1\rangle + \lambda^2 |\psi_2\rangle + ...$$

The corresponding total enery can be written as

$$E = E_0 + \lambda E_1 + \lambda^2 E_2 + ...$$

In MP2, the number "2" denotes the perturbation is performed up to the second-order term and truncated the effects of higher order terms.

$$E_0 = \langle \psi_{HF} | \, \hat{\mathcal{H}}^{HF} \, | \psi_{HF} \rangle = \sum_{i=1}^{N} \epsilon_i$$

$$E_1 = \langle \psi_{HF} | \, V \, | \psi_{HF} \rangle = -\frac{1}{2} \sum_{i,j=1}^{N} (\langle \phi_i | \, \hat{\mathcal{J}}_j \, | \phi_i \rangle - \langle \phi_i | \, \hat{\mathcal{K}}_j \, | \phi_i \rangle$$

$$E_2 = \langle \psi_{HF} | \, V \, | \widetilde{\psi}^1 \rangle = \frac{1}{4} \sum_{i,j=1}^{occ} \sum_{r,s}^{unocc} \frac{|\langle \psi_{HF} | \, V \, | \psi_{i,j}^{rs} \rangle|^2}{E_0 - E_{ij}^{rs}}$$

, a doubly excited state $|\psi_{i,j}^{rs}\rangle = a_s^\dagger a_r^\dagger a_j a_i \, |\psi_{HF}\rangle$ is created via a creation $a_i^\dagger$ and an annihilation a_i operator that increases or decreases the electronic occupation number of the orbital $|\phi_i\rangle$ by 1, respectively.

In summary, the electronic correlation effect can be obtained in the many-body perturbation theory by perturbing the electronic wavefunction into the unoccupied states and hence considering the electronic wavefunction in both occupied and unoccupied states. Better descriptions of the correlation interaction require higher-order perturbations. However, the many-body perturbation theory poorly scales with the number of the perturbations. Consequently, other computationally more efficient methods to treat the correlation effect are needed.

Coupled Cluster Theory

Originally developed in the field of nuclear physics [24], the coupled cluster (CC) theory becomes very popular in atomic and molecular calculations [24, 141]. Like the many-body perturbation method, the CC theory implements the idea of expanding the HF wavefunction into excited states.

According to the CC ansatz, the CC wavefunction can be expanded by a certain number of excitations (single, double, ...) as

$$|\psi_{CC}\rangle = \left[\prod_{a,r}(1 + t_a^r a_r^\dagger a_a)\right]\left[\prod_{ab,rs}(1 + t_{ab}^{rs} a_s^\dagger a_r^\dagger a_b a_a)\right]... |\psi_{HF}\rangle \,,$$

, where the index a denotes the occupied electronic states (running from 1 up to N, where N is the total number of electrons) and the index r represents the unoccupied states (running from N+1 up to ∞).

By using the properties

$$(1 + t_a^r a_r^\dagger a_a) = \sum_{k=0}^{\infty} \frac{1}{k!}(t_a^r a_r^\dagger a_a)^k = e^{t_a^r a_r^\dagger a_a}$$

, the full CC wave function in an exponential ansatz can be written as

$$|\psi_{CC}\rangle = e^T |\psi_{HF}\rangle \,,$$

$$T = T_1 + T_2 + ... + T_N$$

, where T_i denotes the sum over all possible excitations of i electrons:

$$T_1 = \sum_{a,r} t_a^r a_r^\dagger a_a$$

$$T_2 = \sum_{ab,rs} t_{ab}^{rs} a_s^\dagger a_r^\dagger a_b a_a$$

...

While, in theory, a full CC expansion can contain up to N-tuple excitations, the highest number of the electronic excitations is usually performed at triple excitations in practice. The nomenclature for considering the CC method up to triple excitations, i.e. $T = T_1 + T_2 + T_3$, is "CCSDT".

Note that, CCSD(T) is very accurate and is also known as a "gold standard" approach for quantum chemists. The term "T" in the round bracket indicates that this term is calculated based on the many-body perturbation theory instead. The reason is that it is computationally infeasible to have a full treatment of the

triple excitations for large molecules.

3.2.2 Density Functional Theory

The fundametal ideas of density functional theory are based on two seminal papers by Hohenberg, Kohn, and Sham [71, 91]. The main concept is to deal with the total electronic density $n(\vec{r})$ instead of dealing with electronic wavefunctions in the many-body Schrodinger equation. This causes a huge simplification because the number of the degrees of freedom is significantly reduced i.e. from 3N, where N is the number of electrons in the system, in the wavefunction-based methods to only 3, which represents the spatial coordinates of the electron density (or 4N to 4 if including spin).

Hohenberg-Kohn Theorems

Let's start with two theorems proved by Hohenberg and Kohn [71]. These two theorems put a firm theoretical foundation relating the electron density and the ground state properties of materials.

Theorem I: The ground state density $n_0(\vec{r})$ of a many-electron system is uniquely determined by an external potential $V_{ext}(\vec{r})$.

Proof: The first theorem can be proved by contradiction.

Let's assume that there are two different external potentials $V_{ext}(\vec{r})$ and $V'_{ext}(\vec{r})$ that have the same ground state density $n_0(\vec{r})$. These two potentials correspond to two Hamiltonians $\hat{\mathcal{H}}$ and $\hat{\mathcal{H}}'$ that act on different ground state wavefunctions $|\psi_0\rangle$ and $|\psi'_0\rangle$.

$$\hat{\mathcal{H}} |\psi_0\rangle = E_0 |\psi_0\rangle$$
$$\hat{\mathcal{H}}' |\psi_0\rangle = E'_0 |\psi'_0\rangle$$

Thus, from the variational principle

$$E_0 = \langle\psi_0| \hat{\mathcal{H}} |\psi_0\rangle < \langle\psi'_0| \hat{\mathcal{H}} |\psi'_0\rangle$$
$$E_0 < \langle\psi'_0| \hat{\mathcal{H}}' |\psi'_0\rangle + \langle\psi'_0| \hat{\mathcal{H}} - \hat{\mathcal{H}}' |\psi'_0\rangle$$

$$E_0 < E_0' + \int d^3\vec{r} n(\vec{r})[V_{ext}(\vec{r}) - V'_{ext}(\vec{r})] \tag{3.1}$$

Similarly,

$$\begin{aligned} E_0' &= \langle \psi_0' | \, \hat{\mathcal{H}}' \, | \psi_0' \rangle < \langle \psi_0 | \, \hat{\mathcal{H}}' \, | \psi_0 \rangle \\ E_0' &< \langle \psi_0 | \, \hat{\mathcal{H}} \, | \psi_0 \rangle + \langle \psi_0 | \, \hat{\mathcal{H}}' - \hat{\mathcal{H}} \, | \psi_0 \rangle \\ E_0' &< E_0 - \int d^3\vec{r} n(\vec{r})[V_{ext}(\vec{r}) - V'_{ext}(\vec{r})] \end{aligned} \tag{3.2}$$

Adding (3.1) and (3.2) results in a contradiction,

$$E_0 + E_0' < E_0 + E_0'$$

Therefore, the initial assumption is wrong. This proves that the external potential explicitly maps the ground state density by a 1-1 function.

Theorem II: The exact ground state energy $E_0(n)$ is uniquely determined by the true ground state density $n_0(\vec{r})$, i.e. $E_0(n)$ is minimum at $n(\vec{r}) = n_0(\vec{r})$.

Proof: The proof of the second theorem is also by contradiction.

Let $n \in \mathbb{N}$ with $n \neq n_0$ and $E_0[n] < E_0[n_0]$. This is impossible because

$$E_0[n] = \langle \psi_0[n] | \, H[n_0] \, | \psi_0[n] \rangle > \langle \psi_0[n_0] | \, H[n_0] \, | \psi_0[n_0] \rangle = E_0[n_0], \quad n \neq n_0$$

The two theorems by Hohenberg and Kohn devise a conceptual framework on the electron density. For a given external potential $V(\vec{r})$, the ground state energy can be obtained by a minimisation process as

$$E_0[n_0] = \min_{n \in \mathbb{N}} E_0[n]$$

3.2.3 Kohn-Sham DFT

Although the Hohenberg and Kohn theorems assure us on the role of the electronic density $n(\vec{r})$ in electronic structure calculations, these two theorems do not

provide any guildeline on how to exploit them in actual calculations. The implementation of density in actual calculations was presented by Kohn and Sham.

In Kohn-Sham DFT, the interacting electrons are simplified to non-interacting quasi-particles in an effective single-particle potential. This potential depends only on single-particle orbitals. In HF, the solution is obtained by optimising the single particle orbitals to minimise the total energy. Similar idea can be applied to DFT calculation.

In DFT, we know that the energy is a functional of the ground state density. If one can construct the effective potential, the many-body non-interacting system can be solved [91].

Let H and H_s be the Hamiltonians of the interacting and non-interacting systems, respectively:

$$H = T_e + V_{ee} + V \tag{3.3}$$

$$H_s = T_s + V_s \tag{3.4}$$

, V_{ee} is vanished in the non-interacting system.

The ground state density should be identical: $n_0(\vec{r}) = n_s(\vec{r}) = n(\vec{r})$.

The ground state energy can be found by minimising $\langle\psi| H |\psi\rangle$ over all normalised wavefunctions.

$$E = \min_{\psi} \langle\psi| H |\psi\rangle$$

Thus, by minimising (3.3), we can get the ground state energy of the interacting system:

$$E = \min_{\psi\to n} \langle\psi| H |\psi\rangle = \min_{\psi\to n} \langle\psi| T_e + V_{ee} |\psi\rangle + \int d^3\vec{r} V(\vec{r}) n(\vec{r})$$

A universal function F is defined as

$$F[n] = \min_{\psi \to n} \langle \psi | \, T + V_{ee} \, | \psi \rangle = \langle \psi_n^{min} | \, T + V_{ee} \, | \psi_n^{min} \rangle$$

, where ψ_n^{min} is the wavefunction that delivers the minimum for a given n.

Thus,

$$E = \min_n \left\{ F[n] + \int d^3\vec{r} \, V(\vec{r}) n(\vec{r}) \right\}$$

Apply a variational principle with a Lagrange multiplier μ,

$$\delta \left\{ F[n] + \int d^3\vec{r} \, V(\vec{r}) n(\vec{r}) - \mu \int d^3\vec{r} n(\vec{r}) \right\} = 0$$

, which is equivalent to the Euler equation

$$\frac{\delta F}{\delta n(\vec{r})} + V(\vec{r}) = \mu \tag{3.7}$$

Hence μ is to adjusted until the integral of the electron density equals to N

$$\int d^3(\vec{r}) \; n(\vec{r}) = N$$

Similarly, for the non-interacting system, (3.4) can be written as

$$E_s = \min_n \left\{ F_s[n] + \int d^3\vec{r} \, V_s(\vec{r}) n(\vec{r}) \right\}$$

$$F_s[n] = \min_{\psi \to n} \langle \psi | \, T_s \, | \psi \rangle = \langle \psi_n^{min} | \, T_s \, | \psi_n^{min} \rangle$$

$$\frac{\delta F_s}{\delta n(\vec{r})} + V_s(\vec{r}) = \mu_s \tag{3.6}$$

In Kohn-Sham non-interacting system, the potential V_s is a functional of $n(\vec{r})$. Hence, the difference in the chemical potentials for the interacting μ and non-interacting system μ_s will tell us about the deviation of the simplified non-

interacting system V_s from real system.

The difference between F and F_s is defined by

$$F[n] = F_s[n] + V_H[n] + E_{xc}[n]$$

, where the $E_{xc}[n]$ is the exchange-correlation energy, $V_H[n]$ is the Hartree electrostatic self-repulsion of the electron density

$$V_H[n] = \frac{1}{2}\int d^3\vec{r'}\frac{n_0(\vec{r'})}{|r - r'|}$$

Hence, (3.5) and (3.6) are identical if they have same chemical potentials, leading to

$$V_s(\vec{r}) = V(\vec{r}) + \frac{\delta V_H[n]}{\delta n(\vec{r})} + \frac{\delta E_{xc}[n]}{\delta n(\vec{r})}$$

This determines the effective potential V_s, while leaving the exchange correlation E_{xc} to be approximated.

In summary, the Kohn-Sham equations are

$$\left\{ -\frac{1}{2}\nabla^2 + V_s(\vec{r})\right\}\phi_i(\vec{r}) = \epsilon_i\phi_i(\vec{r})$$

$$n(\vec{r}) = \sum_{i=1}^{N}|\phi_i(\vec{r})|^2$$

The Kohn-Sham equation can be nummerically solved by using self-consistent loops as illustrated in Figure 3.2. Initial guess of the electron density of the system is applied to the calculation of the effective potential V_s. The calculated effective potential is used to set up the Kohn-Sham equation, which can be nummerically solved. Self-consistent loops are applied until the electron density converges.

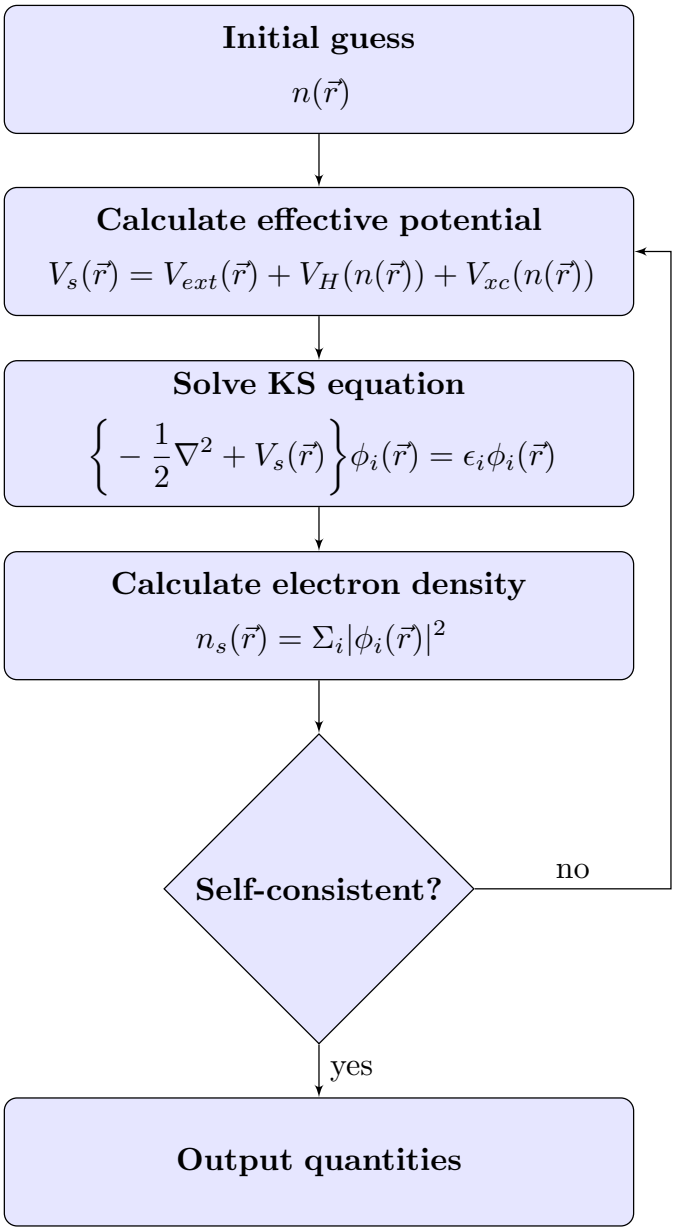

Figure 3.3 *A flowchart of the Kohn-Sham DFT. The electron density is initially guessed and is used in the effective potential (V_s) calculation. Self-consistent method is applied in order to solve the Kohn-Sham equation by checking the convervence in the electron density. Once it reaches the required accuracy, the loop is over and the output quantities are calculated.*

3.2.4 Exchange-Correlation Functional

In Kohn-Sham equation, the only unknown parameter is the exchange-correlation energy E_{xc}. E_{xc} contains all the interactions that are left unconsidered in the simplified Kohn-Sham equation. In other words, it contains the self-interaction correction to the Hartree term and the kinetic energy difference between the interacting and non-interacting system. Two widely methods, namely local density approximation and generalized gradient, in order to approximate the exchange-correlation energy are discussed in this subsection.

Local Density Approximation

Local density approximation (LDA) develops its idea from the homogeneous electron gas (HEG), which provides good approximation for the valence electron in metals.

In LDA, exchange-correlation energy E_{xc} is written as the integral over the local contributions from the HEG's exchange-correlation energy denstity $\epsilon_{xc}^{hom}(n)$.

$$E_{xc}^{LDA}[n] = \int d^3\vec{r} n(\vec{r}) \epsilon_{xc}^{hom}|_{n(r)}$$

The exchange-correlation potential $V_{xc}[n]$ used in the effective potential calculation is

$$V_{xc}^{LDA}[n] = \epsilon_{xc}^{hom}(n)|_{n(r)} + n(\vec{r}) \frac{\partial}{\partial n} \epsilon_{xc}^{hom}(n)|_{n(r)}$$

In general, the exchange-correlation energy as E_{xc} can be decomposed into exchange and correlation term:

$$E_{xc} = E_x + E_c$$

The exchange part often takes on the analytic form for the HEG [171]

$$E_x^{LDA}[n] = -\frac{3}{4}\left(\frac{3}{\pi}\right)^{1/3} \int n(\vec{r})^{4/3} d(\vec{r})$$

While the exchange part has only one form that is popular, there are many forms

of the correlation part. Highly accurate correlation functionals are retreived either by empirically fitted to Monte Carlo data or fitted to the theoretical constraint when the functional approaches high density limit [21, 22, 123] .

Generalized Gradient Approxmation

In LDA, it is likely to underestimate the exchange energy and overestimate the correlation energy because the density is assumed to be the same everywhere. However, the errors tend to compensate each other so that it successfully calculates ground state energies, lattice constants of various materials, especially metals.

To correct the under- and over-estimated tendency of LDA, the exchange-correlation energy is expanded in terms of the gradient of a density to account for the inhomogeneity to the electron density.

$$E_{xc}[n] = \int d^3\vec{r})\ n(\vec{r})\epsilon_{xc}(n, \nabla n)|_{n(r)}$$

Various versions of the GGAs have been proposed to varieties of materials. Among these, PW91 [169] and PBE [122] are the most widely-used. Both depend on the local electron density n and the spin polarization ζ

$$E_x[n] = \frac{1}{2}\widetilde{E}_x[(1+\zeta)n] + \frac{1}{2}\widetilde{E}_x[(1-\zeta)n],$$

$$\widetilde{E}_x[\widetilde{n}] = \int d^3\vec{r}\ \widetilde{n}(\vec{r})F(s)\epsilon_x^{hom}(n)|_{\widetilde{n}(\vec{r})}$$

$$E_c[n] = \int d^3\vec{r}\ n(\vec{r})[\epsilon_c^{hom}(n,\zeta) + H(t, r_s, \zeta)]$$

The density gradient can be tuned by parameter s and t (PW91 and PBE have different scaling factors). These two parameter affect the function F and H, respectively. In LDA, $F(s) = 1$ and $H(t, r_s, \zeta) = 0$.

Table 1.1 shows the typical relative errors from the calculations using LDA and GGA approximations. In most cases, GGA approximation provide better results than LDA. Note that, there are some cancellations of errors between the exchange (E_x) and correlation (E_c).

Property	LDA	GGA
E_x	5% (not negative enough)	0.5% (not negative enough)
E_c	100% (too negative)	5% (too negative)
bond length	1% (too short)	1% (too long)
structure	favours close packing	more correct
energy barrier	100% (too low)	30% (too low)

Table 3.1: Typical errors from self-consistent Kohn-Sham calculations with LDA and GGA approximations. [20].

3.2.5 Dispersion corrections for DFT

Electron dispersion interactions are ubiquitous in nature that play an important role determining the structure of biomolecules such as DNA, molecular crystals, and molecules on surfaces [85]. However, an accurate description is still challenging for density functional theory (DFT). It has been proven that vdW-corrected functional is crucial in some systems such as rare gases and biomelecules; while most standard exchange-correlation functionals fail to accurately describe those systems [85]. Therefore, this section is devoted to emphasise the significance of van der Waals corrected functionals currently used in DFT and also in this thesis.

Standard exchange-correlation functionals

In the past few decades, Kohn-Sham density functional theory has been used in physics, chemistry, and material science. The heart of this theory is how accurate in the approximation of the exchange-correlation (XC) functionals. Nonetheless, there is a lack of dispersion forces in standard XC functionals, which mostly refer to local density approximation (LDA), generalized gradient approximation (GGA), and hybrid XC functionals [85]. These vdW forces are crucial in weakly interacting systems; for example, water, rare gas dimers [49, 85, 136]. The quest for finding proper XC functionals to accurately treat dispersion interactions is still one of the hottest topics in the field [76, 85].

Dispersion interaction originates from the response of electrons to an instantaneous fluctuation of charge density. This is also known as dipole-induced dipole

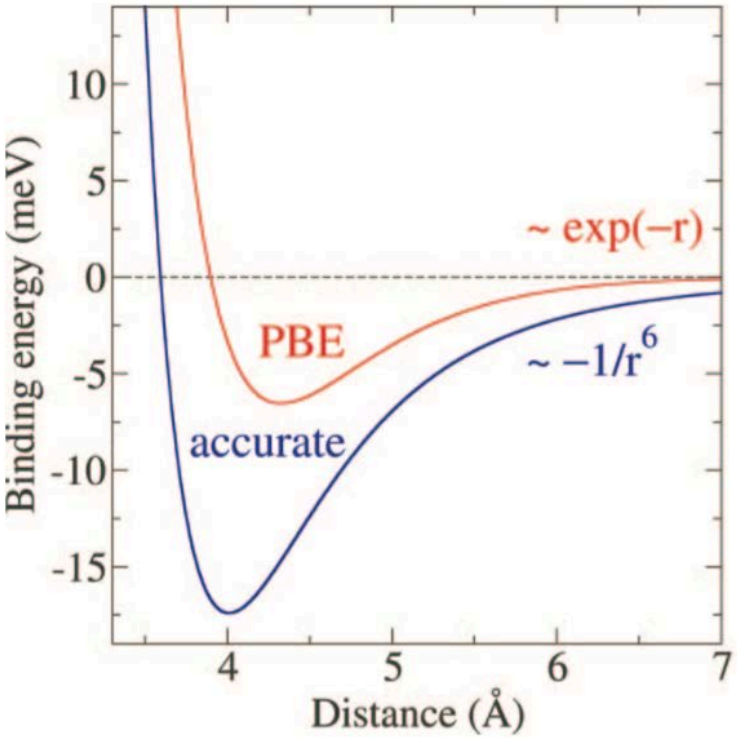

Figure 3.4 *Kr-Kr dimer's binding energy curves with PBE XC functional compared to an accurate -1/r^6 decay. Dispersion interactions from the fluctuations of electron density, which polarize different atoms, is well-known to have -1/r^6 decay. PBE (and most other semi-local functionals) fails to accurately describe this decay but instead represent exponential decay. This exponential decay arrives from the overlap of density. [85]*

interactions, which gives -1/r^6 decay of the interaction energy with interatomic seperation r.

The study of Kr-Kr binding energies from PBE exchange-correlation functional compared to an accurate binding energy curve with -1/r^6 decay is shown in Figure 3.4 [85]. It is obvious that PBE (and other semi-local functionals) fails to accurately describe this decay but represents an exponential decay instead.

The -1/r^6 decay is commonly found in the dispersion interactions from the fluctuations of electron density. However, standard exchange correlation functionals (LDA and GGA) represent exponentially decay, which is originated from the overlap of densities. This inaccurate description of PBE causes errors in determining properties of materials.

Thus, appropriate methods that include the vdW interactions are necessary

in order to produce the actual binding energy. Several approaches have been proposed to fix the issue, which can be mainly classified into two catagories: (i) semi-empirical based method (vdW-D) family, e.g. vdW-D2 and (ii) non-local van der Waals density functional (vdW-DF). The first type uses tabulated experimental data for the dispersion coefficients to obtain the dispersion-corrected energies; whereas, the latter combines the dispersion correlation effects into the exchange-correlation functional. Both methods will be described in more details in the following section.

Semi-empirical vdW-D

In order to treat the dispersion effect accurately, the crucial requirement is to obtain a reasonable interaction representing -1/r^6 behavior for the interactions. A simple approach to achieve this is to add an additional energy term, which accounts for the missing long range attraction. The total energy can then be written as:

$$E_{tot} = E_{DFT} + E_{disp},$$

where E_{DFT} is the DFT energy computed using a given exchange-correlation functional.The dispersion energy E_{disp} can be written as

$$E_{disp} = -\sum C_6^{AB}/r_{AB}^6,$$

where the dispersion coefficients C_6^{AB} depend on the elemental pairs A and B. The dispersion within this approximation is assumed to be pairwise additive and can be calculated as a sum over all pairs of atom A and B. Such C_6^{AB} coefficients are constants and are tabulated. This method is often referred to as "vdW-D" or "DFT-D" method.

Despite of its simplicity and low compitational cost in the computation of the pairwise C_6/r^6 correction, it neglects both many-body dispersion effects and faster decaying terms such as the C_8/r^8 and C_{10}/r^{10} interactions. Thus, various formula involving experimental input i.e. ionization potentials and polarizabilities have been proposed [49].

Figure 3.5 illustrates a binding energy curve (E_{tot}) obtained by adding a dispersion

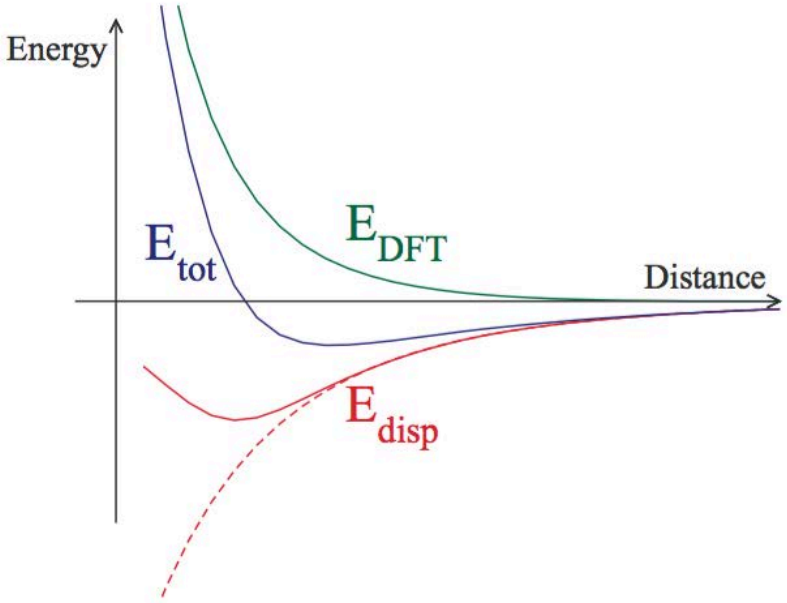

Figure 3.5 *Binding energy curve (E_{tot}) obtained from a dispersion corrected DFT calculation and its contribution to the regular DFT energy (E_{DFT}) and the dispersion correction (E_{disp}). Dashed curve represents -1/r^6 term describing the dispersion interaction in long range and must be fitted with other 1/r^n terms to accurately model the position of the energy minima (solid curve). [85]*

interaction energy (E_{disp}) to the DFT energy (E_{DFT}) [85]. The dispersion correction interaction (E_{disp}) is usually represented by the -1/r^6 term. Red dashed line represents a -1/r^6 function which diverges for small r so that it must be damped (red solid line). The amount of damping governs the energy minima on the binding curve. Thus, this damping function is needed to be fit to reference data.

In 2006, two research groups independently proposed the semiempirical van der Waals correction to the density functional [40, 50]. Ortmann et al provided a correction based on the asymptotic London form of dispersive forces for each pair of atoms [40]. Nevertheless, this method is not popular due to its limited accessibility. Grimme [50] proposed a method named "DFT-D2", in which the dispersion coefficients are calculated from a formula, which couples ionization potentials and static polarizabilities of isolated atoms. However, the DFT-D2 has some shortcomings, particularly, the dispersion coefficeints for some elements

(such as alkali and alkali earth atoms) are made by taking an average of noble gas and group III atom. Secondly, the dispersion energy E_{disp} is scaled with the the XC functional used so that the interaction energy is not constant but is related to the choice of XC functional.

Additionally, a major problem with the "DFT-D2" method is that the dispersion coefficient is predetermined and is constant. For each element, the same value of the dispersion coefficient is applied no matter what state of that element is, i.e. its oxidation or hybridization. Thus, two main approaches have been introduced to overcome this drawback, namely DFT-D3 proposed by Grimme et al [132] and vdW-TS proposed by Tkatchenko and Scheffler [156].

In DFT-D3 method, the C_6 coefficient is adjusted according to the number of neighbours. The higher number of the neighbours is, the lower the value of C_6 coefficient. This is due to the fact that the atom feels more squeezing effects caused by its neighbours. Therefore, in DFT-D3 approach, the C_6 coefficients are precalculated for various pairs of elements in different hybridization states and the appropriate C_6 coefficient is assigned to each atomic pair according to the current number of its neighbours. Additionally, the function counting the number of neighbours continuously interpolates between the precalculated reference values so that if the hybridization state of an atom changes during the calculation, its C_6 coefficient will change accordingly [85].

In 2009, Tkatchenko and Scheffler [156] proposed a method based on reference atomic polarizabilities and reference C_6 coefficients to calculate the dispersion energy. During the calculation, the electron density of a molecule is divided between the individual atoms and this density is compared to the density of a free atom. The C_6 coefficient of a reference atom is then scaled according to this comparison. New value of C_6 coefficient is obtained and then used to calculated the dispersion energy of the system [163].

Non-local vdW-DF

As mentioned in the previous subsection, both standard LDA and GGA fail to describe the $-1/r^6$ decay in Kr dimer. This suggests proper methods that can account for vdW interactions in DFT are necessary. The van der Waals density functional (vdW-DF) are proposed to emphasize the accurate treatment of such dispersion interactions lacked in standard LDA and GGA functionals.

Several vdW approximations are proposed. Some are based on calculating atom-based pair potentials [128, 174], some also include advanced screening mechanisms [34, 155, 163]. However, a first-principles DFT treatment used in the calculations in this thesis is based on a nonlocal exchange-correlation functional, or typically known as the Rutger-Chalmers vdW-DF method. These are named after Rutger and Chalmers Universities, where main developers of vdW-DF functionals work in these affiliations.

There are other non-local density functionals such as the ones proposed by Vydrov and Van Voorhis [167, 168]; however, the non-local van der Waals density (vdW-DF) used in this thesis is based on Langreth, Lundqvist and co-workers [27, 84, 100, 130, 151].

In vdW-DF, the exchange-correlation is written as

$$E_{xc} = E_x^{GGA} + E_c^{LDA} + E_c^{nl},$$

where $E_x{}^{GGA}$ is the the revPBE exchange energy [177], E_c^{LDA} is the LDA correlation energy, and E_c^{nl} represents the non-local correlation energy term.

$$E_c^{nl} = \frac{1}{2} \int d^3r d^3r' n(\vec{r}) \phi(\vec{r}, \vec{r'}) n(\vec{r'}),$$

where $\phi(\vec{r}, \vec{r'})$ is an integration kernel, which is analogous to the classical Coulomb interaction kernel, i.e. depending on $\vec{r'}$-$\vec{r}$, and n is the density of electrons.

Various forms for E_c^{nl} were proposed in the 1990s with the restriction to non-overlapping fragments [128, 174]. In 2004, Dion et al solved this limitation by proposing a functional form which can evaluate the overlapping molecules [27]

The method proposed by Dion has been termed the van der Waals density functional (vdW-DF). The vdW-DF makes a significant impact in the dispersion interaction correction in DFT because it adds dispersion interactions directly to a DFT functional and combines correlations of all ranges in a single formula [85]

Varieties of forms of the original vdW-DF has been developed since it was shown by Vydrov and van Voorhis that the original vdW-DF tends to overestimate the long range dispersion interaction [167]. Hence, they proposed a computationally cheaper functional but having better average errors by 50% [167, 168]. The

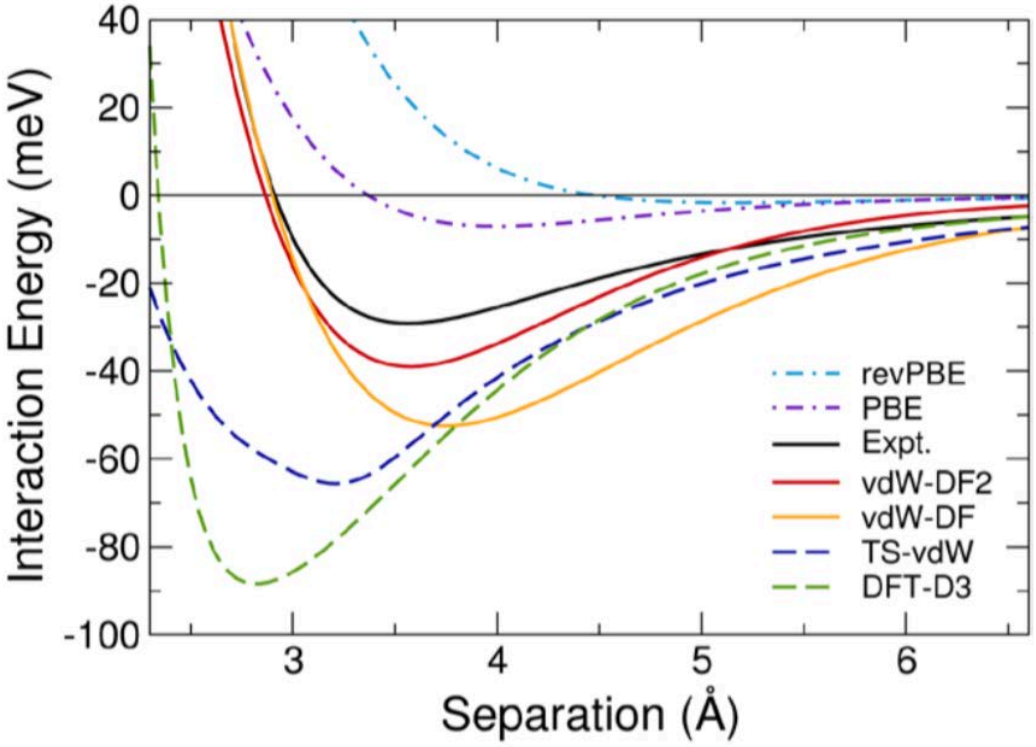

Figure 3.6 *Comparison between experimentally determined and calculated interaction energy for H_2 on Cu(111) using different methods [76].*

developers of the original vdW-DF realised this issue and announced a second version, vdW-DF2, which solves the overbinding effect at large separations [100] by modifying both the exchange and non-local correlation components. However, the predicted C_6 coefficients are still considerably underestimated [168].

Figure 3.6 demonstrates a comparison between experimentally determined and computationally predicted adsorption energy curve for H_2 on Cu(111) [76]. According to Figure 3.6, all the vdW-corrected functionals (both semi-empirical and non-local methods) tend to overbind the interaction energy; whereas both semi-local PBE and revPBE underestimate the interaction energy of the system. Among these, the vdW-DF2 (red solid line) deviates least from the experiment (black solid line). Thus, it is clear that a proper vdW-corrected functional is necessary in order to accurately predict the interaction energy.

Aside from the development of the E_c^{nl}, the original proposed revPBE exchange functional in the $E_x{}^{GGA}$ part often leads to too large intermolecular binding distances causing inaccurate binding energies. Thus, several exchange functionals with less repulsive interactions have been proposed; these include the "optB88" and "optPBE" exchange functionals [151].

3.3 Nudged Elastic Band Theory

A common dynamical study in condensed matter physics and theoretical chemistry is to identify the chemical pathway. This method is to find a minimum energy path through the process of transitional states. This transition state theory is used to figure out the energy barrier that the system is needed to overcome for a particular reaction or chemical pathway. In order to determine the minimum energy pathway, a chain of states is connected by a spring so that the force along the chain is governed by the spring force to ensure an equal spacing [57, 139]. The potential force is only allowed to act perpendicularly to the chain. The states along the pathway is represented by images. Finally, the total force on the system can be written as

$$F^{NEB} = F_i^v + F_i^p,$$

in which the F_i^v is the vertical component of the force (i.e. the force that is perpendicular to the unit tangent) and F_i^p represents a spring force parallel to the band.

$$F_i^v = -P_t g(y_i), P_t = E - t_i t_i^T$$

$$F_i^p = k(|y_{i+1} - y_i| - |y_i = y_{i-1}|)t_i$$

$$t_i = \frac{g(y_i)}{|g(y_i)|}$$

, g is the gradient of the PES, P_t is a projection operator constructed by a dyadic product of the tangent vector, E is the unit matrix, t is the steepest descent of the curve and k is the spring constant. In this case, the spring interaction between adjacent images is considered to ensure the continuity of the chain [127].

In order to compute the action of potential force, the spring constant (k) is initailly set to zero. Then, find a chain that fulfills the projector equation under no spring forces:

$$P_t g(y_i) = 0$$

Since every steepest descent curve is a solution of the above equation, the initial process can be easily done. The NEB method is normally considered with week spring forces, it can localize images on a gradient extremal along the valley of the PES. The gredient extremal is a quasi-solution to the equation shown above yielding the smallest eigenvalue.

The second part is obtained when having the spring force, which is to ensure quasi equal spacing of the images (along the tangent of the curve).

Several numerical methods are implemented for efficiently find the general gredient pathway such as utilising Newton-Raphson steps [126].

In summary, nudged elastic band theory (NEB) is introduced in order to perform a geometry optimization of atoms along to potential energy surface (PES). Such process is obtained by considering spring forces along a chain of images in order to search for the global energy pathway. Figure 3.7 illustrates the initial and final configuration of a NEB calculation with 16 images. Note that, NEB is one of the useful methods to optimise the energy pathway.

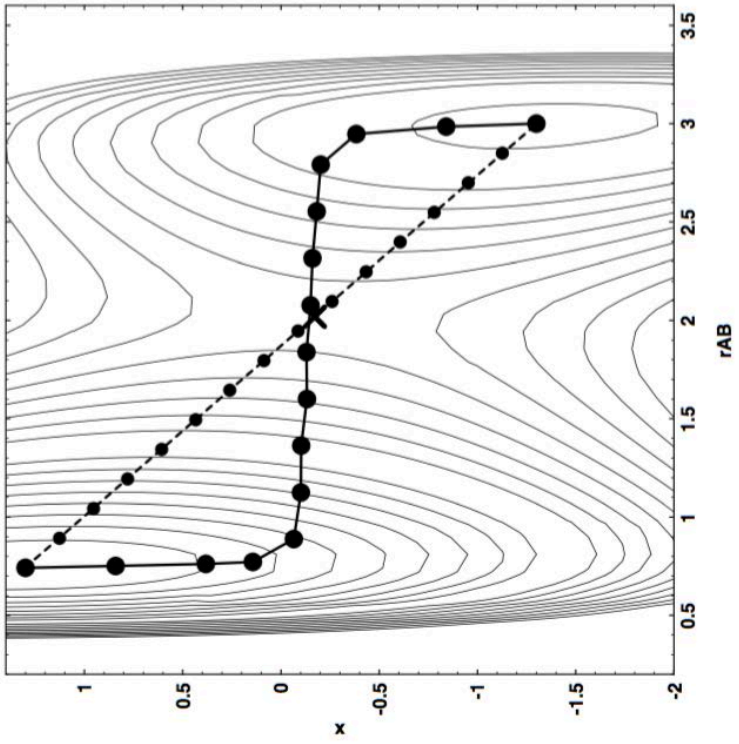

Figure 3.7 *Initial and final configuration of a NEB calculation with 16 images. Dashed and filled line represent initial and final configuration, respectively. [74]*

Chapter 4

Computational Methods

4.1 DFT in periodic systems

In the previous chapter, density functional theory is introduced for solving the complicated many-body systems. In order to solve the Kohn-Sham equations numerically, several computational techniques have been introduced. Therefore, fundamental knowledge about electronic structure calculations will be discussed in this section.

4.1.1 Basis Sets

Any arbitrary wavefunction ψ can be expressed as a sum of the basis function ϕ_i,

$$\psi = \sum_i c_i \phi_i.$$

The basis set is said to be "complete" if the representation of ψ is accurate. However, this requires an infinite number of the basis function ϕ_i. Hence, in practice, a finite number of the basis function is used instead. Any function that maintains the limiting behaviour of the real wavefunction could be used as a basis function, i.e. the basis function should decay to zero at large distances in order to represent the wavefunction of an isolated atom or molecules. This subsection discusses two basis sets that are widely used, namely a localised basis set and a

plane wave basis set.

Localised Basis Sets

The localised basis set, which is commonly used in the quantum chemistry community, has the following form

$$\phi_\zeta(\vec{r}) = \phi_\zeta(r) Y_{lm}(\theta, \phi)$$

, where the radial part is represented in either of these two forms: Slater and Gaussian function.

$$\phi_\zeta(r) = \begin{cases} e^{-\zeta r} & \text{Slater} \\ e^{-\zeta r^2} & \text{Gaussian} \end{cases}$$

The major difference in describing the wavefunction in terms of the Slater and Gaussian function is the power of r in the exponent. The r dependence in the exponent in the Slater form has a better representation of the wavefunction than that of the r^2 dependence in the Gaussian function. However, there is a cusp at r = 0 in the Slater function. This causes a great difficulty in the calculations. Therefore, Gaussian type represention is computationally more efficient although more Gaussian functions are needed to construct a proper basis set than the Slater functions.

The larger the number of the basis functions usually has a better accuracy of the calculations. Nevertheless, this increases the amount of time spent in the calculations. A suitable number of basis set is often tested to find the optimum number balancing the tradeoff between the accuracy and the comsumption of computational resources.

Plane Wave Basis Sets

Another option is to consider the basis set in terms of plane wave. The plane wave basis set is very popular in solid state community involving the calculations of periodic systems. VASP is one of the programs (e.g. CASTEP, Abinit, Quantum ESPRESSO, etc.) utilizing the plane wave basis set method [93]. Fundamental knowledge about the plane wave basis set is discussed in details.

Brillouin zone (BZ) is a unit cell having highest symmetry in reciprocal space

(the first Brillouin zone is considered as the Wigner-Seitz primitive cell in the reciprocal lattice).

Let $\mathbf{a}_i$, i = 1,2,3, be a set of primitive lattice vectors, then the reciprocal lattice $\mathbf{b}_i$ can be written in terms of those three primitive vectors as

$$\mathbf{b}_1 = 2\pi \frac{\mathbf{a}_2 \times \mathbf{a}_3}{\mathbf{a}_1 \cdot (\mathbf{a}_2 \times \mathbf{a}_3)}$$

$$\mathbf{b}_2 = 2\pi \frac{\mathbf{a}_3 \times \mathbf{a}_1}{\mathbf{a}_1 \cdot (\mathbf{a}_2 \times \mathbf{a}_3)}$$

$$\mathbf{b}_3 = 2\pi \frac{\mathbf{a}_1 \times \mathbf{a}_2}{\mathbf{a}_1 \cdot (\mathbf{a}_2 \times \mathbf{a}_3)}$$

For any Bravais lattice vectors

$$\mathbf{r} = n_1\mathbf{a}_1 + n_2\mathbf{a}_2 + n_3\mathbf{a}_3,$$

the reciprocal lattice vector $\mathbf{G}$ is defined as

$$\mathbf{G} = h_1\mathbf{b}_1 + h_2\mathbf{b}_2 + h_3\mathbf{b}_3$$

Thus,

$$\mathbf{G} \cdot \mathbf{r} = h_i\mathbf{b}_i \cdot n_j\mathbf{a}_j \; \delta_{ij} = 2\pi(n_1h_1 + n_2h_2 + n_3h_3)$$

Due to periodicity,

$$e^{i\mathbf{G}\cdot\mathbf{r}} = 1,$$

$$\mathbf{G} \cdot \mathbf{r} = 2\pi N, \quad N \in \mathbf{Z}$$

Finally,

$$n_1 h_1 + n_2 h_2 + n_3 h_3 = N, \quad N \in \mathbf{Z}$$

In a periodic potential, the electronic wavefunction has to follow Bloch theorem. For a given band index n, the Bloch wavefunction has the following form

$$\psi_{nk}(\mathbf{r}) = e^{(i\mathbf{k}\cdot\mathbf{r})} u_{nk}(\mathbf{r}),$$

with the cell periodic term $\mathrm{u}_{nk}(\mathbf{r}+\mathbf{R}) = \mathrm{u}_{nk}(\mathbf{r})$ and $\mathrm{e}^{(i\mathbf{k}\cdot\mathbf{r})}$ is the plane wave in which $\mathbf{k}$ is the wave vector. The periodic function $\mathrm{u}_{nk}(\mathbf{r})$ can be expanded as

$$u_{nk}(\mathbf{r}) = \sum_{\mathbf{G}} c_G \; e^{[i\mathbf{G}\cdot\mathbf{r}]}$$

, where $\mathbf{G}$ is a reciprocal lattice vector.

Thus, the Bloch wavefunction is

$$\psi_{nk}(\mathbf{r}) = \sum_{G} c_{k+G} \; e^{[i(\mathbf{k}+\mathbf{G})\cdot\mathbf{r}]}$$

In principle, there are an infinite number of allowed vector $\mathbf{G}$. However, the coefficients c_{k+G} become smaller as the kinetic energies $|\mathbf{k}+\mathbf{G}|^2$ become larger. In other words, the coefficients c_{k+G} for the plane waves with smaller kinetic energies are more important than those with larger kinetic energies. Therefore, for practical reasons, the plane wave basis set are often truncated to include only the plane waves that have the kinetic energies that are smaller than some particular values. This value is set by the maximum value of the vector $\mathbf{G}$, called G_{cut}.

The kinetic energy of a plane wave with a wave vector $\mathbf{k} + \mathbf{G}$ is given as

$$E = \frac{1}{2}|\mathbf{k}+\mathbf{G}|^2$$

Hence, the value G_{cut} determines the maximum energy (cutoff energy, E_c) of the system as

$$E_c = \frac{G_c^2}{2},$$

and plane waves must satisfy the condition

$$\frac{1}{2}|\mathbf{k}+\mathbf{G}|^2 < E_c$$

$$|\mathbf{k}+\mathbf{G}| < G_{cut}$$

Only wavefunctions satisfying the above criteria will be included in the Fourier expansion of Kohn-Sham orbitals. The number of plane waves for a given E_c is approximately to be

$$N_{PW} \approx \frac{2^{3/2}V}{6\pi^2}E_c^{3/2}.$$

,where V_0 is the volume of the cell [Å^3], E_c is the cutoff energy [eV].

The plane wave basis set has several advantages over other types of basis sets: Slater and Gaussian basis set. These include

- the plane waves have a very good performance due to highly efficient algorithms for performing Fourier transforms allowing the calculations to work in both real and reciprocal space.

- the convergence of the physical properties can be easily tested and controlled by a single parameter (the cutoff energy).

- the kinetic energy operator is diagonal in the plane wave basis so that the kinetic energy can be quickly computaionally solved.

- the plane wave basis set provides the same accuracy at all points in space.

In this thesis, two different values of the plane wave cutoff energy (E_c): 875 eV and 500 eV were used in the static part (i.e. structural relaxations) and dynamic calculations (i.e. NEB method), respectively.

4.1.2 K-point Sampling

In general, the Kohn-Sham equations are needed to sum over the entire reciprocal space N_k k-points in the BZ, where $N_k \sim 10^{23}$ to obtain observable entities such as electron density or band structure energy. However, it is impossible to run over all the k-points. An approximation is made by introducing a weighted sum over few representative points. A systematic construction of those representative points is given as follows:

Let f($\mathbf{k}$) be a periodic function on the reciprocal lattice, the average value per cell becomes

$$\bar{f} = \frac{1}{N_k} \sum_k f_k(\mathbf{k}),$$

where N_k is the number of k-points.

This summation can be converted to an integral in a continuous variable in Fourier space having a volume per k point of Ω_{BZ}/N_k as

$$\bar{f} = \frac{1}{\Omega_{BZ}} \int_{BZ} d\mathbf{k} f_k(\mathbf{k}) = \frac{V}{2\pi^3} \int_{BZ} d\mathbf{k} f_k(\mathbf{k}),$$

where V is the volume of a primitive cell in real space.

The periodic function f can be expanded in a Fourier series of the Bravais lattice vectors by symmetrized plane waves A($\mathbf{k}$) as:

$$f(\mathbf{k}) = \frac{1}{\sqrt{V}} \sum_R f(\mathbf{R}) e^{-i\mathbf{kR}}$$

$$= \sum_{m=0}^{\infty} f_m A^m_{G_0}(\mathbf{k}), \quad A^m_{G_0}(\mathbf{k}) = \frac{1}{|g^m_0|} \sum_{g \in g_m} cos(\mathbf{k} \cdot g\mathbf{R}_m),$$

in which $g^m_0 \subseteq G_0$ is the subset of the orbit G_0, $A^m_{G_0}$ are the symmetrised plane waves with $A^0_{G_0}$ ($\mathbf{k}$) = 1, m counts the number of the orbit. These fulfill the orthonormality conditions:

$$\frac{1}{\Omega_0}\int_{BZ} d^3\mathbf{k} A^m_{G_0}(\mathbf{k}) = \delta_{m0}$$

$$\frac{1}{\Omega_0}\int_{BZ} d^3\mathbf{k} A^m_{G_0} A^n_{G_0}(\mathbf{k}) = \frac{1}{|g^m_0|}\delta_{mn}$$

Finally,

$$\bar{f} = \frac{1}{\Omega_{BZ}}\int_{BZ} d^3\mathbf{k} \sum_{m=0}^{\infty} f_m A^m_{G_0}(\mathbf{k})$$

Thus, $\bar{f}$ can be written as

$$\bar{f} = \sum_{i}^{N} w_i f(\mathbf{k}_i),$$

for N special points k_i, with weight w_i having normality condition ($\sum_i \mathrm{w}_i = 1$).

In the case of N = 1, the single most special point is the Baldereschi point [8], where the integration reduces to a single point. For N > 2, Monkhorst and Pack proposed a method for determining a uniform set of points, widely known as Monkhorst-Pack k-points [114], as:

$$\mathbf{k}_{i,j,k} = b_i\mathbf{b}_1 + b_j\mathbf{b}_2 + b_k\mathbf{b}_3$$

$$b_i = \frac{2i - q - 1}{2q}, i = 1, 2, ..., q.$$

where b_i are the reciprocal lattice vectors, q is a regular grid in the BZ. Note that when q = 2, this is the Baldereschi point. Typically, q is often set to be even numbers to avoid the highest symmetry points ($\mathbf{k} = 0$ point and the BZ boundary points).

The Monkhorst-Pack process is convenient for constructing equally spaced k-points. However, To find out the proper number of k requires an accuracy test. Finer meshes usually provide higher accuracy with the drawback of larger amount of time spent on the calculations. Therefore, convergence test in k-points is often

conducted to figure out the optimum number of k-point meshes.

In this thesis, we have performed the convergence tests in order to find out the optimum k-point meshes in the calculations. Results turn out that with the k-point meshes' density of $20/\text{Å}^{-1}$ is sufficient for all the gas hydrate systems studied in this thesis. This is also a typical value for the k-point meshes' density for the insulators.

4.1.3 Pseudopotentials

The wavefunctions of the electrons in a periodic crystal can be expanded in terms of plane wave basis sets. The size of the plane wave basis set required for a given system is far larger than that of a localised basis set. Especially in the vicinity of atomic nuclei, the orbitals oscillate very rapidly. A very large cut-off energy is required in order to describe this rapid oscillation. However, most of the space in the cell is much more smoothly oscillating. Therefore, most of the computational expense is wasted.

The electronic states of an atom can be classified into three states; core states, valence states, and semi-core states. For the core electrons, they are highly localised around an atomic nucleus and do not contribute to the chemical bonding. The valence electrons are delocalised and responsible for to chemical interaction. Semi-core states are localised but polarizable, so they do not contribute directly to the chemical bonding. Generally, the core states are not allow to relax according to the environment (frozen core approximation). Semi-core states are treated either as part of the frozen core or as part of the valence electrons depending on how important the contribution of them on the chemical environment. Due to orthogonalization of the valence electrons with respect to the core states, the wavefunctions of the valence states have an oscillatory behaviour with a number of node of n - l - 1, in which n is the principal quantum number and l is the angular momentum.

The pseudopotential concept is introduced in order to make the computations feasible. In the pseudopotential, the true wavefunction is replaced by a smooth, nodeless pseudo-wavefunction, which is not a solution to the orginal atomic problem. The pseudo-wavefunction is originated from a pseudo-atomic problem where the true potential is replaced by a pseudopotential. This fictitious potential replaces the effect of core electrons and the nuclear potential so that the valence

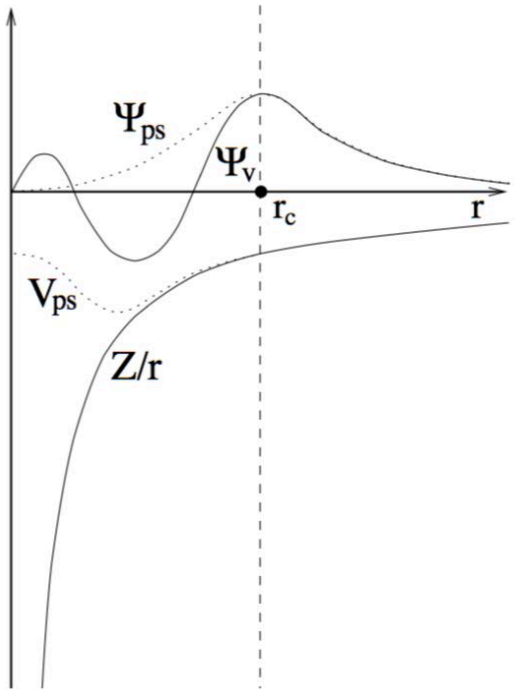

Figure 4.1 *Steep ionic potential ($\frac{Z}{r}$) causes rapid oscillations of the true wavefunction (Ψ_v). For numerical efficiency, pseudopotential (V_{ps}) is introduced. As a result of this, the rapidly varying (true) wavefunction Ψ_v is then replaced with smoother pseudo-wavefunction Ψ_{ps}. r_c is the cutoff radii determining the boundary between the core and the valence electrons.*

electron wavefunctions are smooth and nodeless inside a cut-off radius (r_c) from the nucleus, but remain unaffected outside that cut-off radius (shown in Figure 4.1). Modifying the valence electron wavefunctions near the nuclei to a rather more pleasant form should not affect the chemical bonding between atoms.

As illustrated in Figure 4.1, true wavefunction (Ψ_v) is substituted by pseudopotential wavefunction (Ψ_{ps}). Noting that there are no nodes in pseudopotential wavefunction. This smooth wavefunction has great computational benefits as it replaces the rapidly varying wavefunction inside the core regions by a slowly varying one. As a consequence ot this replacement, a lot fewer plane wave basis sets are required to describe the wavefunction inside the core region [17, 161].

Pseudopotential Transformation

In 1940, Herring introduced a concept of orthogonalized plane waves (OPWs) [64, 65], which were the antecedant of modern pseudopotential approaches. The

othogonalized form for the valence states ψ^v_{lm} can be expanded into a smooth part $\widetilde{\psi}^v_{lm}$ plus a combination of a localised function u_{lmj} as

$$|\psi^v_{lm}\rangle = |\widetilde{\psi}^v_{lm}\rangle + \sum_j B_{lmj}\,|u_{lmj}\rangle$$

Inspried by Herring, Philips and Kleinman [124] and Antoncik [4, 5] suggested a formal transformation of the OPW by inserting the expression of the valence wavefunction ψ^v_i into the valence eigenfunctions

$$\hat{\mathcal{H}}\,|\psi^v_i\rangle = [-\frac{1}{2}\nabla^2 + V]\,|\psi^v_i\rangle = \epsilon^v_i\,|\psi^v_i\rangle$$

Hence, the smooth part of the valence eigenfunctions becomes

$$\hat{\mathcal{H}}^{PKA}\,|\widetilde{\psi}^v_i\rangle = [-\frac{1}{2}\nabla^2 + \hat{V}^{PKA}]\,|\widetilde{\psi}^v_i\rangle = \epsilon^v_i\,|\widetilde{\psi}^v_i\rangle$$

In order to maintain the same eigenvalue, the potential V^{PKA} has the following form

$$\hat{V}^{PKA} = V + \hat{V}^R$$

,where $\hat{V}^R$ is a non-local operator, which can be written as

$$\hat{V}^R = \sum_j (\epsilon^v_i - \epsilon^c_j)\,|\psi^c_j\rangle\,\langle\psi^c_j|$$

$$\hat{V}^R\,|\widetilde{\psi}^v_i\rangle = \sum_j (\epsilon^v_i - \epsilon^c_j)\,\langle\psi^c_j|\widetilde{\psi}^v_i\rangle\,|\psi^c_j\rangle$$

In summary, the modification of the valence wavefunction to a smoother form requires the change in the potential. The modified potential (V^{PKA}) is stronger than the original nuclear potential (V) because V^R is always positive (repulsive). However, the pseudopotential V^{PKA} is smoother and weaker than the original potential V resulting in great computational advantages.

Modern pseudopotentials have been developed futher from the OPW trans-

formation. Ionic pseudopotentials, which concentrate only on the interacting valence electrons, is focused in this topic. Model potentials based upon the ionic pseudopotentials are constructed such that they have the same scattering properties as the pseudopotential operators. The potential of a nucleus and the core elctrons is replaced by a model potential, which is non-local and spherically symmetric. Therefore, each angular momentum l, m can be treat separately. The l-dependent model pseudopotentials $V_l(r)$ has the following features: the potential is repulsive inside the core region and has the potential of Z_{ion}/r outside the core region, Z_{ion} is a combination of the core electrons and nuclear potential [25].

There are several "ab initio" pseudopotentials, which are generated by calculations on atoms based on model potentials. These include: norm-conserving pseudopotentials, ultrasolf pseudopotentials, and projector augmented wave (PAW) method.

Norm-conserving pseudopotentials

In norm-conserving pseudopotentials, the pseudo wavefunction ψ^{PP} are normalized and are solutions of a model potential, which is chosen to reproduce the valence properties of an all-electron calculation. This is in constrast to the PKA method, where we concentrate only the smooth part of the valence function $\widetilde{\psi}$. Hence, different notations are used to clearly distinguish the difference between the two wavefunctions. The valence pseudo wavefunctions satisfy the usual orthonormality conditions as

$$\langle \psi_i^{\sigma,PP} | \psi_j^{\sigma',PP} \rangle = \delta_{i,j}\delta_{\sigma,\sigma'}$$

Originally proposed by Hamann, Schluter, and Chiang (HSC) in 1979 on the requirements for a good "ab initio" pseudopotential [29], Troullier and Martin have developed a method to construct the norm-conserving pseudopotentials for DFT [158].

Let's start with a spherically symmetric effective potential, $V_S(\vec{r}) = V_S(r)$. The all electron wavefunctions ψ_{nlm}^{AE} can be written as a separation of the angular part and the radial part as

$$\psi_{nlm}^{AE}(\vec{r}) = N_{nlm}\frac{u_{nl}^{AE}(\vec{r})}{r}Y_{lm}(\theta,\phi)$$

The radial equation for a spherical atom or ion is

$$\left\{ -\frac{1}{2}\frac{d^2}{dr^2} + \frac{l(l+1)}{2r^2} + V_S(r) \right\} u_l^{AE}(r) = \epsilon_l u_l^{AE}(r)$$

The band index n is omitted in the radial equation above because all valence electrons should be in the same electronic shell.

Inside a cut-off radius r_c, the radial wavefunction is replaced by a desirable analytical pseudo wavefunction R_l^{PP} as:

$$R_l^{PP}(r) = \begin{cases} R_l^{AE}(r) & r \geq r_c \\ r^l e^{p(r)} & r < r_c \end{cases}$$

$$R_l^{AE}(r) = u_l^{AE}/r,\ p(r) = \sum_{i=0}^{6} c_{2i} r^{2i}$$

The pseudo wavefunction R_l^{PP} should have the following features [29, 58, 110]:

1. All-electron and pseudo valence eigenvalues are the same: $\epsilon_l^{AE} = \epsilon_l^{PP}$.

2. All-electron and pseudo valence wavefunctions are the same beyond a chosen core radius: $R_l^{AE}(r) = R_l^{PP}(r),\ r > r_c$.

3. Smoothness: the logarithmic derivatives of the all-electron and pseudo valence wavefunction agree at r_c: $D_l R_l^{AE}(r) = D_l R_l^{PP}(r),\ r = r_c$.

4. Norm-conservation inside r_c, $\int_0^{r_c} dr r^2 |R_l^{AE}|^2 = \int_0^{r_c} dr r^2 |R_l^{PP}|^2$.

5. The first energy derivative of the logarithmic derivatives of the all-electron and pseudo valence wavefunction are equal at r_c: $dD_l^{AE}/d\epsilon = dD_l^{PP}/d\epsilon,\ r = r_c$ (D_l is a dimensionless logarithmic derivative).

6. Softness: $R_l^{PP}(r)$ does not have any nodes: $R_l^{PP}(r) \neq 0$.

7. The curvature of $R_l^{PP}(r)$ is zero at the origin: $d^2 R_l^{PP}(r)/dr^2|_0 = 0$.

The first four conditions suggest transferability of the pseudo wavefunctions. This is because the modifications are made only inside r_c so that there is no effect on the chemical bonding. From point 2 to 5 ensure the scattering phase of the all-electron and pseudo valence wavefunction are the same at the region beyoun r_c.

The latter two conditions provide a numerical suitability of the pseudo valence wavefunction.

Once inserting the pseudo wavefunction R_l^{PP} into the radial Kohn-Sham equation, the screened ionic pseudopotential can be obtained by rearranging the equation as follows

$$\left\{ -\frac{1}{2}\frac{d^2}{dr^2} + \frac{l(l+1)}{2r^2} + V_{l,scr}^{PP}(r) \right\} r R_l^{PP}(r) = \epsilon_l r R_l^{PP}(r)$$

$$V_{l,scr}^{PP}(r) = \epsilon_l - \frac{l(l+1)}{2r^2} + \frac{1}{2rR_l^{PP}} \frac{d^2 r R_l^{PP}}{dr^2}$$

In order to obtain the ionic (unscreened) pseudopotential $V_{l,en}^{PP}$, we need to substract the Hartree- and exchange-correlation interaction of the valence electrons from the screened ionic pseudo potential $V_{l,scr}^{PP}$.

$$V_{l,en}^{PP} = V_{l,scr}^{PP} - V_H(r, n_v^{PP}) - V(r, n_v^{PP})$$

The complete pseudopotential operator can be decomposed into local and non-local part, which can be written as

$$V_{l,en}^{PP} = V_{loc}^{PP}(r) + \sum_{l,m} |lm\rangle \, V_{l,non-loc}^{PP}(r) \, \langle lm|$$

In fact, $V_{l,non-loc}^{PP}$ is semi-local because it is non-local in the angular variables but local in the radial coordinate. For practical purposes, a complete non-local form is more preferable. Hence, Kleinman and Bylander suggested a formalism to replace the effect of the semi-local $V_l(r)$ by a separable operator $V_{non-loc}^{KB}$ as

$$V_{non-loc}^{KB} = V_{loc}^{PP} + \sum_{l,m} \frac{|\psi_{lm}^{PP} V_{l,non-loc}^{PP}\rangle \, \langle V_{l,non-loc}^{PP} \psi_{lm}^{PP}|}{\langle \psi_{lm}^{PP}| \, V_{l,non-loc}^{PP} \, |\psi_{lm}^{PP}\rangle}$$

,where $\psi_{lm}^{PP}(r) = R_l^{PP}(r) Y_{lm}(\theta, \phi)/r$ are the pseudo valence wavefunction.

Ultrasoft pseudopotentials

In plane wave basis sets, the wavefunctions are represented in a form of Fourier

functions. The fewer the number of Fourier components, the lower the cost of the calculation. Therefore, pseudopotentials that create "smooth" pseudo wavefunctions is computationally preferable. One can maximize the smoothness of the wavefunctions by minimizing the range in Fourier space needed to describe the valence properties. However, norm-conserving pseudopotentials sometimes cannot produce smooth pseudo wavefunctions, especially in the case of first-row elements e.g. carbon or oxygen. This is because the 2p valence states are localised near the nuclei. To overcome this issue, David Vanderbilt proposed a new approach known as ultrasoft pseudopotentials [161].

In ultrasoft pseudopotentials, the scattering properties of the all-electron and the pseudo-atom does not necessarily agree at the eigenvalue ϵ_l, but at an arbitrary energy $\widetilde{\epsilon}_l$, which preserves the same bonding properties of the valence electrons. Thus, there is no requirements for the pseudo wavefunctions to have the norm-conservation feature becuase the wavefunctions are not normalizable if $\widetilde{\epsilon}_l$ is not an eigenvalue.

The scattering properties can be fixed to agree at an arbitrary energy $\widetilde{\epsilon}_i^l$. At different energies $\widetilde{\epsilon}_i^l$, pseudo wavefunctions $\widetilde{\psi}_i$ can be constructed from all-electron calculations. The generalised non-local potential operator can be written as

$$V_{non-loc}^l = \sum_{i,j} B_{i,j}^l \left|\beta_i^l\right\rangle \left\langle\beta_j^l\right| = \sum_j \left|\chi_j^l\right\rangle \left\langle\beta_j^l\right|$$

$$\left|\beta_i^l\right\rangle = \sum_j (B^l)_{ji}^{-1} \left|\chi_i^l\right\rangle$$

A matrix $B_{i,j}^l = \langle\widetilde{\psi}_i^l|\chi_j^l\rangle$ and the states $|\chi_i^l\rangle$ are the results of the non-local pseudopotential acting on the pseudo wavefunction $|\widetilde{\psi}_i^l\rangle$

$$\left|\chi_i^l\right\rangle = V_{non-loc}^l \left|\widetilde{\psi}_i^l\right\rangle = (\widetilde{\epsilon}_l^i - T_e - V_{loc}) \left|\widetilde{\psi}_i^l\right\rangle$$

The full pseudopotential V_{ps} can be obtained via

$$V_{ps} = V_{loc} + V_{non-loc}$$
$$V_{non-loc} = \sum_l V_{non-loc}^l$$

At any arbitrary value of $\widetilde{\epsilon}_i^l$, $V_{non-loc}^l$ provides a correct scattering phase for the pseudo wavefunctions $\widetilde{\psi}_i^l$ and their energy derivative.

Let's introduce a generalised eigenvalue problem. A non-zero difference in the norms of the all-electron ($|\psi_j^l\rangle$) and pseudo wave states ($|\widetilde{\psi}_j^l\rangle$) can be written in a form of a matrix elements Q_{ji}^l as

$$Q_{ij}^l = \langle \psi_i^l | \psi_j^l \rangle_R - \langle \widetilde{\psi}_i^l | \widetilde{\psi}_j^l \rangle_R$$

These norms are only determined to a radius R, which is often larger than r_c, because both $|\psi_j^l\rangle$ and $|\widetilde{\psi}_j^l\rangle$ are usually not normalised.

A new non-local ultrasoft potential that operates on a smooth pseudo state $|\widetilde{\psi}_j^l\rangle$, can be defined to be

$$V_{non-loc}^{US} = \sum_{i,j} D_{i,j}^l \, |\beta_s\rangle \, \langle \beta_s|$$

,where

$$D_{i,j}^l = B_{i,j}^l + \widetilde{\epsilon}_j^l Q_{i,j}^l$$

For each reference atomic state i, the smooth pseudo states $|\widetilde{\psi}_i^l\rangle$ are solutions of the generalized eigenvalue problem

$$\hat{\mathcal{H}} \, |\widetilde{\psi}_i^l\rangle = \widetilde{\epsilon}_i^l \hat{S} \, |\widetilde{\psi}_i^l\rangle$$

,where

$$\hat{\mathcal{H}} = T_e + V_{loc} + V_{non-loc}^l$$

and an overlap operator $\hat{S}$ is defined as

$$\hat{S} = \hat{1} + \sum_{i,j} Q_{ij}^l \, |\beta_i^l\rangle \, \langle \beta_j^l|$$

,which β_i^l are projectors that form a dual basis with the pseudo reference states.

$$\langle \beta_j^k | \widetilde{\psi}_j^l \rangle = \delta_{ij} = \begin{cases} 1 & r \leq r_c \\ 0 & r > r_c \end{cases}$$

Therefore, the overlap operator $\hat{S}$ is different from unity only inside the cut-off radius, r_c.

The Projector Augmented Wave method

Like the ultrasoft pseudopotentials, the projector augmented wave (PAW) method uses the projector operator and auxiliary localised functions to reformulate the OPW approach [17]. However, the difference is that PAW approach still keep the full all-electron wavefunction, which varies very rapidly near the nucleus. Thus, the integrals of smooth functions and localised part are evaluated separately. Radial integration over muffin-tin spheres is used to obtain the contribution from the localised function. PAW is not a pure pseudopotential method, but it is a technique with advanced algorithms to find the solution of the generalized eigenvalue problem [72, 94].

In ultrasoft pseudopotentials, the overlap operator S mediates between full and pseudo wavefunctions as

$$\langle \psi_i^l | \psi_j^l \rangle = \langle \widetilde{\psi}_i^l | \, S \, | \widetilde{\psi}_j^l \rangle$$

Similarly, a linear transformation operator $\mathcal{T}$, which transforms the pseudo wavefunction $|\widetilde{\psi}\rangle$ to the all-electron wavefunction $|\psi\rangle$, is introduced in PAW method as

$$|\psi_i^l\rangle = \mathcal{T} \, |\widetilde{\psi}_i^l\rangle$$

$$\langle \psi_i^l | \psi_j^l \rangle = \langle \widetilde{\psi}_i^l | \, \mathcal{T}^\dagger \mathcal{T} \, | \widetilde{\psi}_j^l \rangle \, , \quad S \equiv \mathcal{T}^\dagger \mathcal{T}$$

Thus, the overlap operator S is anologous to the square of the transformation operator $\mathcal{T}$.

To ensure that $|\widetilde{\psi}\rangle$ and $|\psi\rangle$ differ only in the regions vicinity to the ion cores, the transformation operator $\mathcal{T}$ has the following feature,

$$\mathcal{T} = \hat{1} + \hat{\mathcal{T}}_0$$

, where $\hat{\mathcal{T}}_0$ is non-zero only within some spherical augmentation regions close to the nucleus.

The expansion of each smooth function $|\widetilde{\psi}\rangle$ in partial waves i within each sphere can be written as

$$|\widetilde{\psi}\rangle = \sum_i c_i \, |\widetilde{\psi}_i\rangle$$

The corresponding all-electron function is

$$|\psi\rangle = \mathcal{T} \, |\widetilde{\psi}\rangle = \sum_i c_i \, |\psi_i\rangle$$

Hence, the full wavefunction in all space can be written as

$$|\psi\rangle = |\widetilde{\psi}\rangle + \sum_i c_i \Big\{ \, |\psi_i\rangle - |\widetilde{\psi}_i\rangle \, \Big\}$$

The transformation operator $\mathcal{T}$ is linear, the coefficient c_i can be obtained by a projection in each sphere from some projection operators $\widetilde{p}$

$$c_i = \langle \widetilde{p}_i | \widetilde{\psi} \rangle$$

, where $\langle \widetilde{p}_i | \widetilde{\psi}_j \rangle = \delta_{ij}$

Thus, the transformation operator can be written as

$$\mathcal{T} = \hat{1} + \sum_i (|\psi_i\rangle - |\widetilde{\psi}_i\rangle) \, \langle p_i|$$

Each all-electron wavefunction can be expressed in three parts:

$$|\psi\rangle = \mathcal{T} \, |\widetilde{\psi}\rangle = |\widetilde{\psi}\rangle + |\psi^1\rangle - |\widetilde{\psi}^1\rangle$$

$$|\psi^1\rangle = \sum_i |\psi_i\rangle \langle p_i|\widetilde{\psi}\rangle$$

$$|\widetilde{\psi}^1\rangle = \sum_i |\widetilde{\psi}_i\rangle \langle p_i|\widetilde{\psi}\rangle$$

The fictitious wavefunction $|\widetilde{\psi}\rangle$ is soft is defined in all of space. This pseudo wavefunction deviates strongly from the all-electron wavefunction $|\psi\rangle$ at the regions close to nuclei. Thus, a correction is made by the contributions from both $|\psi^1\rangle$ and $|\widetilde{\psi}^1\rangle$ (index "1" refers to the "one-center" localisation).

PAW pseudopotential implemented in VASP program is used in this thesis. Two versions of PAW pseudopotentials depending on the amount of atomic cutoff radii are applied in this work, namely the standard one and the "hard" PAW. For the static calculations in both noble gas hydrate and hydrogen hydrate system, the "hard" pseudopotential is employed. The standard pseudopotential is implemented in the dynamic calculations of the hydrogen hydrates.

4.2 Ground state properties of materials

4.2.1 Geometry Optimisation

This subsection discusses ground state properties of the system (i.e. calculations performed at zero K temperature). In order to find the ground state property of materials, one needs to optimise the geometry of considered materials first. This can be done by relaxing the nuclear positions from an initial state by minimising the forces.

A single SCF cycle yields the total energy of the system, which depends on the nuclear positions ($\mathbf{R}_a$) as

$$E(\mathbf{R}_a) =< \Psi_{KS}|H_e|\Psi_{KS} >,$$

providing the force acting on a given atom as

$$F_a = -\nabla_a E(\mathbf{R}_a)$$

The force described in the gradient function of energy above can be solved by numerical methods (such as a finite-difference approximation). However, this requires more computational steps to find the energies ahead and after the considered position. A more elegant method proposed by Hellmann and Feynman is widely used in the fields. The Hellmann-Feynman theorem states that, for any Hamiltonian H that depends on a parameter λ, the derivative of its expectation value is given as

$$\frac{\partial E}{\partial \lambda} = \frac{\partial}{\partial \lambda} < \Psi | H | \Psi > = < \Psi | \frac{\partial H}{\partial \lambda} | \Psi >$$

According to the Hellmann-Feynamn theorem, the gradient of the energy can simply be retrieved by evaluating the gradient of the Hamiltonian H. If λ corresponds to nuclear coordinates ($\mathbf{R}_a$), the gradient of the operator can be evaluated at the end of every SCF loop to obtain the forces on all atoms. Geometry relaxation is then performed by following the gradients to the nearest local minimum.

Not only the forces but also the stresses of the system are taken into account if doing volume relaxation. By obtaining the stress tensors, cell shape can be relaxed. Thus, we can do constant-pressure calculations.

The energy convergence criteria in this thesis is smaller than 10^{-7} eV/unit cell, with the net forces are smaller than 2 meV/Å.

4.2.2 Equation of State

The equation of state (EOS) is of interest when considering mechanical properties of materials. At ground state (no temperature effect), the total energy of the system can be written as a function of volume, E = E(V). By knowing the equation of state, other properties can be determined, such as pressure p and bulk modulus B:

$$p = -\frac{\partial E}{\partial V}$$

$$B = -V\frac{\partial p}{\partial V}$$

The equilibrium volume (V_0) is determined when $p(V_0) = 0$ ($p = -\frac{\partial E}{\partial V} = 0$). The information on both V_0 and B_0 (the bulk modulus at $p = 0$) can be compared with experiment, which can be measured quite accurately through diffraction methods and elastic response measurements. Additionally, both properties can be easily computed. In practice, by changing the lattice parameters (i.e. varying the volume), the energies corresponding to those lattice parameters can be obtained. E-V curve is usually plotted and fitted to an analytical expression. There are variety of EOS fits: these are Murnaghan-EOS [118], Birch-Murnaghan-EOS [15], and Vinet-EOS [164].

4.2.3 Ground State Enthalpy Calculation

By performing the structure relaxation, its ground state energy can be retrived. Combining with applied pressure, the ground state enthalpies ($H = E + P \cdot V$) of all possible phases in the system are explored.

For example, if we would like to determine the stability of a binary compound system (A_nB_m), the formation enthalpy of each phase (i.e. each has different stoichiometries) is computed and compared to pure constituents as follows:

$$\Delta H_f(A_nB_m) = H_f(A_nB_m) - n \cdot H_f(A) - m \cdot H_f(B).$$

Convex Hull Plot

The convex hull plot is a useful way to compare the enthalpies of all the phases having different stoichiometries. All the points on the convex hull are stable against the decomposition reactions. The tie line connects the points representing stable phases on the convex hull. Points located above the tie line are meta-stable and eventually decompose into the unary or binary phases which are more energetically favourable. Other points having positive relative enthalpies of formation are unstable with respect to the based constituents, and of course, these points are far less energetically favourable than the points on the convex hull.

Figure 4.2 demonstrates an example of a convex hull plot of three compunds: A, B, and C at two pressures: 1 bar (small dots) and 1 kbar (large dots). Their relative enthalpies with respect to the based constituents are plotted in the y axis

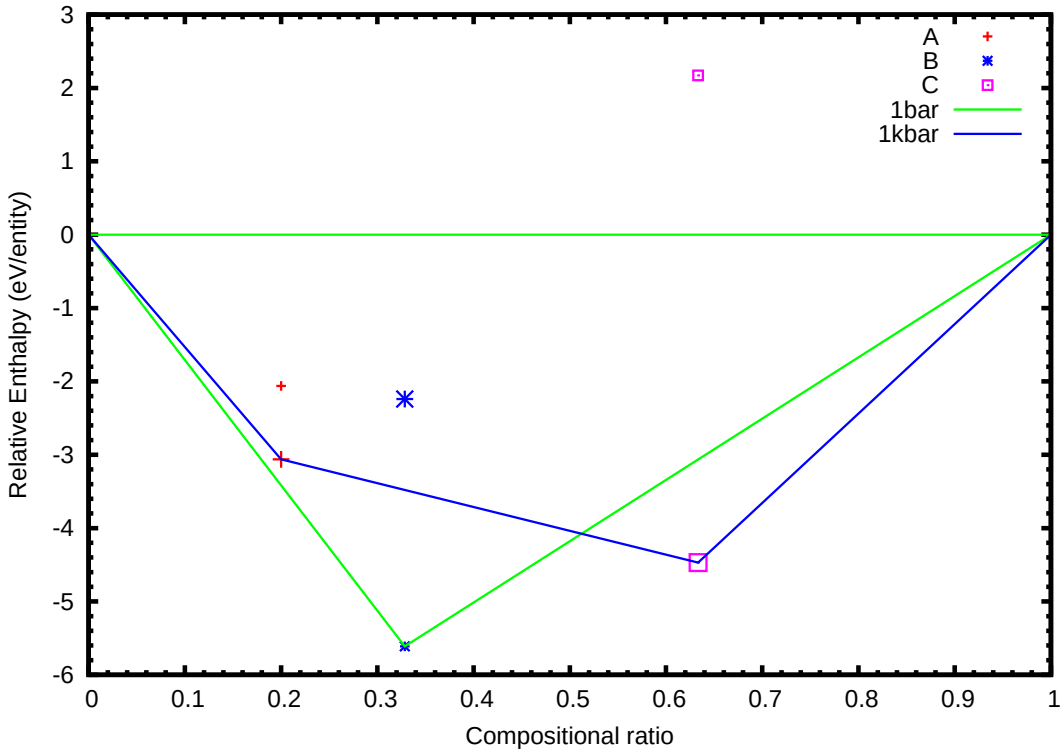

Figure 4.2 *Convell Hull Plot of the compound A, B and C at two pressures: 1 bar (small dots) and 1 kbar (large dots). The tie lines that connect stable phases at 1 bar and 1 kbar are shown in green and blue color, respectively. At 1 bar, the constituent B is the stable phase. Whereas, the compound A is metastable and the compound C is unstable. At 1 kbar, both compound A and C are stable; whereas, compound B is metastable.*

versus their compositional ratios in the x axis. At 1 bar, Only compound B is stable with respect to the based constituents, as its location is at the convex hull (green line). Compound A is metastable because it is situated above the green tile line; whereas the compound C is unstable because it has positive enthalpy of formation. At 1 kbar, stable phases are connected by blue tie line. Thus, both compound A and C are stable at this pressure. The point representing the compound B is above the blue tie line yet still have negative formation enthalpy. Thus, compound B is metastable at 1 kbar.

Chapter 5

Proton Ordering in water networks

Governed by the "ice rule" or the Bernal-Fowler rules [13] in water ice structures, each oxygen forms two covalent bonds to two hydrogens, in which each of these two hydrogens forms a hydrogen bond to its neighbouring oxygen. This leads to precisely one hydrogen between each pair of oxygen atoms.

Because of that restriction, the number of arranging the hydrogen bonds to the oxygen lattice in order to construct the water ice networks is limited. In 1935, Linus Pauling [121] suggested $(3/2)^N$ different ways of assigning hydrogens in an ice Ih lattice, where N is the number of water molecules. Confirmed later by Giauque and Stout [48] who measured the entropy of ice Ih near 0 K to be $NK_B\ln(3/2)$. This remarkably accurate pretiction by Pauling is verified when compared to the exact results of 1.5069^N [119]. This non-zero entropy near 0 K implies a nearly random arrangements of protons. The mysterious question whether the phase transition to the fully proton-ordered structure exists is still unsolved. Can we find the proton-ordered structure if the phase is not fully solved? Can we test the proton disordered-ordered phase transition if we know the structure? These unanswered questions are theoretically possible to be investigated if having enough information, i.e. be able to construct the hydrogen-bonded networks. One possibility is to implement the graph theory to count how many ways of assigning the hydrogens to the ice networks. Thus, this section is mainly focus on how to assign hydrogens to the experimentally known oxygens' positions forming a complete host water network.

5.1 Hydrogen disorder and defects in pure ice structures

Recalling to the pure ice phases mentioned in Chapter 2, at least eighteen crystalline phases of ice are characterized and reported in the literature, and they are enumerated with Roman numerals. Their place in the phase diagram of water is shown in Figure 5.1.

Those not shown in Figure 5.1 are ice I_c, IV, X, XVI and XVII. Ice-I_c is a cubic phase located within the stability region of I_h. Ice-IV phase is a proton-disordered network situated in the stability region shared between ice-III and ice-II; however, there is no proton-ordered counterpart for this ice-IV phase. Unlike other ice phases where the H_2O networks are formed by hydrogen bonds, ice X acts like an ionic crystal, in which their oxygen atoms are connected by symmetric O-H-O bonds. Additionally, its stability region is beyond this plot (> 10 GPa).

As have already mentioned in Chapter 2, there are other ice phases under negative pressure regions. Ice XVI was synthesized by Dr. Werner Kuhs from the University of Gottingen in 2014 by removing the neon guest molecules out of its host water networks based on sII network [41]. The most recent ice XVII phase was obtained by removing the hydrogen gas molecules from the S_χ host network in vacuum [99].

As illustrated in Figure 5.1, there are several ice phases, which can be classified by their protonic configurations to either proton-ordered or proton-disordered structures. In fact, the five phases that share a phase boundary with the liquid (ice I_h, III, V, VI, and VII) and ice-XII, are orientationally disordered and transform to proton-ordered phases (ice XI, IX, XIII, XV, VIII, and XIV respectively) when cooled. Ice Ih is the phase commonly created when cooling water at ambient pressure (h refers to the hexagonal close-packed positions of the oxygens). The remaining four phases are Ice I_c, II, IV, and X. Ice I_c is the metastable phase of Ice Ih in which the arrangement of oxygen positions is cubic diamond instead of the hexagonal lattice of Ice I_h. Ice II is the only known ice-structure that occurs in a hydrogen-ordered configuration only.

The summary of the proton-disordered and corresponding proton-ordered phases is listed in Table 5.1. Ice X is of course not included in the table because its structure cannot be thought of in terms of water molecules like the other ice

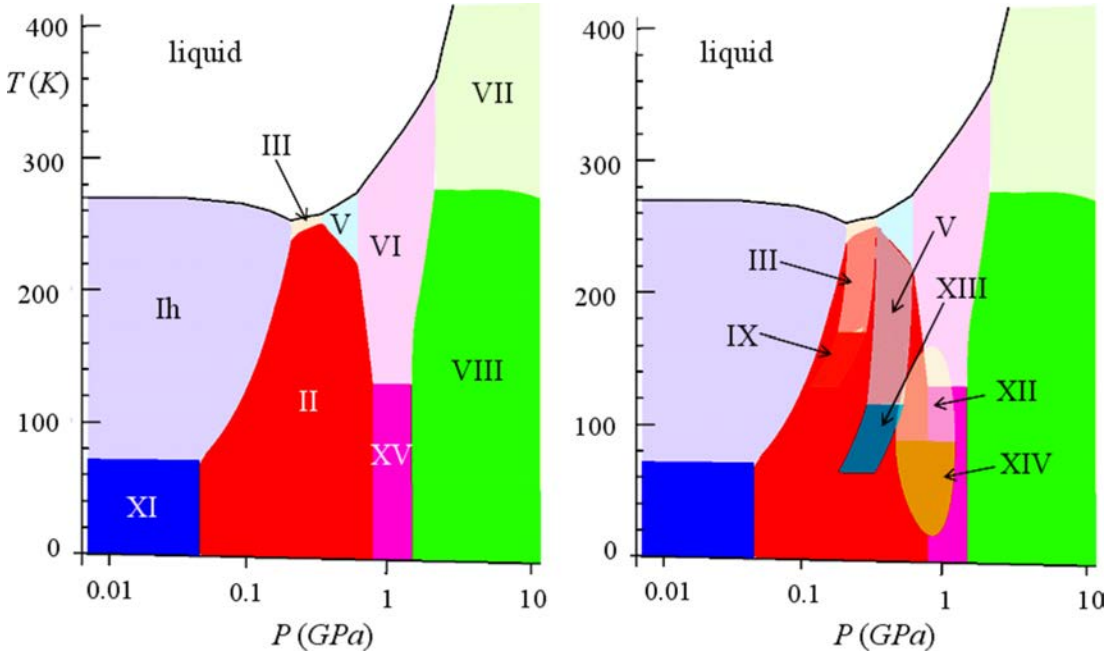

Figure 5.1 *Phase diagram of pure water as a function of pressure and temperature showing stable phases (left) and some meta-stable phases, which will eventually revert to an equilibrium phase (right). [1]*

structures. Both recent discovered ice phases: ice XVI and ice XVII are not considered in this part either because they are formed under negative pressure, and hence are out of the scope of this study.

The summary of the structural data (i.e. space group, unit cell parameter, number of water molecules per unit cell, etc.) of all seventeen crystalline phases of water are tabulated in Appendix B.

Proton-disordered modifications	Corresponding proton-ordered modifications
Ice I_h	Ice XI
Ice I_c	-
-	Ice II
Ice III	Ice IX
Ice IV	-
Ice V	Ice XIII
Ice VI	Ice XV
Ice VII	Ice VIII
Ice XII	Ice XIV

Table 5.1: Proton-disordered and proton-ordered modifications of ice.

Glass transition has been observed when the ice I_h is cooled down to around 110 K from its melting temperature [97]. This prohibits the transition to a proton-ordered phase. However, when doped with impurities such as KOH, the transition to the proton-ordered phase occurs at 72 K [152]. These impurities help breaking the hydrogen bonds and rearranging the bonds to the properly proton-ordered network [82].

There are three main types of point defects in ice (molecular, impurity, and protonic defects).

i) The molecular defects are defects in which whole water molecules disappear from the normal sites, and left those sites vacant - "vacancy defects"; or defects in which whole water molecules occupy the cavities formed by the hydrogen bonding networks in ice - "interstitial defects". Because of the large size of the water molecules, the most probable sites for the interstitial defects are in the center of

the hexagonal rings or in the middle between those two hexagonal rings. The addition of water molecules by those interstitial defects also has to follow the "ice rule" i.e. forming hydrogen bonds to the surrounding water lattices. The molecular defects are the largest point defects, which require high amount of energy to dislocate the whole water molecules from their normal sites so the chance of occurance is very small if the temperature is not high enough.

ii) The impurity defects occur when the elements of the water molecules are substituted with other atomic types. For instance, if using HF as a catalyst, the fluorine atom may replace the oxygen atom, creating H-F bond instead of the normal H-O-H bond. Moreover, the impurity defects also include the case of interstitial atoms inserted in the empty space. To induce the impurity defects, it is also required high amount of energy needed to break the covalent bonds of the water molecules in case of substitional defects; or to overcome the strain effect from neighboring atoms in the case of interstitial defects.

iii) The protonic defects are the most common defects found in ice, which can be divided into two main types namely Bjerrum and ionic defects as shown in Figure 5.2. These two types of defects are induced via violating the Bernal-Fowler rules by allowing no hydrogen (L defect) or two hydrogen atoms (D defect) along the O-O connection, and by ionizing the water molecule to H_3O^+ or OH^- ion. Such defects will introduce a frustration of the hydrogen bond network, while also opening up low-barrier pathways to rearrangement, so that the system transforms into a lower energy state or ordered structure. To emphasize on the effect of protons in the ice network which obeys the Bernal-Fowler rules, the Bjerrum defects are specifically proposed to the ice structures to distinguish from the conventional point defects such as interstitials and vacancies. Since the formation enthalpies of these protonic defects are smaller than the other two point defects listed above, the hydrogen-ordering process upon mixing with the dopant is normally governed by these types of defects. The dopants and their corresponding defects are listed in Table 5.2.

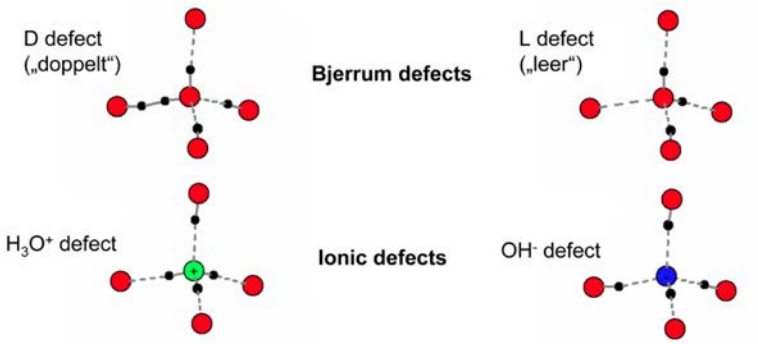

Figure 5.2 *Possible point defects in ice structures: Bjerrum (top) and ionic defects (bottom).*

Dopant	Defect
HF	H_3O^+
HCl	H_3O^+
HF	L
HCl	L
NH_3	OH^-
NH_3	D

Table 5.2: Dopants and their corresponding defects.

The protonic configurations in ice have significance effects in terms of their properties and energies. The variation in hydrogens' orientation can change the dielectric properties of ice, such as forming a ferroelectric state if the net dipole moment does not vanish. Recent computational studies showed that the difference between the two lowest cohesive energies, which have different symmetries ($I4_1md$ and $P4_12_12$) of the proton-ordered cubic ice (ice Ic), is 5 meV/ water molecule [129]. Therefore, the proton ordering's study is of significance as it can also affect the stability of the ice phases.

Furthermore, this protonic configurational effect may also alter the stabilities of the gas hydrates. Nonetheless, little research has been conducted on the effect of different proton configurations in the gas hydrate systems, especially in DFT calculations. Thus, this Chapter is devoted to the configurational effect's study of pure water ice structures, and hence, we can examine the effect of having different protonic configurations in the gas hydrates in the following Chapters.

5.2 Finding proton configurations for atomistic calculations

In order to prepare the input of the ice structures, one of the most difficult parts is to assign the hydrogen postions into the ice network as the total different ways of assigning hydrogen in the hydrogen bonds increases with system size. The completely distinct hydrogen configurations in ice Ih has been predicted to be $(3/2)^N$, where N is the number of water molecules [121]. Graph theory method is therefore commonly used together with some other computational algorithms (such as Monte-Carlo sampling), in order to explore the possible configurations of hydrogen bond networks. Several proton-ordered/disordered phase transitions on various systems such as Ih/XI, VII/VIII [90, 143], III/IX [88] and V/XIII [89] have been explained successfully based on the graph invariant topology of ice structures.

The following section will briefly describe the graph invariant topology method proposed by a research group at Ohio State University in the US, leaded by Prof. Sherwin J. Singer [97, 142]. The graph invariant topology code is also available on their webpage [1], which I use this code to generate the hydrogen bonds to form the host water structures for sT hydrates.

There are many ways of assigning hydrogens to form hydrogen bonds as shown in Figure 5.3. Thus, for mathematical convenience, directional graphs are used to specify the direction of protons pointing from donors to acceptors. A bond variable (b_r) is then introduced, having values +1 or -1 according to the bond points along or opposite to an arbitrarily pre-defined direction for that bond. Topology of hydrogen bonds is described in terms of the bond variables (b_r). Such that polynomial sum in bond variables are referred as "graph invariants". Linear polynomials in the b_r are called "first-order" graph invariants. Quadratic polynomials are "second-order" graph invariants, and so on.

The first-order graph invariant (I_r) is constructed by applying a symmetric representation, $\hat{G}$, which equals to

$$I_r = \hat{G}(b_r) = \frac{1}{|G|} \sum_{\alpha=1}^{|G|} g_\alpha(b_r)$$

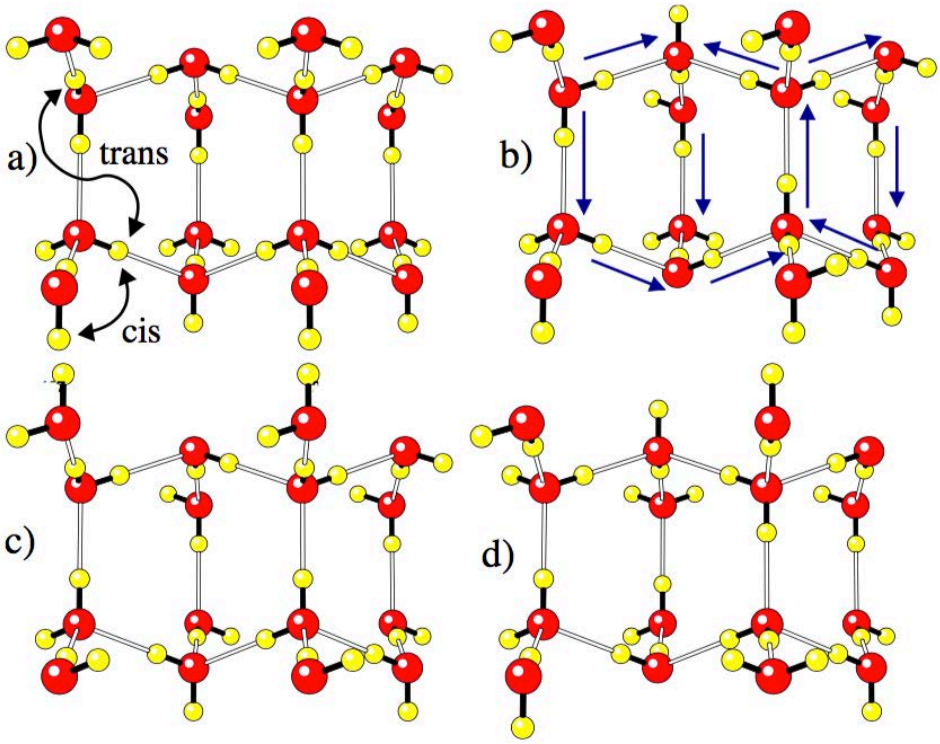

Figure 5.3 *A sample of four possible arrangements of hydrogen bonds within a 16-water orthorhombic unit cell of ice I_h. Cis and trans hydrogen bonds are defined as the protons' locations are on the same or the opposite side of the hydrogen bond respectively as shown in (a). Directed graphs are used to show the directions of the hydrogen bonds pointing from donors to acceptors, illustrated in (b).*

In the equation above, g_α is a symmetry element of the point group G, $|G|$ is the number of symmetry elements in the group.

Higher order graph invariants' terms (I_{rs}, I_{rst}, ...) can be constructed in the similar way as follows,

$$I_{rs} = \hat{G}(b_r b_s) = \frac{1}{|G|} \sum_{\alpha=1}^{|G|} g_\alpha (b_r b_s)$$

The energy of the hydrogen bond topology is obtained by

$$E(b_1, b_2, ..., b_n) = \sum_r \alpha_r I_r(b_1, b_2, ..., b_n) + \sum_{rs} \alpha_{rs} I_{rs}(b_1, b_2, ..., b_n) + ...$$

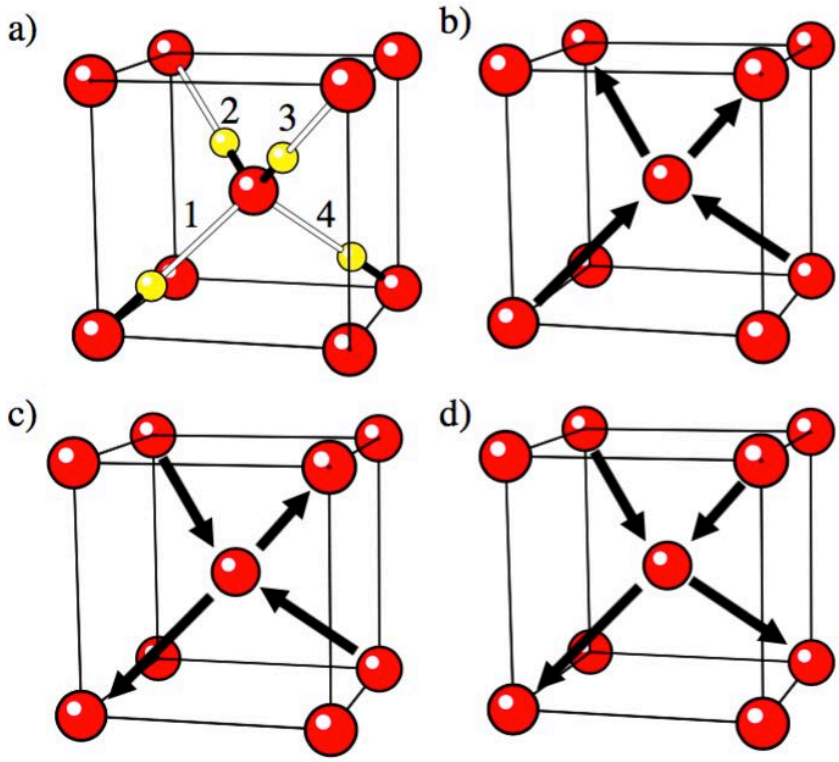

Figure 5.4 *Four configurations of a 2-water primitive unit cell of ice VII. The hydrogen bonds are labeled from 1 to 4 to provide a bond variable, b_r.*

In practice, the α coefficients are feasibly determined for small unit cells. Since it has been proved that the invariants for small unit cells are automatically invariants for larger cells, the energy formalism here can be applied for larger cells as well. Note that the expansion higher than the second order term are negligible. Kuo et al [98] have shown that second-order invariants is sufficient for generating a projection on a small number of nearby bond pairs for pure water ice phases. For example, the ice I_h system, three second-order invariant functions provided an accurate result for the energy [142].

For valid water ice networks, the first-order graph invariant (I_r) must equal to zero. In other words, the sum of all bond variables (b_r) for valid water ice network, which obeys ice rule, is zero. For example, Figure 5.4 depicts four possible configurations in a 2-water primitive cubic unit cell of ice VII. Therefore, the first step the program does is to assign the +1 and -1 to every bond variable (b_r) in the unit cell. Then, based on this criteria, those configurations having non-zero first-order graph invariant (I_r) are excluded from the samples. Only those configurations with zero first-order graph invariant are used for further

calcalations i.e. higher order graph invariant terms. Because the energy of the system is related to the bond variables (b_r), information on the second-order graph invariant terms are very useful to catagorize the ice networks whether they are new structures or not.

Practically, the main input parameters for this programs include 1. the oxygen lattice parameters, 2. the maximum number of invariant samples, 3. unit cell size, and 4. symmetry of the unit cell.

Hydrogen bonds are generated base on the oxygen lattice positions. The maximum number of samples sets the maximum number of configurations performed in this program since there are tremendous amount of ways (2^N) to assigned +1 and -1 to the bond variable (b_r). The unit cell size limits the amount of the bond variable (b_r) to be considered only within that unit cell. Finally, specifying the symmetry will constraint the search to only obtain the water ice network to that symmetry and its subgroup.

Another program that was used in my thesis is developed by my supervisor, Dr. Andreas Hermann, called "exhaustive tree-based search with backtracking". This code utilizes a graph-theory-based method that is tree-based approach in order to search for different hydrogen bonded networks. At the beginning, the code assign a hydrogen bond to connect two oxygen lattices. The next step is to assign the hydrogen to one of those two oxygen atoms to its oxygen neighbours, and so on. Therefore, this code is like a tree-based method because the way the program assigns protons depends upon the path.

Most of the proton-ordered structures used in this thesis are constructed by using this program. Although, the code is exhaustive, it does check the symmetry of the finally generated configurations. This helps sorting out the configurations based on symmetry.

5.3 Enthalpy results of different protonic configurations in various water ice phases

The water ice phases studied in this Chapter have been experimentally proven to be hosts to some guest species, which sit on specific sites. Hence, we search for the best candidate structure of each water ice phase by constructing the hydrogen-

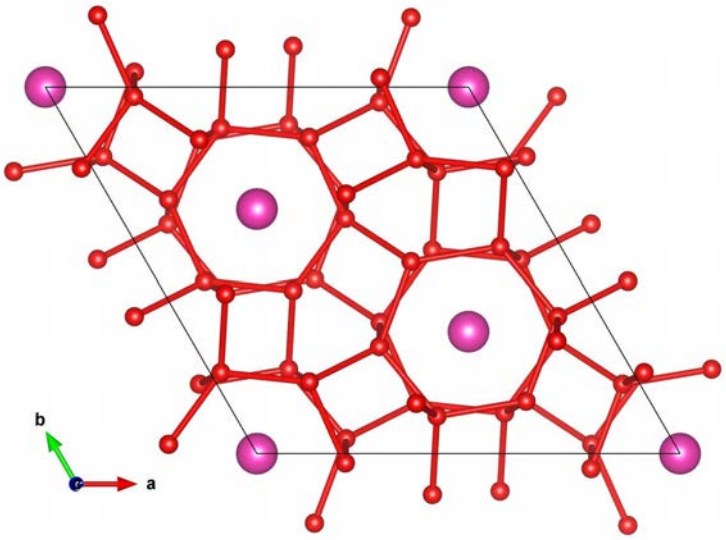

Figure 5.5 *Picture of ice-II network, viewed along the channel along c axis. O-O bonds are indicated. Six possible sites for the guest species are allowed in this network, two sites per each channels.*

bonded networks to known host nuclear lattices of water ice and calculating their enthalpies. The structure, which has the lowest enthalpy in each ice phase, is used as a host water network for the gas hydrates studied later.

Thus, this section contains the enthalpy results of various ice phases with several proton-ordered configurations generated by using both our graph-theory-based program and a graph-invarient topology program proposed by Prof. Singer's research group.

Ice-II

Unlike other ice, ice-II is the only ice phase that is found only proton-ordered in experiment. Figure 5.5 illustrates the ice-II structure in a hexagonal unit cell. In the hexagonal unit cell, there are 36 water molecules with six possible sites for the guest species, 2 sites per channel, allowed in this network. Those two guest sites in the same channel situate almost on top of each other if viewing along c-axis.

Another way of representing ice-II structure is by using a rhombohedral unit cell because the Bravais lattices in the hexagonal crystal family can be described by rhombohedral axes (a = b = c, $\alpha = \beta = \gamma \neq 90°$). This rhombohedral unit cell contains 12 water molecules with two possible guest sites. Thus, the rhombohedral unit cell was used in the study of different proton configurations

in ice-II to save computational resources.

The mystery on why the ice-II phase are experimentally found to exist in only the proton-ordered networks is still unclear and intriguing. Thus, this section contains the computational results on other proton-ordered structures besides the naturally found one. Those proton-ordered structures were generated by our reserch group using graph-theory-based program in order to assign protons to the ice-II host oxygen lattices and construct complete water ice networks, i.e. obeying the ice rule. Here, 22 distinct proton-ordered structures were computationally produced based originally on a primitive unit cell with R-3 symmetry. Their relative enthalpies with respect to the structure having the lowest enthalpy are shown in Figure 5.6, calculations were performed using rPW86-vdW2 functional. Configuration #1 is the experimentally found ice-II phase. It is clear that the configuration #1 has the lowest enthalpy compared to our other computationally generated configurations. According to the results in Figure 5.6, the energetic spread between the structure having the lowest and highest entahlpy is about 25 meV per water molecule, which is around the thermal energy at room temperature.

Figure 5.6 also shows the pressure effect on these 22 proton-ordered structures. Their relative enthalpies with respect to the structure having the lowest enthalpy were plotted from P = 1 bar upto P = 20 kbar. The energetic sequence of the configurations does not change much as pressure increases. Configuration #1 still has the lowes enthalpy in this studied pressure range. At some pressures, some configurations swap the order sequences but does not change the overall step-wise shape.

$\mathbf{S}_\chi$

The novel host water network S_χ that was found to exist in several gas hydrate systems is extensively studied in this subsection. Originally, the C_0 hydrate was firstly discovered in the hydrogen hydrate system by Efimchenko et al [37] in 2011. Although the C_0 water network has been proposed by several researchers, its structure had been unresolved. In 2017, Amos et al. performed a neutron and x-ray diffraction in both CO_2 and H_2 hydrates and suggested a spiral proton-disordered water network with spacegroup $P6_522$ and called this helix water network as "S_χ" [3].

The S_χ framework has a unique structure, which cannot be classified as either "filled-ice" or a "traditional" clathrate. Its unit cell contains six water molecules

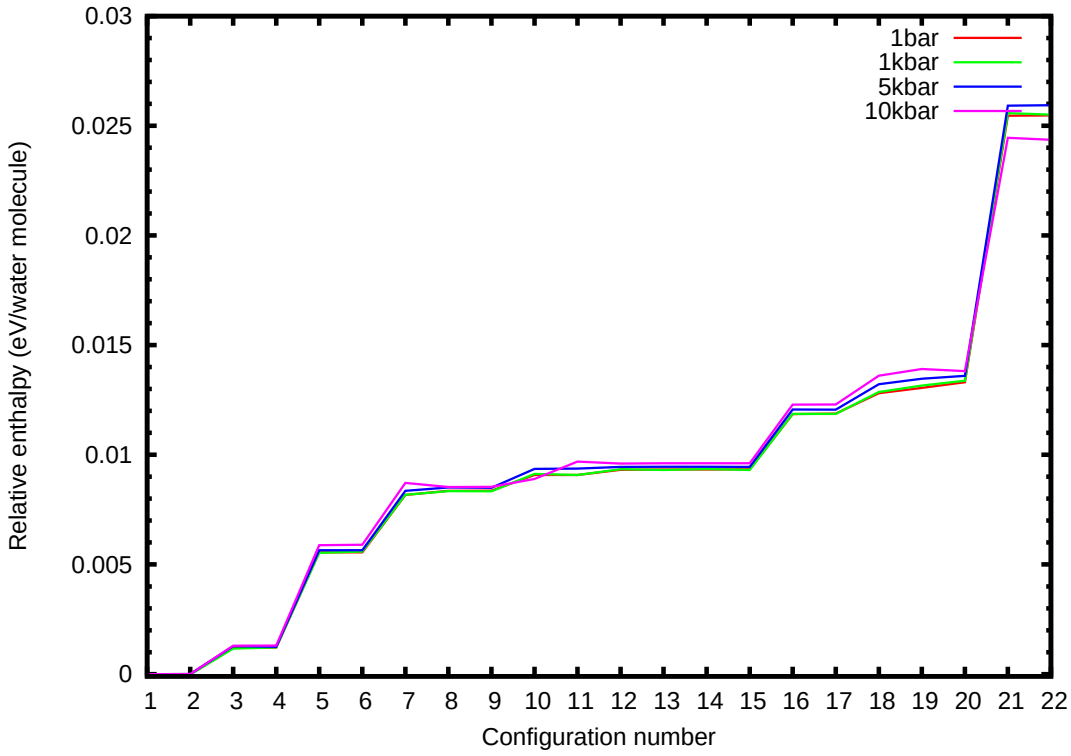

Figure 5.6 *Relative enthalpy plot of several proton-ordered ice-II phases with respect to the structure having the lowest enthalpy. Configuration #1 is the one found in nature. Calculations were performed using rPW86-vdW2 functional at various pressures.*

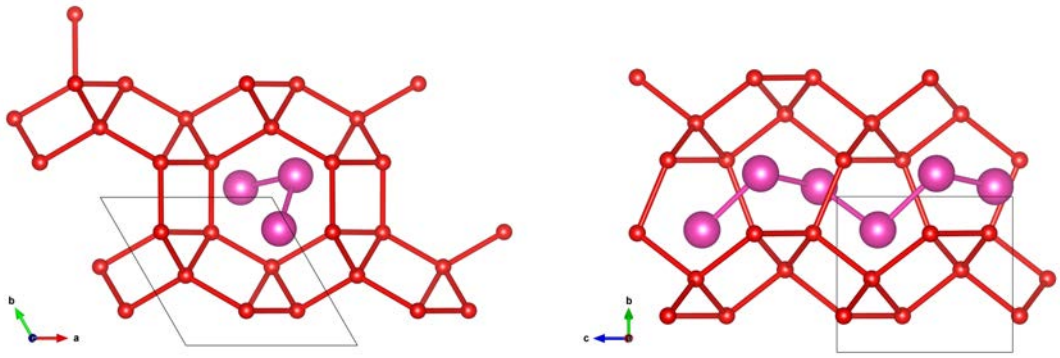

Figure 5.7 *Two views of the fully-filled S_χ hydrate, along (left) and perpendicular (right) to the channels in the S_χ network. Guest-Guest and O-O bonds are indicated. Three possible sites for the guest species are allowed in this network*

and has three sites for the guests, leading to a water:gas ratio of 2:1. The three guest sites are located within the spiral channal along the z-axis (see Figure 5.7).

In this subsection, several proton-ordered phases were computationally constructed based on the $P6_522$ unit cell. By using our graph-theory-based program to assign protons to experimentally known oxygen lattices, 12 distinct proton-ordered structures were generated. Their enthalpies obtained from full geometry optimisations based on the S_χ network were plotted as shown in Figure 5.8. Enthalpy calculations were performed using optB88-vdW functional from P = 1 bar to P = 20 kbar. Only selective pressures were shown in Figure 5.8 for clarity.

Of all the 12 structures (4 crystallographic symmetries), the configuration #1 with $P3_2$ symmetry has the lowest enthalpy at all our studied pressures (from P = 1 bar to P = 20 kbar). At elevated pressure, there are changes in the order sequences of some configurations, i.e. configurations #2 and #3 at P = 5 kbar and P = 10 kbar are swapping in the order sequences.

The energy spread between the structures having the lowest and highest energy is about 4 meV/H_2O molecule at P = 1 bar and slightly increases upon increasing pressure. The calculations of C_0 hydrates in the next chapters are based on the recently proposed proton-ordered S_χ network with $P3_2$ symmetry.

sI

Traditional clathrate structures are found to be host water structures for several gas hydrate systems. Three of the four known clathrate structures were studied

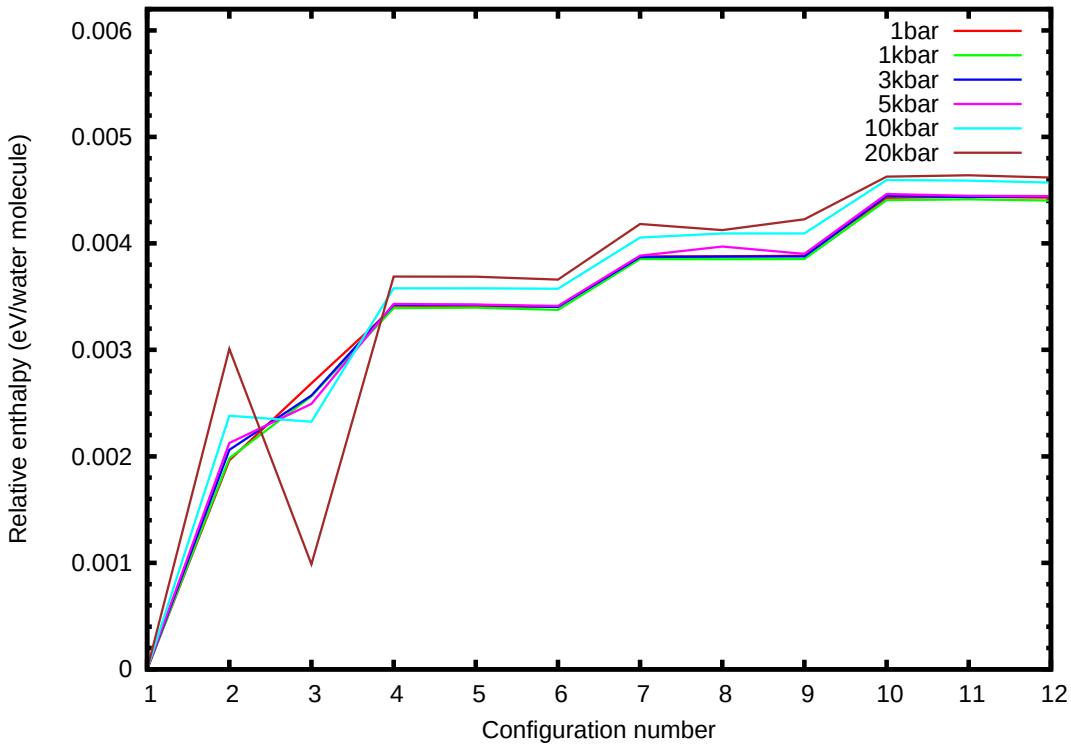

Figure 5.8 *Relative enthalpy plot of several proton-ordered S_χ phases with respect to the structure having the lowest enthalpy ($P3_2$ symmetry, configuration #1). Calculations were performed using rPW86-vdW2 functional.*

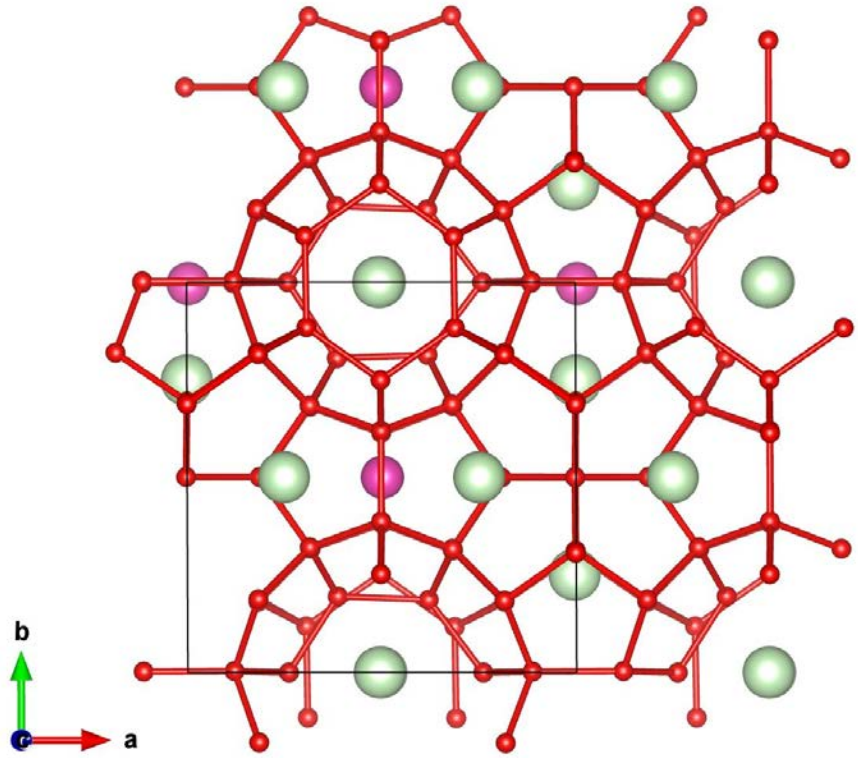

Figure 5.9 *Picture of the sI clathrate. O-O bonds are indicated. Eight possible sites for the guest species are allowed in this network: two in small cages (purple), six in large cages (green).*

in this section, namely sI, sII, and sT. The sH is omitted in this research due to its huge unit cell leading to a computational limitation. The goal is to obtain an idea on the energetic spread of pure clathrate structures so that we can estimate computational errors in the future. Thus, proton-ordered structures based on these three clathrates were produced. Additionally, there is still limited experimental information on the protons' positions on all the clathrates mentioned above, usually because of their partially occupancies. Thus, constructing proton-ordered structures is useful for computational works.

Figure 5.9 represents the sI network in a cubic unit cell (a = 12.1 Å). This sI clathrate contains 46 water molecules/ unit cell. Eight possible guest sites are allowed in this structure. Two sites are located within small cages (shown as purple points) and six are at large cages (green points).

For the clathrate structure I (sI), 4 proton-ordered structures were generated by our using graph-theory-base program, which the oxygen lattice has $Pm\bar{3}n$ symmetry. While placing hydrogens in particular sites lowers the symmetry

significantly, in this case, all structures have space group P1.

Enthalpy calculations were performed using optPBE-vdW functional at P = 1 bar and listed in Table 5.3. Results demonstrate that the enthalpy difference is quite small (< 2 meV/H_2O molecule). However, this conclusion is based only on 4 candidate structures. Since there are several million ways of arranging protons to the sI clathrate structure, there might be larger enthalpy spread among the configurations.

Nevertheless, we select the structure having the lowest enthalpy (structure #2) to be the host water structure for our gas-hydrate structure in the latter work in this thesis.

Structure	Enthalpy (eV/ water molecule)
1	-14.8728
2	-14.8741
3	-14.8725
4	-14.8729

Table 5.3: Proton-ordered phases generated using the oxygen host water lattice of sI clathrate and their enthalpies per water molecule.

sII

Traditional clathrate structure II (sII) is the largest structure we assign protons into. Its oxygen lattice has $Fd\bar{3}m$ symmetry with a cubic lattice vector of 17.3 Å. Calculations based on this sII also requires huge amount of computational resources in order to obtain their enthalpy information. Thus, we assigned proton positions to sII clathrate in both a conventional unit cell (136 H_2O molecules/ unit cell) and a primitive unit cell (34 H_2O molecules/ unit cell) in order to test their enthalpy differerence. 4 distinct proton-ordered structures (with P1 symmetries) in a conventional unit cell and a proton-ordered structure in a primitive unit cell (with Cc symmetry) were constructed. Their enthalpies were demonstrated in Table 5.4. Calculations were performed at optPBE-vdW level of theory at P = 1 bar.

According to Table 5.4, the energetic spread among those 5 configurations are very small (< 0.5 meV/ water molecule). Moreover, the enthalpy results between

both the conventional and primitive unit cell are similar. This suggests one can use the primitive unit cell for the furthur studies to save computational cost. Again, we admit that our conclusion was based only on small samplings. Wider energetic spread might be found if taking more configurations into account.

Structure	Enthalpy (eV/ water molecule)
P1 (136 H_2O/ per unit cell)	
1	-14.8753
2	-14.8755
3	-14.8758
4	-14.8753
Cc (34 H_2O/ unit cell)	
1	-14.8754

Table 5.4: Proton-ordered phases generated using the oxygen host water lattice of sII clathrate and their enthalpies per water molecule.

Figure 5.10 shows the sII network, with Cc symmetry so that there are 34 H_2O molecules per unit cell. Twelve possible guest sites are allowed in this structure. Eight sites are located within small cages (shown as purple points) and are at large cages (green points).

sT

A fully-filled sT hydrate is demonstrated in Figure 5.11 in a tetragonal unit cell, (a = b = 6.14 Å, c = 10.84 Å; $\alpha = \beta = \gamma = 90°$). Two viewed along b-axis (left) and c-axis (right) are presented. There are 12 water molecules per unit cell. Four possible sites for the guest species are allowed (shown as purple dots) in this network.

The tetragonal clathrate structure (sT) is found in only few gas hydrate systems. However, one of the experimentally known hydrates based on sT structure is argon hydrates at P = 0.6 - 1.1 GPa. In addition, experimental results provide only partial occupancy information based on this sT structure. Therefore, we performed a test on different proton-ordered configurations by using known host oxygen lattices based on sT hydrates.

A program based on graph-invariant topology proposed by Singer's research

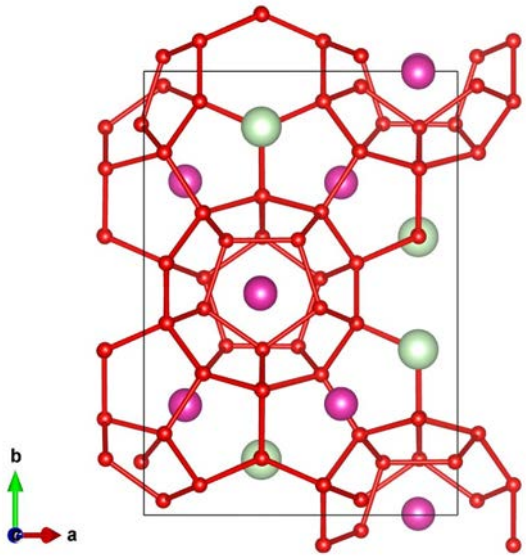

Figure 5.10 *Picture of the sII network, with Cc symmetry, along c axis. O-O bonds are indicated. Twelve possible sites for the guest species are allowed in this network: eight in small cages (purple), four in large cages (green).*

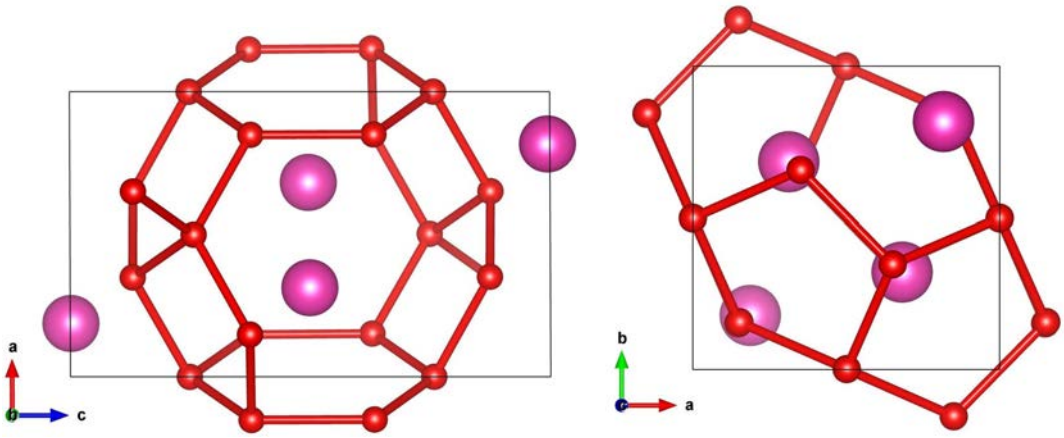

Figure 5.11 *Two views of the fully-filled sT hydrate, along b-axis (left) and along c-axis (right) in the sT network. O-O bonds are indicated. Four possible sites for the guest species are allowed in this network as shown.*

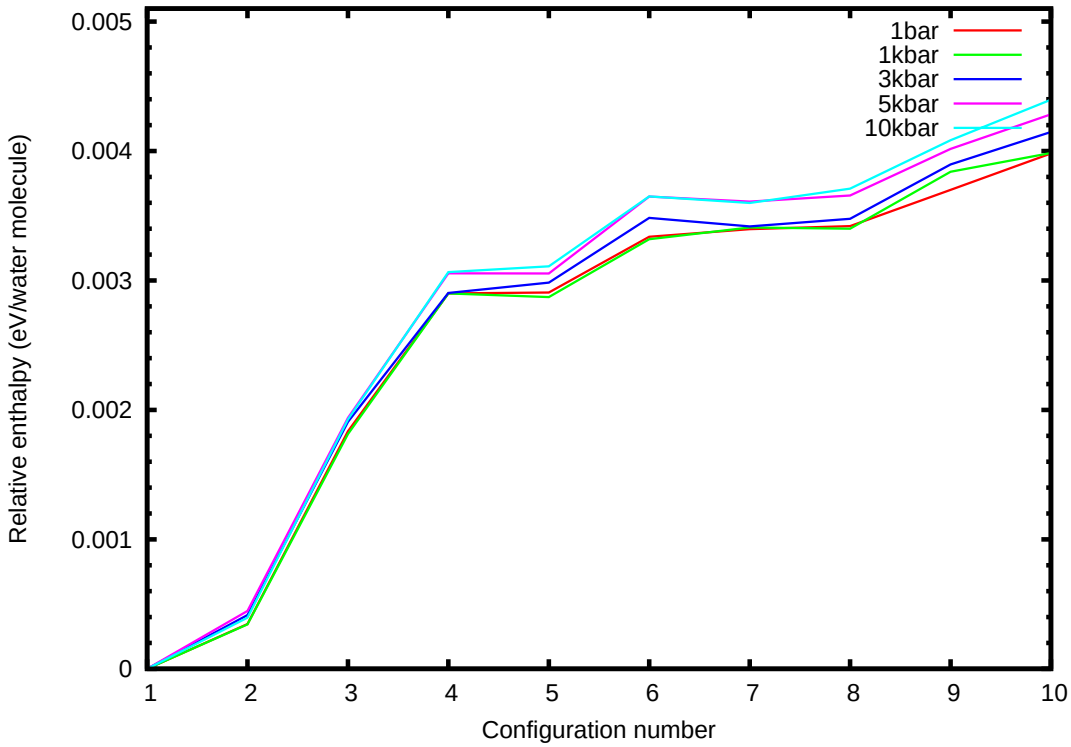

Figure 5.12 *Relative enthalpy plot of several proton-ordered sT phases with respect to the structure having the lowest enthalpy. Calculations were performed using rPW86-vdW2 level of theory.*

group is used in order to generate protons in this subsection. 10 proton-ordered structures were selected as a representative out of 52 distinct configurations generated by such program. Their enthalpies were plotted and illustrated in Figure 5.12.

According to Figure 5.12, configuration #1 has the lowest enthalpy and the order sequence of all 10 configurations arranging by their relative enthalpies (from low to high) is approximately the same, althouth there are some changes in the order sequence at certain pressures. However, this does not change the fact that the configuration #1 still has the lowest enthalpy under our studied pressure range (P = 1 bar to P = 10 kbar).

The enthalpy spread between the structures having the lowest and highest enthalpy is about 4 meV/ water molecule and slightly increase as elevated pressure.

5.4 Discussion

According to the enthalpy results obtained from assigning proton positions to pure water networks, the enthalpy spreads among all different water networks are small. For both sT and S_χ structures the enthalpy spread is about 4 meV per water molecule, traditional clathrate structutre I and II is in a much relatively smaller spread ($<$ 2 meV per water molecule and 0.5 meV per water molecule, respectively). This suggests only small contribution from different arrangements of hydrogens and has already been confirmed by other theoretical works [69]

Moreover, the enthalpic spread between the structures having the lowest and highest enthalpies slightly increases upon increasing pressure.

Although the enthalpy spread based on ice-II structure is larger (about 25 meV/H_2O molecule), this might be the reason on why it is the only ice phases having proton-ordered structure.

Chapter 6

Noble Gas Hydrates

This chapter focuses on noble gas-water compounds, where the noble gases are He, Ne, and Ar. Hydrates formed by these inert gases are commonly found in nature because their small sizes are suitable to be accommodated in the empty space formed by ice networks [106]. Additionally, weak interaction between noble gases, and between noble gases and the surrounding water molecules help stablize the hydrate compounds [41]. These compounds also serve as model systems for more complex di-atomic molecular gases (discussed in Chapter Seven). The main reasons for studying these gases are they share almost the same size similarities, both have the spherical symmetric properties. In spite of their simple structures, there is not much research on the noble gas hydrates compared to the other gas hydrates, e.g. hydrogen, methane, or other small molecules [106].

Thus, this chapter will emphasize on computational work on the noble gas hydrate systems. Some host water networks found by both theoretical predictions and experiments in the hydrogen hydrate system are implemented as the host water structures for the noble gases in this work. Most results in this chapter has already been published by us in the Journal of Chemical Physics, **143**, 154407 (2015).

6.1 Currently known noble gas hydrate phases

Experimentally known phase diagrams of helium hydrate (blue dots) and neon hydrate (red dots) based on ice-I_h and ice-II are shown in Figure 6.1. The

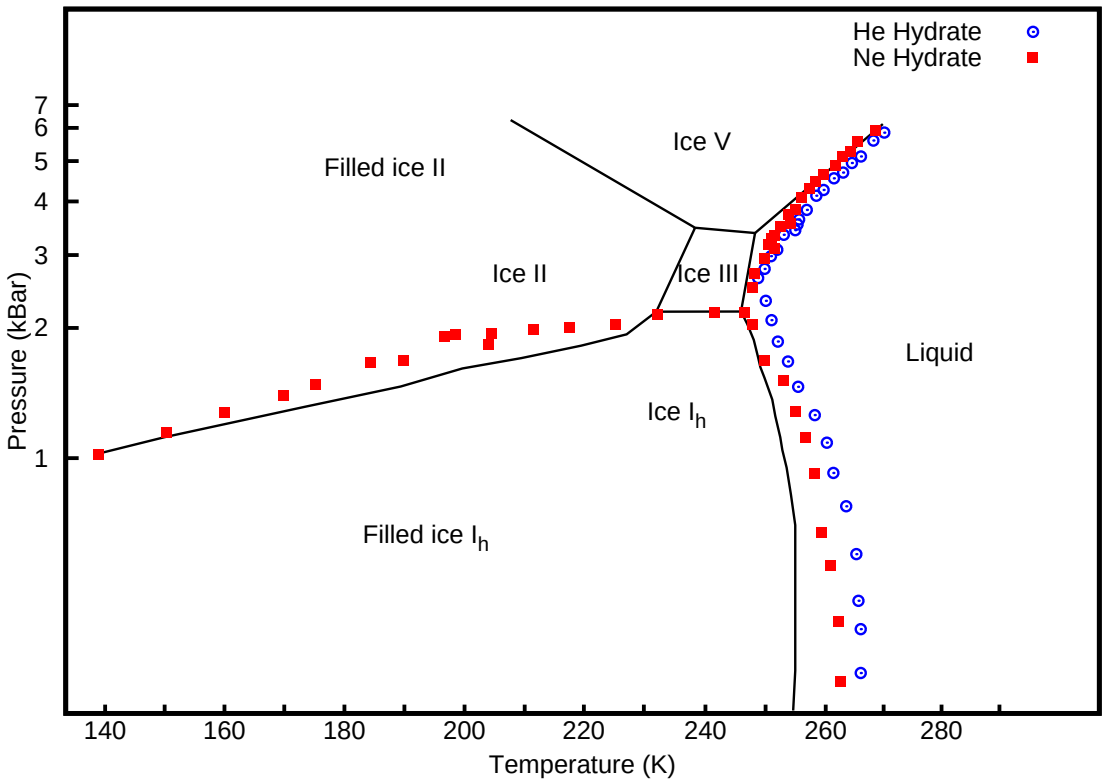

Figure 6.1 *Phase diagram of helium hydrate and neon hydrate based on ice-I_h and ice-II [32]. Solid lines indicate phase boundaries of pure ice phases. Dots represent the phase boundaries of hydrates.*

hydrates' phase boundaries were measured by using differential thermal analysis (DTA) by Dyadin *et al.* [32]. Solid lines illustrate the phase boundaries of pure ice. Both helium and neon hydrates adopt the ice structures based on ice-I_h and ice-II. Known phases by both experiments and theoretical predictions are summarised in this section.

6.1.1 Helium Hydrates

In the helium hydrate system, the only well characterised helium hydrate is based on the filled ice-II structure, and found at pressures between 0.28 - 0.48 GPa [104, 105] and further been refined by Lobban et al. [102]. The water:helium ratio is 6:1 at full occupancy (i.e., one He per cavity). By using differential thermal analysis (DTA) to explore the dissociation curve of the helium hydrate up to 1.5 GPa, Dyadin *et al.* [32] discovered thermal anomalies in the 0.1-0.2 GPa range, suggesting the presence of a different phase at lower pressure. Based on their interpretation, a classical clathrate was suggested (see Figure 6.1). This

discovery also implied the possibility of finding helium-water compounds in other host water networks. Although there is evidence of helium base on ice-I_h structure at P $<$ 0.28 GPa [102], none of the research has experimentally proposed the crystal structure based on ice-I_h. In 2014, Belosludov et al. [12] performed a theoretical calculation based on an extended van der Waals-Paltteeuw approach [11] to construct the phase diagram of helium hydrates based on ice-I_h and ice-II and help completing the phase diagram previously proposed by Dyadin [32].

There are limited diffraction studies on this helium hydrate system at pressure above 0.5 GPa [106], which restrict the information on structural data at higher pressure. Several theoretical studies using both MD simulations and statistical mechanics have been conducted in order to predict hydrate phases and obtain their crystal structures instead [10]. By using classical lattice dynamics with SPC potential between water molecules and standard 6-12 Lennard-Jones potential between the helium atoms, the estimated stability region of helium hydrates based on ice-I_c was predicted to be at P = 0.42-0.5 GPa [10].

In summary, three phases based on ice-II, ice-I_h and ice-I_c are proposed in the helium hydrate system. Only the phase based on ice-II network is fully structural resolved at P = 0.28-0.48 GPa. Although there is some evidence showing the phase based on ice-I_h in this system at P $<$ 0.28 GPa, none of the experiments has been able to find the crystal structure based on this ice-I_h. Theoretical work also proposed the adoption of ice-I_c host water networks in the helium hydrates at higher pressure (P = 0.42-0.5 GPa).

Since helium and hydrogen have sizes comparable to each other, helium might be able to adopt the same host water networks found in the hydrogen hydrates system. Therefore, in addition to the currently known hydrogen hydrates' host water networks, the novel host water network S_χ is also considered in the helium hydrate system here. In summary, five different phases of host water structures, namely S_χ, ice-II, ice-I_h and ice-I_c, are implemented in all noble gas hydrate studies.

6.1.2 Neon Hydrates

Similar to helium, neon hydrates were recently found to adopt ice-II host water network (water:neon ratio of 6:1) at 0.48 GPa and 70-260 K by in situ neutron diffraction [176]. Molecular dynamics studies confirmed the neutron diffraction

result at 0.48 GPa and 260 K. These findings agree well with the results from DTA measurements by Dyadin et al. [32] suggesting that neon forms a clathrate structure based on ice-II network between 0.2-0.3 GPa. The DTA study by Dyadin et al. (depicted in Figure 6.1) also suggested the formation of neon hydrates based on ice-I_h structure (water:neon ratio = 2:1). However, only the crystal structure of ice-II hydrate has been resolved.

There is also a theoretical work suggesting a new host water network, which is based on ice-I_c structure in this system. In 2010, Hakim et al suggested a new theoretical predicted ice-I_c host water network using a hybrid type of grand-canonical (GC) and isothermal-isobaric (NPT) Monte Carlo (MC) simulation [53]. The ice-I_c was predicted to be stable at 0.3-1.8 GPa, T = 210 K. They also found that the number of neon guest atoms increases as pressure elevates with the maximum water:neon ratio of 1:1.

In 2014, Bozhko et al. performed a statistical simulation to study the phase transition of neon hydrates based on ice-I_h and ice-II structures [18]. This study helps constructing a complete P-T diagram and also confirming the results retreived from the DTA measurement by Dyadin et al [32].

In summary, three host water networks are proposed by both experiments and computations in the neon hydrate system, namely ice-II, ice-I_h, and ice-I_c. However, these three gases i.e. helium, neon and hydrogen are of a similar size. This implies a possibility of the existence of adopting some other phases already found in those hydrate systems. In this work, the same five host water phases used in the helium hydrate system are analyzed;.

6.1.3 Argon Hydrates

Three phases of argon hydrate are known to exist. At low pressure, argon forms a clathrate structure (ArH-I) based on sII (with water:argon ratio = 4-4.5:1). Neutron powder diffraction [108] experiments demonstrated that ArH-I transforms to ArH-II, which adopts the sH structure, at 0.46 GPa (water:argon ratio of 3.4:1). Then, at 0.77 GPa, ArH-II transforms to ArH-III, which adopts the sT framework (water:argon ratio of 3:1) [108]. Hirai *et al.* [67, 68] performed X-ray diffraction measurements and suggested a new phase at 1.1 GPa that is based on MH-III; this is refered to as "filled-ice" structures. Although experimental studies indicate that argon does not adopt any of the filled-ice structures [68, 107],

the same set of host water networks used in both the helium- and neon hydrates is still implemented in the argon hydrate system. Thus, we can compare the quantitative measurement as to how unstable the argon hydrates to their base line decompositions (pure water ices and solid argon). Consequently, we may establish the role of different guest sizes for stabilization of the hydrates.

6.2 Methodology

Structural relaxations were performed by using density functional theory (DFT) [71, 91] and the projector augmented wave (PAW) method [17, 94] to describe the electron-ion interaction, as implemented in the VASP code, version 5.3.3 [93]. The plane wave cutoff energy ($E_c = 875$ eV) and Monkhorst-Pack k-point meshes [114] (density 20/Å^{-1}) were considered to be large enough to fully converge total energies and forces. The "hard" PAW data sets, with atomic cutoff radii (H = 0.80 a_0, O = 1.10 a_0, He = 1.10 a_0, Ne = 1.70 a_0, Ar = 1.90 a_0) were used in the calculations. Structural relaxations were performed until the net forces were smaller than 2 meV/Å. Dispersion corrections of long-range electronic correlation effects were included in the structural relaxations along with the standard PBE functional to establish how they affected structures and stabilities of various phases. Two dispersion methods were used in this study, the semi-empirical PBE+D2 [50] and the electron density-based vdW-DF approach [27]. PBE+D2 is a correction to the total energy based on a pair-wise atomic interaction potential using tabulated parameters. The first vdW-DF functional proposed by Dion *et al.* is a non-local dispersion functional dependent on the electron density. There are several varieties of the vdW-DF functionals. Here, only two vdW-DF functionals are tested, namely optPBE-vdW [84] and the second version of vdW-DF proposed by Lee *et al.* [100] that uses rPW86 functional for the exchange energy (rPW86-vdW2).

6.3 Dispersion Effects

6.3.1 Noble Gas-Water Dimers

Long range dispersion interactions, such as van der Waals (vdW) forces, are crucial to approximately predict correct lattice energies and phase transition pressures between different molecular ice phases [136, 137]. This has been seen, for instance, by accurate calculations of electron correlation energies in solid ice [62]. This research considers the results from four different exchange-correlation functionals: rPW86-vdW2, optPBE-vdW, PBE+D2, and PBE. Amongst these, the non-local density-based rPW86-vdW2 functional is assumed to provide the most accurate results. This was concluded from the work by Santra *et al.* on the importance of dispersion corrections for ice, comparing a series of vdW correction methods [137]. While water ice is now seemingly well understood, it is less clear which dispersion correction method would be most suitable to describe the inclusion compounds of the type of hydrates studied here. This is presumably due to the nature of the weak interaction between host and guest, dispersion interactions will make a quantitative difference with regards to phase stabilities and transition pressures. However, since water is a polar molecule, the leading interaction is of a nature permanent dipole-induced dipole. Much of this essentially electrostatic interactions should be already included in semi-local exchange-correlation functionals. Thus, the comparison among different functionals (density-based rPW86-vdW2 method, the semi-empirical PBE+D2 and the semi-local PBE functionals) should provide an insight on the dispersion interaction in these gas hydrate systems.

A simple test on the influence of the dispersion energies with different computational methods was done on the noble gas-water dimer systems. The study of these noble gas-water dimer models supplies insightful information on the amount of dispersion interactions provided by different methods. The potential energy surface of a He-H_2O dimer, but with different orientations of the water molecule was tested. Five configurations of a water molecule (as shown in the inset of Figure. 6.2) were used to calculate the water-He interaction energies via both wavefunction-based methods (MP2, CCSD, CCSD(T)) and density functional theory approach (PBE, PBE+D2, optPBE-vdW, rPW86-vdW2). DFT results using VASP are compared to results from second-order Møller-Plesset perturbation theory (MP2) and coupled-cluster calculations (at the CCSD(T)

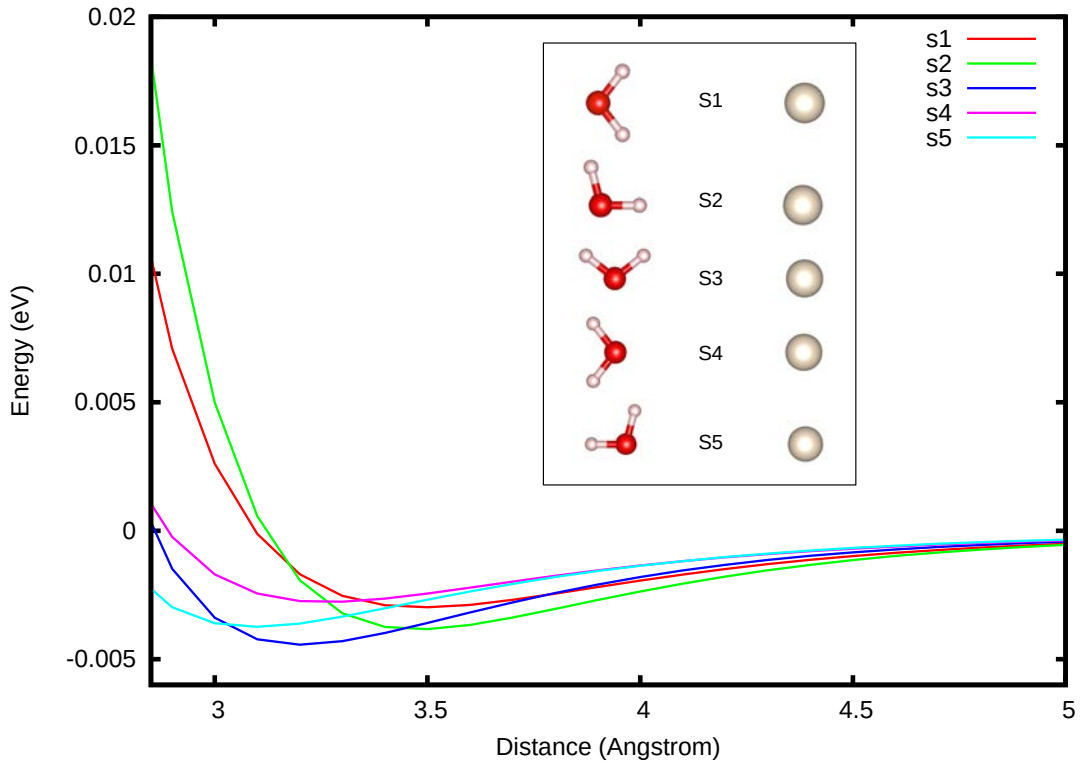

Figure 6.2 *He-H_2O CCSD(T) interaction energies as a function of He-O distance, for five different water configurations (shown in the inset, listed as S1 to S5). Of those five water configurations, the structure S5 was chosen to represent the water-guest orientation in the hydrate compounds.*

level) using Gaussian [45], where the latter will provide the most accurate estimate of the actual interaction energy. Augmented quadruple-zeta correlation consistent basis sets were used in those calculations [154, 173].

According to the five configurations shown in the inset of Figure 6.2, the S5 configuration is assumed to be the best candidate structure to naturally describe the water networks surrounded the guest gas species. The reason is due to limited choices of protons' directions as governed by the Bernal-Fowler rules, which form hydrogen bonded networks to the neighbouring water molecules.Therefore, the S5 water configuration was chosen to represent the water-guest interaction energies in further calculations in this work. An example of the noble gas-water interactions based on different water configurations (S1 to S5) calculated by the CCSD(T) method is listed in Table 6.1.

The results of the He-H_2O interaction from different computational methods are shown in Figure 6.3 and listed in Table 6.2. It is clear that all DFT methods

Noble Gas	S1	S2	S3	S4	S5
He	(3.50, -2.98)	(3.50, -3.83)	(3.20, -4.43)	(3.30, -2.76)	(3.10, -3.74)
Ne	(3.40, -8.64)	(3.40, -11.14)	(3.20, -11.62)	(3.20, -7.24)	(3.10, -9.07)
Ar	(3.70, -16.30)	(3.70, -20.20)	(3.50, -19.61)	(3.50, -14.79)	(3.40, -17.04)

Table 6.1 *Noble gas-water interactions based on different water configurations labled by S1 to S5. Results are calculated by CCSD(T). For each noble gas, equilibrium distance d_{O-NG} in Å and binding energy E_0 in meV are given.*

Methods	He	Ne	Ar
MP2	(3.16, -2.88)	(3.18, -7.34)	(3.36, -17.28)
CCSD	(3.11, -3.10)	(3.15, -7.39)	(3.49, -13.11)
CCSD(T)	(3.10, -3.74)	(3.09, -9.01)	(3.37, -16.83)
PBE	(3.06, -5.38)	(3.21, -7.15)	(3.64, -8.65)
PBE+D2	(2.90, -9.54)	(3.02, -16.31)	(3.37, -21.18)
optPBE-vdW	(3.03, -14.39)	(3.13, -22.38)	(3.48, -31.03)
rPW86-vdW2	(2.99, -7.99)	(3.06, -14.28)	(3.38, -23.62)

Table 6.2 *Noble gas-water interactions from various methods. The interaction results of each noble gas and the water configuration S5 are listed in the brackets (equilibrium distance d_{O-NG} in Å , binding energy E_0 in meV).*

overestimate the interaction considerably when compared to the CCSD(T) results. This is in agreement with other theoretical studies that find an overestimation of rare gas dimer binding energies using (semi-)local exchange-correlation functionals [115]. This is an issue which gets aggravated with additional explicit inclusion of long-range attractive interactions. While the PBE binding energy (amongst the small set of DFT methods used here) deviates least from the CCSD(T) result, the rPW86-vdW2 functional produces an equilibrium separation d_{O-He} that is closest to the CCSD(T) result. The PBE+D2 method, as well as significantly overbinding, also produces the by far smallest equilibrium separation d_{O-He}. None of the DFT methods are therefore perfect to describe the noble gas hydrate compounds. However, in order to correctly describe the pressure-induced phase sequence of their main constituent, water, the rPW86-vdW2 results are the most accurate. Hence, these calculated results will be referred to this functional unless otherwise specified. As d_{O-He} is obtained most accurately with this functional, it is expected to give the most accurate geometries of the hydrates, while the severe overbinding could mean an artificial stabilisation of hydrate phases compared to the elemental constituents.

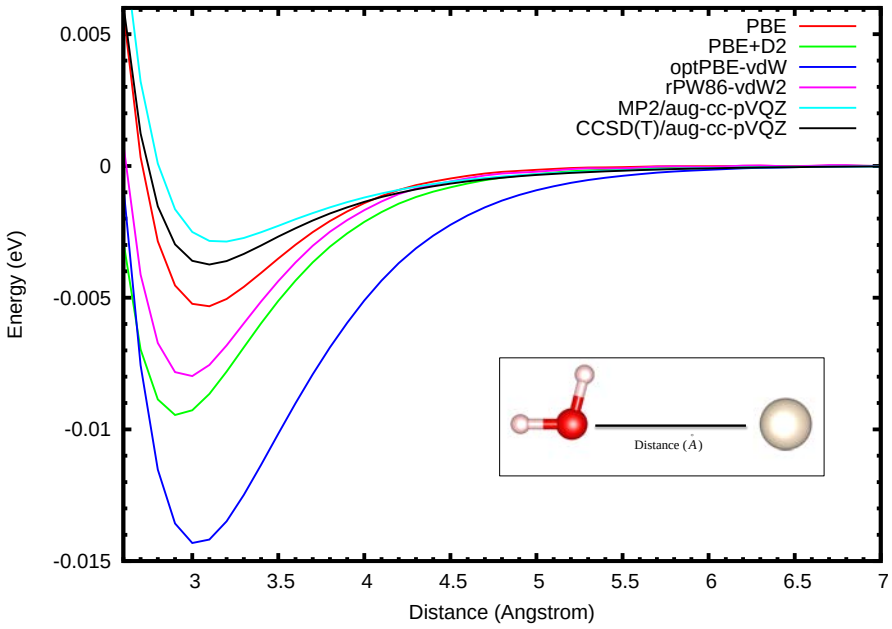

Figure 6.3 *Potential energy surface of the He-H_2O interaction (geometry shown in inset), comparing various density- and wave function-based approaches, as function of the He-O separation.*

Methods	rPW86-vdW2 geometry of He	optimized geometies
MP2	-22.14	-
PBE	3.88	42.34
PBE+D2	-13.94	-12.04
optPBE-vdW	6.60	-58.29
rPW86-vdW2	-24.91	-24.91

Table 6.3 *Relative formation energy (in meV/cluster) of a cluster containing a helium atom and 12 water molecules from various methods, both wavefunction-based method (MP2) and density functional methods (PBE, PBE+D2, optPBE-vdW and rPW86-vdW2).*

6.3.2 Noble Gas-Water Clusters

Up to date, we cannot calculate the dispersion energy in a solid system using a "gold standard" quantum chemistry approach CCSD(T) due to its computational demanding. The largest system we can compute using the CCSD(T) method is a cluster system. Therefore, noble gas-water clusters are studied in this subsection. In an attempt to establish the influence of dispersion effects in solid states caused by different computational methods, we examine the interactions of noble gas-water clusters and compare the results to the helium-water dimer's calculations. The investigation on how much of the deviation between the helium-water dimer and cluster will provide an general idea on the dispersion effects produced by different methods in expanded systems.

Shown in Figure 6.4 is a cluster consisting of a helium atom and its twelve closest neighbours of water molecules, this He-$(H_2O)_{12}$ cluster was taken from a relaxed structure of helium hydrate based on ice-II host water network using rPW86-vdW2 functional at 1 bar. Calculations were performed by using both quantum chemistry (MP2) with aug-cc-pVQZ basis set by Gaussian program and density functional approaches (PBE, PBE+D2, optPBE-vdW and rPW86-vdW2) by VASP software. The summation of the relative formation energies of the helium-water cluster obtained by various methods is listed in Table 6.3. According to Table 6.3, there are significant deviations in the relative formation energy of the cluster among different methods. The MP2, PBE+D2 and rPW86-vdW2 indicate the stability of the cluster; whereas the PBE and optPBE-vdW suggest unstability.

To test this cluster interaction further, alternative approaches using wavefunction-based correlation methods via the method of increments and the local MP2

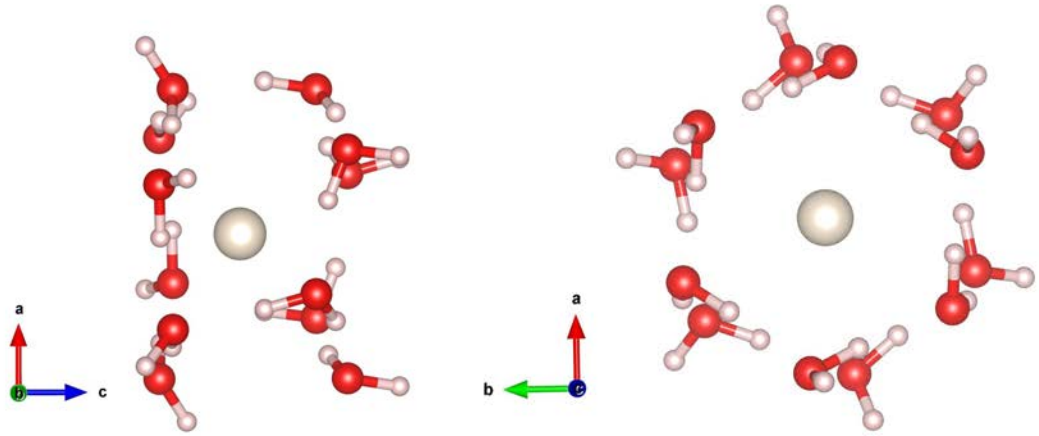

Figure 6.4 *Cluster model of a helium atom and its twelve closest neighbours of water molecules. The He-$(H_2O)_{12}$ cluster was taken from a relaxed structure of helium hydrate based on ice-II host water network using rPW86-vdW2 functional at 1 bar.*

method [116] are collaborately performed by a research group leaded by Prof. Beate Paulus at Freie University in Berlin (Paulus' group).

In the method of increment, the correlation energy is expanded in the following

$$E_{corr} = e_g + \sum_i e_i + \sum_i \Delta e_{gi} + \sum_{i>j} \Delta e_{ij} + \sum_{i>j} \Delta e_{gij} + ...$$

In the above equation, the first and second term, e_g and e_i, represents the correlation energy of the guest and the individual water molecules of the cluster, respectively. The third term, $\Delta e_{gi} = e_{gi} - e_g - e_i$, is a two-body increment between the guest and individual water molecules. The forth term, Δe_{ij}, is a two-body increment of two water molecules of the cluster. The last term, $\Delta e_{gij} = e_{gij} - \Delta e_{gi} - \Delta e_{gj} - \Delta e_{ij} - e_g - e_i - e_j$, corresponds to a three-body increment of the guest and two water molecules of the cluster.

In principle, higher order terms (e.g. four-body term and so on) can also be included. However, the two-body terms are expected to provide the major contribution of the binding interaction and little contributions from those higher order terms [117]. Thus, the method of increment are often truncated at the three-body terms between the guest and two water molecules [7].

The binding energies were calculated by taking the difference of the energy of the

combined system (a noble gas atom encapsulated by $(H_2O)_{12}$ cluster) and the energy of the empty cluster and the guest atom. The latter two energies were calculated by applying counterpoise correction in order to take care of the basis set superposition error (BSSE). The total binding energy was divided into three parts: (1) E_{HF}, which was calculated for the full system, (2) E_{MP2}, evaluated in both the full system and with the method of increments (MI) to validate the limit the incremental expansion, (3) $E_{CCSD(T)}$, which was computed by using MI.

According to the results listed in Table 6.4, the interaction is repulsive at the HF level and the HF binding energy increases as the noble gas' size increases (from He to Ar). This reflects the larger spatial extent of the guest atoms. When including the correlation effect at the MP2 level to the HF (HF+MP2), the binding energies are greatly reduced, although still repulsive. For the most accurate method (HF+MP2+incLCCSD(T)), the binding energies of the noble gases are trivially attractive for neon, though still slightly repulsive for helium. For argon, repulsive binding energy is found. Such a result is not surprising for large guest atoms to be unstable if fitted in small space.

Comparing the results between DFT (rPW86-vdW2) in Table 6.3 and HF+MP2+ incLCCSD(T) in Table 6.4, it is clear that the rPW86-vdW2 has a significant greater overbinding effect than the HF+MP2+incLCCSD(T) by about 24 meV/cluster. Nevertheless, if comparing the binding energies from the cluster and the dimer (in the previous subsection) between DFT (rPW86-vdW2) and quantum chemistry approach (MP2), the result from the cluster indicated significant reduction in the overbinding energy compared to the dimer's. This implied that the overbinding effect might be less in the solid state phases than the decomposed systems.

Although, the sophisticated method (i.e. HF+MP2+incLCCSD(T)) has been conducted, it is still not possible to draw a firm conclusion for the binding energy in the solid phase whether the gas-water compound is stable or not. Howerver, as this calculation considers only 12 water cluster, further cluster expansion imitating a real crystal structure is still required.

Methods	He	Ne	Ar
HF	64	143	813
HF+MP2	7	20	253
HF+MP2+incLCCSD(T)	1	-2	288

Table 6.4 *Embedding Method used in Paulus's work [7] to calculate the binding energy of different guest gases on a cluster of twelve water molecule (geometry shown in Figure 6.4 , unit is in meV.*

6.4 Hydrate results

6.4.1 He-H_2O compound system

This chapter explores possible phases in the He-H_2O system by using ground state total energy calculations. As mentioned above, due to the similarity in size of He and H_2, the known phases of the H_2-H_2O system (with H_2 molecules replaced by He atoms) were used here, in addition to the currently known He hydrate structures, filled ice-II, ice-I_h and ice-I_c.

At each host water network, the energetic dependence upon varying the guest contents was tested (changing the stoichiometry of the compound). For example, ice-II contains 6 cages per hexagon unit cell being able to encapsulate the guest species. If all the cages have one guest atom/molecule per cage, this is called "fully-filled". In the case of the number of the guest species being more than the total number of the cages (to satisfy this, there must be more than one atom/molecule per cages), this is called "overly-filled". On the contrary, if the total number of the guest species is less than the number of the hosts' empty cages, this is called " partially-filled". Since there are varieties of combinatoric ways to assign the guests into the host sites, some samples are chosen to represent the whole possibilities to observe their energetic trends.

In order to compare the enthalpies of the compounds having different stoichiometries, a convex hull at each pressure is constructed. The convex hull (as mentioned in Chapter 4) is an intuitive method of comparing the calculated enthalpies of the compounds The convex hull is constructed by connecting a polygon enveloping all the points having negative formation enthalpies. Points on the convex hull are stable phases at that pressure. Points above the convex hull imply metastablilities; whereas points above the baseline indicate unstable

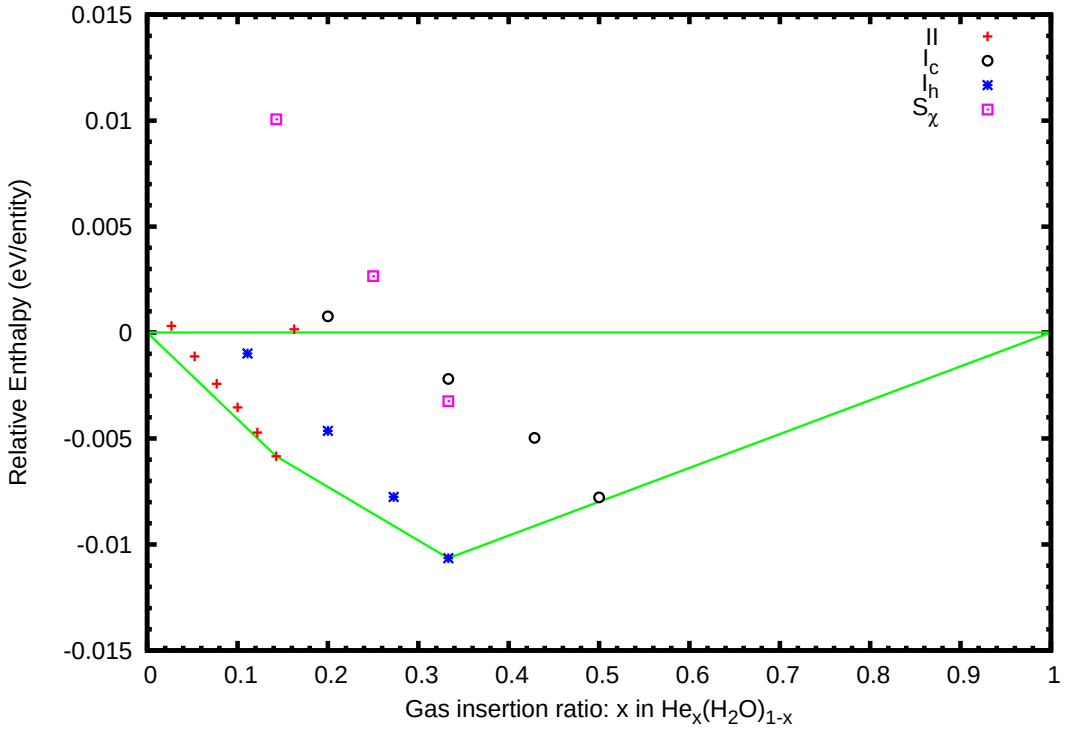

Figure 6.5 *Relative ground state enthalpies of formation for He-H_2O phases at P = 1 kbar, on the rPW86-vdW2 level of theory.*

phases compared to the constituents, ice and solid He.

According to the convex hull plot at P = 1 kbar (Figure 6.5), the He-H_2O compounds adopt the host water networks based on ice-II and ice-I_h. Seen from the graph, the fully-filled hydrates (one guest per cavity) have lowest enthalpies compared to the partially-filled and overly-filled networks. This leads to an overall H_2O:He ratio of 6:1 in filled ice-II, and 2:1 in filled ice-I_h. Note that the relative enthalpy of fully-filled ice-II is more stable than the partially-filled ice-II. Indeed, the partially-filled phases (not all the cavities are occupied) are not far from the convex hull. This means that a variety of ice-II based hydrates with varying degree of He occupancy may be formed experimentally, depending only on the He reservoir (i.e., its chemical potential) and potential diffusion barriers for He through the ice-II network. Over-filled ice-II (having two He atoms in one cavity) results in a large increase in enthalpy (see single red symbol at $x_{He} = 0.167$ in Figure 6.5). In contrast, partially-filled ice-I_h structures are less favorable, and an enthalpic trend towards formation of fully-filled ice-I_h hydrate is evident in Figure 6.5.

The other water networks included in this study, S_χ and ice-I_c, did not form any

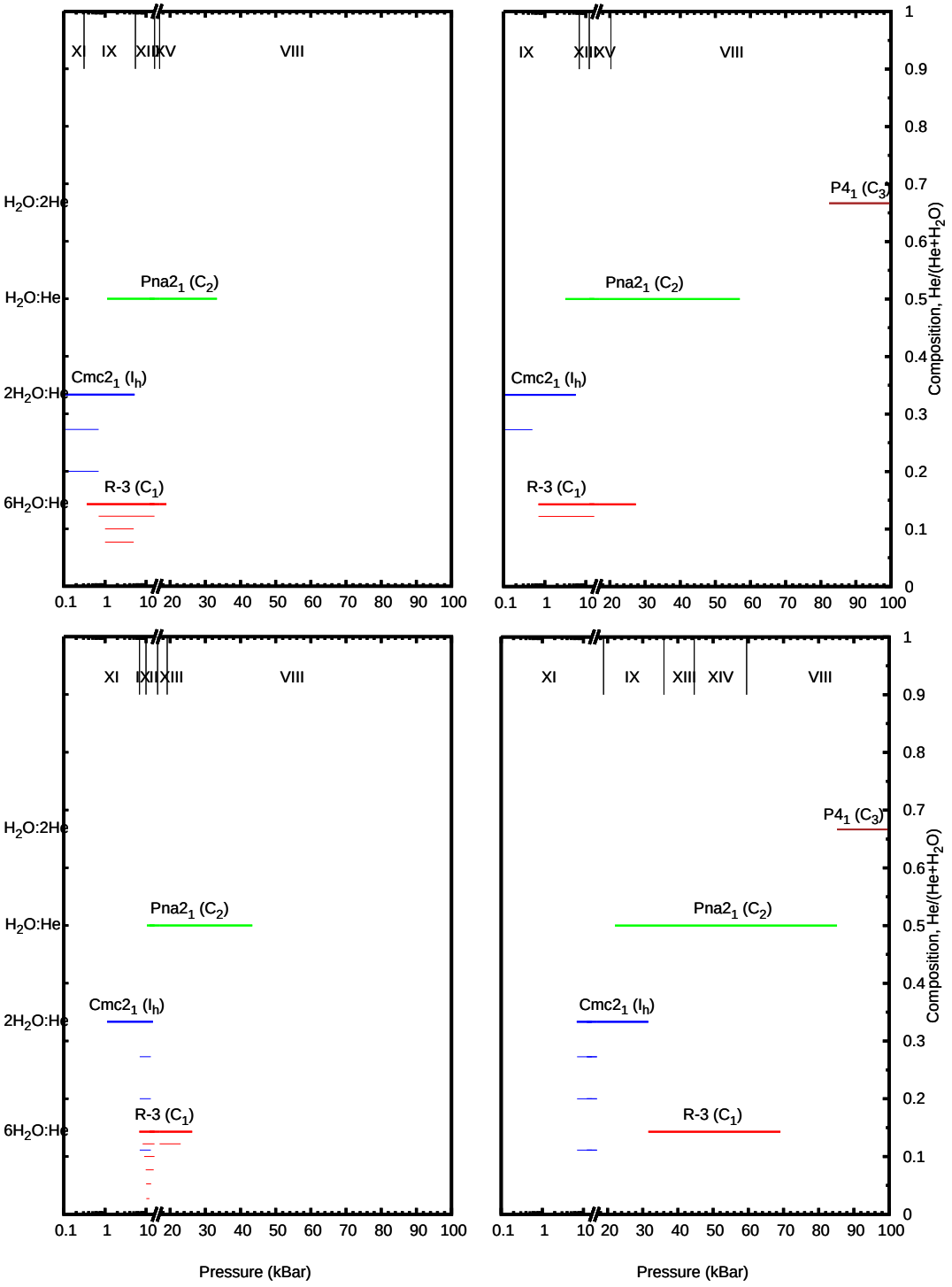

Figure 6.6 *Stability ranges as a function of pressure of the ground state phases in the He-H_2O system, using the rPW86-vdW2 (top left), optPBE-vdW (top right), PBE+D2 (bottom left), PBE (bottom right) functional. Information about the host spacegroups following by the notations of the host water networks, shown in brackets, are indicated above the stability ranges. Stability range of ice phases are also shown on the top of the graph.*

stable helium hydrates at this particular pressure. As can be seen in Figure 6.5, that a hydrate based on ice-I_c with H_2O:He=1:1 is not far off stability. Indeed, we find this phase to become stable at slightly higher pressures, at $P = 1.13$ kbar upto $P = 33.31$ kbar. In hydrogen hydrate terminology, this is the C_2 hydrate phase: one He atom occupies each cavity in the ice-I_c water network. The higher He content phase, which is also based on the ice-I_c water network with H_2O:He=1:2, remains unstable in our pressure range of consideration. This phase was calculated to be stable and was introduced as C_3 in the hydrogen hydrates [125]. Although both the C_2 and C_3 phases share the same ice-I_c water network, the difference between those two phases is that the He atoms are positioned either in the center of the cavities, or in the center of the six water rings that form the boundary of each cavity. Noting that the convex hull is the plot at only one specific pressure, to cover the entire range of studied pressure (upto 100 kbar), several convex hull plots are constructed. Finally, knowing which phases are stable at what pressure, the summary of all the convex hulls are plotted in Figure 6.6. Pressure is plotted in log-linear scale along the x-axis, whereas the composition ratios are listed along the y-axis. A sequence of stable host water networks also represent along the top of the graph. Each thick solid line in Figure 6.6 represents the pressure range where the respective phase is stable. The metastable phases are also included in the plot (shown as thinner solid lines), where metastability is defined as having ΔH_f less than 1 meV/entity above the convex hull. These phases include the partially-filled ice-II and ice-I_h networks.

Predicted stability ranges (in kbar) of the host water networks by using various functionals are listed in Table 6.5. According to Table 6.5, the S_χ host water network is not found to be stable in the He-H_2O system in all four functionals. The results also suggest that the predicted phase sequences upon increasing pressure are almost identical (ice-I_h $\rightarrow$ ice-II (C_1) $\rightarrow$ ice-I_c (C_2) $\rightarrow$ ice-I_c (C_3)). Although, at the studied pressure (upto 100 kbar), the C_3 phase is not found to be stable with both rPW86-vdW2 and PBE+D2 functionals. It might possibly become stable at higher pressure. The transition pressure ranges are different among the functionals used. E.g., rPW86-vdW2 suggests the helium-water compound based on ice-I_h is stable at $P = 1$ bar upto $P = 5.26$ kbar, whereas PBE indicates the stability at $P = 6.87$ kbar to $P = 31.59$ kbar.

Thus, in summary, the calculation indicates the phase sequence of helium hydrates to be very similar to that of the hydrogen hydrates. This could be expected

Methods	ice-I_h	ice-II	ice-I_c (C_2)	ice-I_c (C_3)
rPW86-vdW2	0.001- 5.26	0.36 - 18.94	1.13 - 33.31	-
optPBE-vdW	0.001 - 5.67	0.70 - 27.40	3.15 - 56.96	82.30 - 100
PBE+D2	1.32 - 14.69	6.84 -26.26	10.46 - 43.36	-
PBE	6.87 - 31.59	31.59 - 69.13	22.10 - 85.19	85.19 - 100

Table 6.5 *Stability range in the He-H_2O system as a function of pressure (unit is in kbar) in different host water networks having fully-filled guest occupancy, using rPW86-vdW2, optPBE-vdW, PBE+D2 and PBE functionals .*

due to the similarities in guest sizes and their interactions with the water host network. The stability fields of the various phases are summarized in Figure 6.6 and Table 6.5. Additionally, the computational results also suggest that there is no qualitative difference among various functionals used. Similar phase sequences have been predicted. However, there is still quantitative discrepancies among different functionals. This results in different phase transition pressures and stability ranges among those functionals. Finally, the S_χ water network, seen in hydrogen hydrate system, is not found stable in the He-water system at any pressure conditions.

6.4.2 Ne-H_2O compound system

Using the same set of host ice structures, the phase diagram of the Ne-H_2O system is computed up to $P = 100$ kbar as well. We found a phase sequence of filled ice-I_h, filled ice-II, and filled ice-I_c with increased pressure, expanding on the only experimentally resolved structure based on filled ice-II [176]. Figure 6.7 shows the convex hull plot at $P = 1$ bar with the rPW86-vdW2 functional. The only stable phases at $P = 1$ atm are based on filled ice-II (shown as red plus symbol) and ice-I_h (shown as blue symbol). A structure based on filled S_χ (shown as purple square) is quasi-degenerate with the ice-I_h phase, with the energy difference around 2 meV/entity at $P = 1$ bar. Both S_χ and filled ice-I_h contain the same amount of Ne (H_2O:Ne=2:1). That neon hydrate based on the S_χ water network is energetically competitive with a filled ice-I_h structure is surprising. This could warrant an experimental re-examination of the low-p/low-T phase diagram of Ne-H_2O. Note that in the otherwise similar He-H_2O system, the S_χ water network is significantly less stable. The structure based on filled ice-I_h remains stable up to $P = 6.18$ kbar. The filled ice-II phase with H_2O:Ne=6:1 is stable in the pressure range from $P = 1$ atm to 23.56 kbar. The sequence of

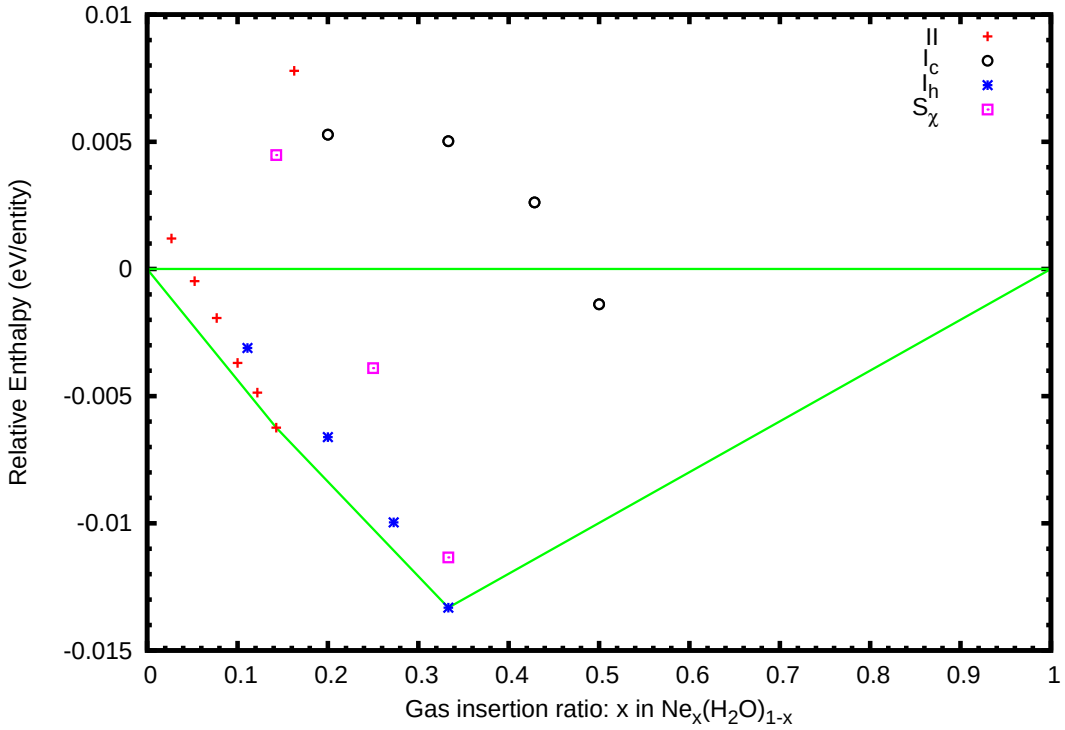

Figure 6.7 *Relative ground state enthalpies of formation for Ne-H_2O phases at P = 1 bar, on the rPW86-vdW2 level of theory. The compound based on fully filled S_χ has a slightly higher relative enthalpy than the structure based on ice-I_h*

phase stabilities is plotted in Figure 6.8. Although a hydrate based on ice-I_c with H_2O:Ne=1:1 is unstable at low pressures, it becomes stable at $P = 2.86$ kbar and remains such up to the highest pressure studied, $P = 100$ kbar. Structures with partially- and overly-filled host cavities were also investigated. Apart from the filled ice-II phase, their relative enthalpies are significantly less competitive than the stoichiometrically occupied phases.

As expected, stable phases in the Ne-H_2O system are calculated to be quite similar to the hydrogen and helium hydrates. This is likely due to the similar guest species sizes in these three compounds. Note that, both the S_χ structure and the phase with the highest guest content, based on filled ice-I_c with a H_2O:Ne ratio of 1:2 (C_3) were not stable in the pressure range studied here. Nonetheless, the S_χ may be more kinetically favourable than the ice-I_h phase. In addition, the C_3 phase may become stable at higher pressures. In Figure 6.8 the metastable phases having an enthalpy difference less than 1 meV/entity from the stable structures are also included. The only thus-defined metastable phases in the Ne-H_2O compound system are based on partially-filled ice-II.

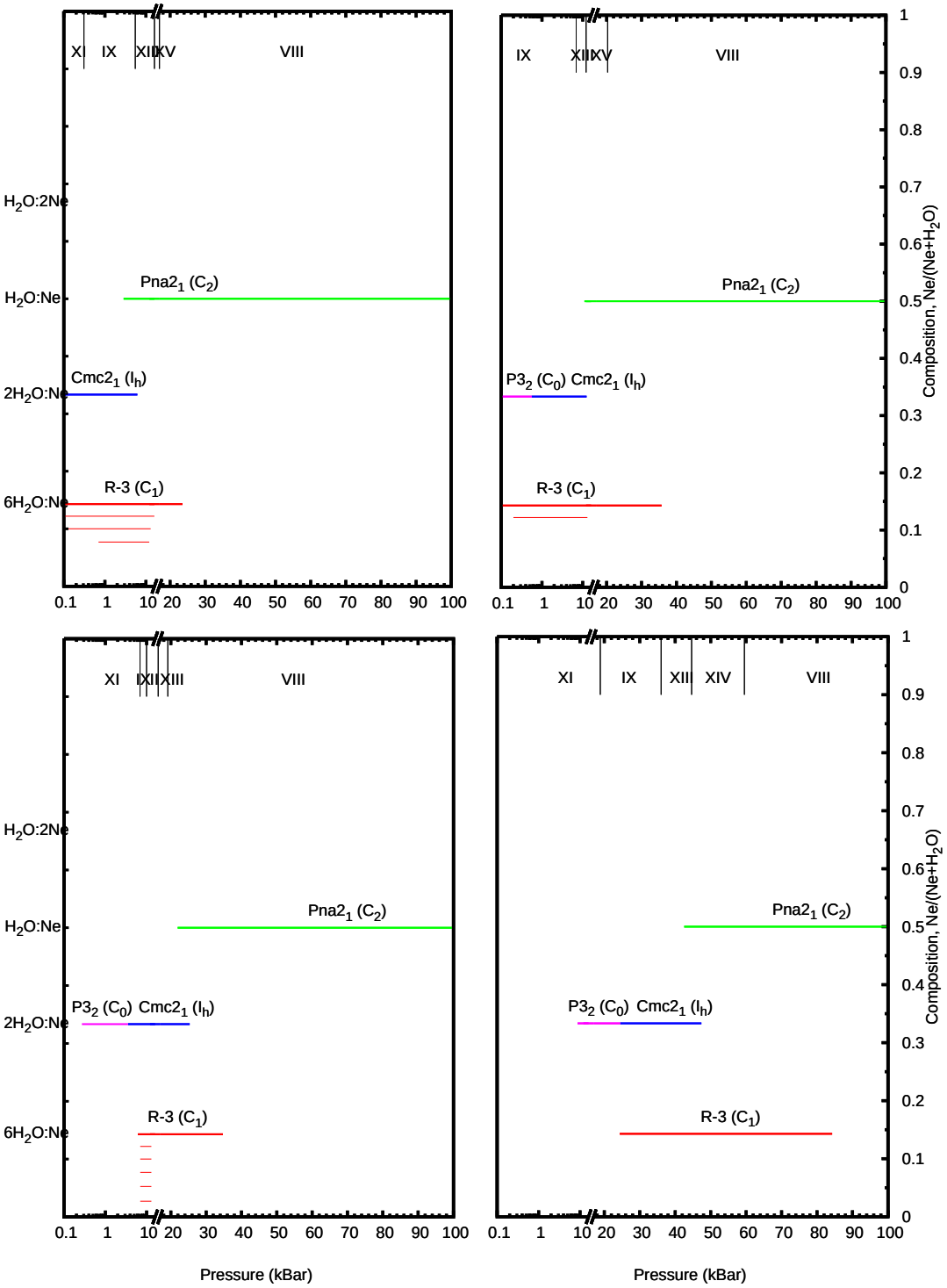

Figure 6.8 *Stability ranges as a function of pressure of the ground state phases in the Ne-H_2O system, using the rPW86-vdW2 (top left), optPBE-vdW (top right), PBE+D2 (bottom left), PBE (bottom right) functional. Information about the host spacegroups following by the notations of the host water networks, shown in brackets, are indicated above the stability ranges. Stability range of ice phases are represented on the top of the graph.*

Methods	S_χ (C_0)	ice-I_h	ice-II (C_1)	ice-I_c (C_2)
rPW86-vdW2	-	0.001- 6.18	0.001 - 23.56	2.86 - 100
optPBE-vdW	0.001 - 0.56	0.56 - 12.45	0.001 - 35.76	11.02 - 100
PBE+D2	0.27 - 3.55	3.55 -25.35	6.12 - 34.75	21.93 - 100
PBE	8.70 - 24.51	24.51 - 47.40	24.37 - 84.25	42.54 - 100

Table 6.6 *Stability range in the Ne-H_2O system as a function of pressure (unit is in kbar) in different host water networks having fully-filled guest occupancy, using rPW86-vdW2, optPBE-vdW, PBE+D2 and PBE functionals.*

The test upon using other three functionals (optPBE-vdW, PBE+D2 and PBE) indicates an interesting result - the S_χ host water network is found to be stable at low pressure with all other three functionals. Although, S_χ host water network is metastable in the rPW86-vdW2 functional compared to filled ice-I_h, the energetic difference between those two water networks is very small (2 meV/entity at $P =$ 1 bar). This suggests a possibility of finding a novel host water network that has not yet been found by experimentalists in this system before. The stability ranges with various functionals in this neon hydrate system is summarised in Table 6.6. Note that, according to the studied pressure in this work (upto 100 kbar), there is not enough information to confirm the existance of the host water network based on ice-I_c (C_3). This C_3 host water network might be found to be stable later at higher pressure beyond 100 kbar.

6.4.3 Ar-H_2O compound system

Ar-H_2O compounds based on the filled-ice water host networks studied here are not supposed to be stable. The only exception to this is a partially-filled S_χ compound. A cavity occupancy of 2/3 (i.e., a Ar:H_2O ratio of 1:3) leads to a relative enthalpy of formation of 3 meV/entity at P=1 kbar – admittedly a very small stabilisation but maybe synthesisable as a metastable phase. Different functionals give slightly larger binding energies: 3.6 and 4.8 meV/entity for PBE+D2 and PBE, at $P = 10$ and 20 kbar, respectively. The structure of the partially-filled S_χ network is shown in Figure 6.9. This metastable phase to the traditional clathrate structure I (sI, with Ar:H_2O=0.148) is compared to structure II (sII, with Ar:H_2O=0.15), shown in Figure 6.10. Both are found to be much more stable, with relative enthalpies of formation of 12 and 11 meV/entity at $P = 1$ kbar, respectively. Nevertheless, from both Ne and Ar hydrates a trend

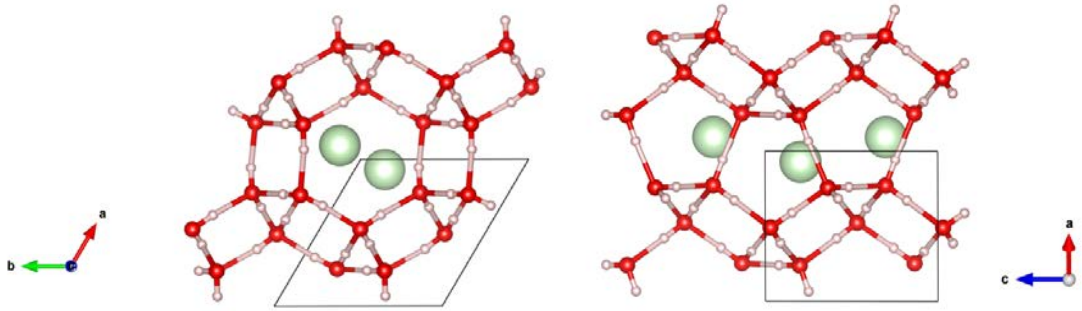

Figure 6.9 *Two views of the partially-filled Ar-C_0 hydrate, along (left) and perpendicular (right) to the channels in the S_χ network.*

emerges - the S_χ network is positioned between the filled-ice and the classical clathrate phases in terms of the sizes of the guest species it can take up.

As expected, Argon is too large to fit comfortably inside the host water networks based on pure water structure. Even applying some amount of pressure cannot stablize the compound. Alternative types of the host water frameworks having a larger empty space are necessary in the the argon hydrate system such as the traditional clathrates structure I and II, or the novel structure S_χ. Since Ar is too big to be fitted in the three empty sites in the S_χ structure, argon adopts the partially-filled having 2/3 occupancy instead. Similar trend of large guest gases adopting the partially-filled S_χ host water network is also confirmed in CO_2 hydrate system [3]. This suggests a possibility of having the S_χ as a host water network in other hydrate systems (e.g. nitrogen hydrates, oxygen hydrates). Further investigations in this area may indicate the existence of a S_χ host water network in those systems.

6.5 Discussion

6.5.1 Cavity size vs host network stability

The discussion on the relationship between cage sizes in clathrates and guest size was initiated by von Stackelberg and updated by Sloan [36, 146]. The very intuitive argument is that guest species of a particular size "fit" or do not "fit" the cages provided by the classical clathrate water networks. Can similar conclusions be drawn for the filled-ice structures, and can the sequence of stable hydrates, e.g. seen in He or Ne hydrates, be rationalized by the pressure evolution of

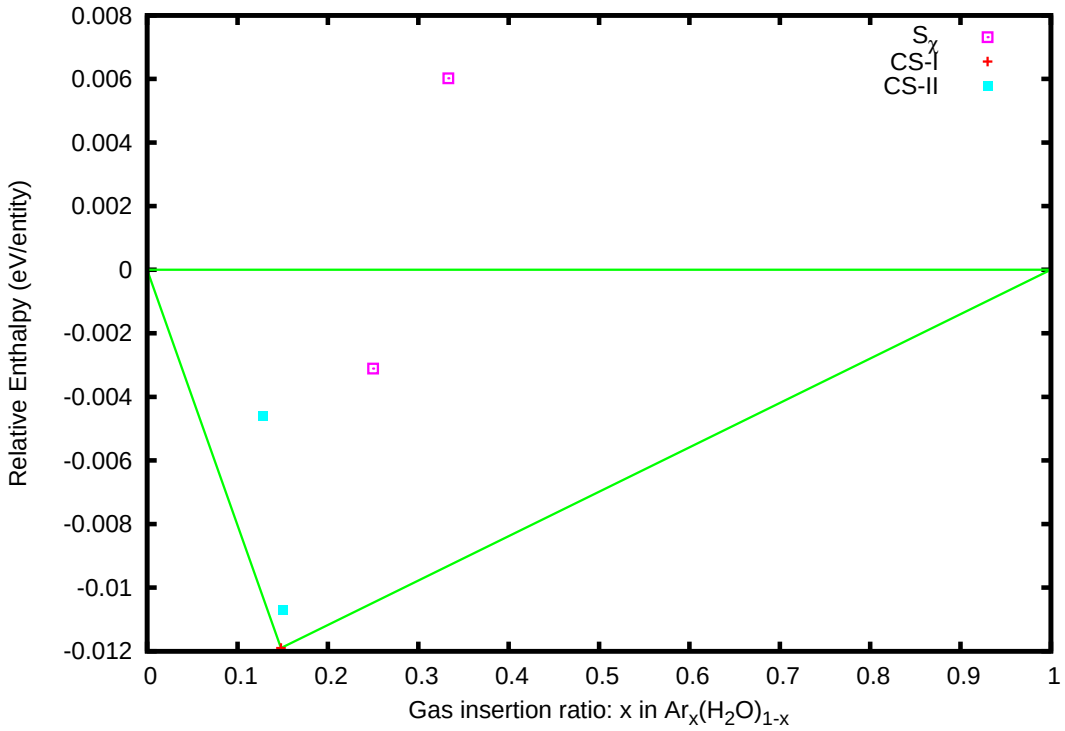

Figure 6.10 *Relative ground state enthalpies of formation for Ar-H_2O system with different guest filling contents based on S_χ, sI and sII host water networks. Calculations were performed using rPW86-vdW2 functional, 1 kbar.*

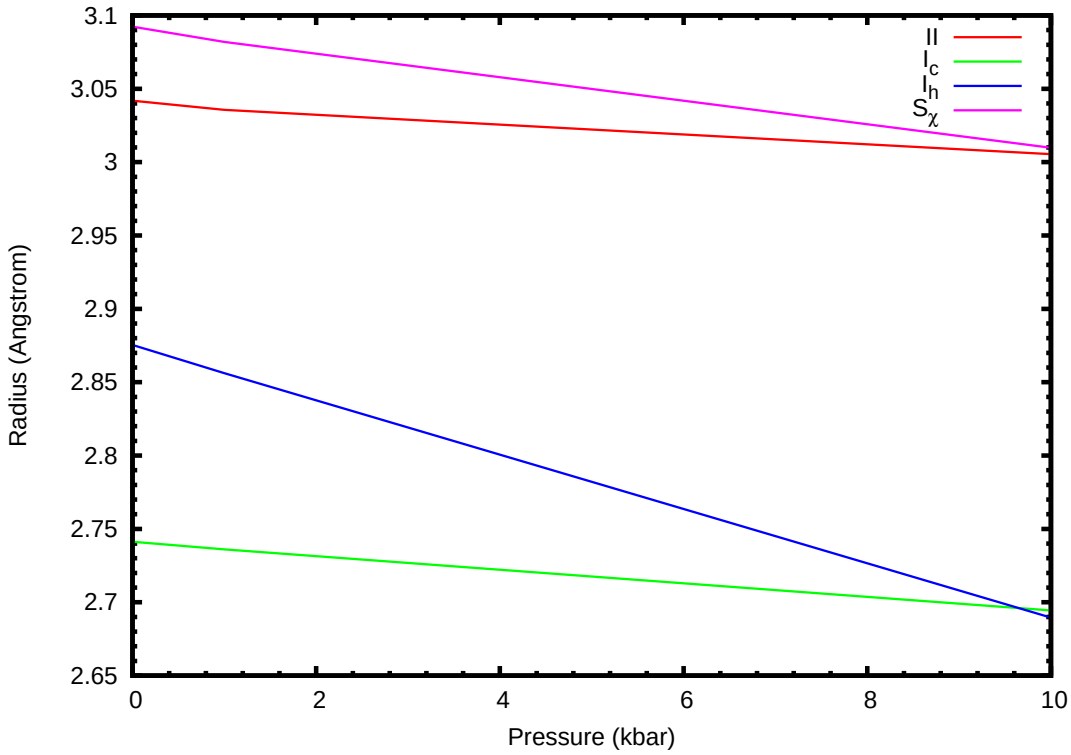

Figure 6.11 *Pressure evolution of cavity sizes of different host water networks from P=1 atm to 10 kbar.*

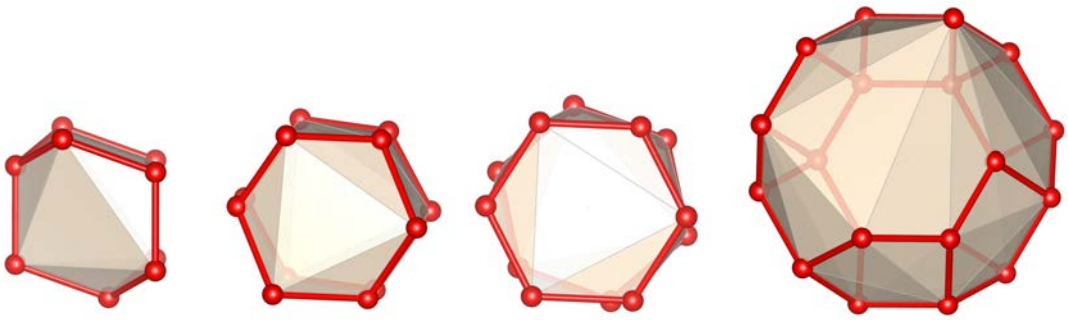

Figure 6.12 *Cavities of different host water networks, ranging from the smallest to the largest, and drawn to the same scale: ices I_c, I_h, II, and S_χ. Protons are omitted.*

the cavity sizes in the water networks? We measured these cavity sizes as the diameters of the largest spheres to be inscribed into the water host structures without touching any of the host network nuclei. The results, obtained from r86PW-vdW2 calculations over a range of pressures (Figure 6.11) indicate that the ambient pressure stable ices I_h and I_c have smaller cavities throughout than the high-pressure phase ice-II, and that the S_χ network has the largest cavities (see Figure 6.12). All filled ices have much smaller cavities (between 2.74 and 3.04Å) than the classical clathrate networks – clathrate structure sII, for example, has a cage size of 4.7Å, according to the same measurement.

Correlating the predicted structural sequence of the noble gas hydrates to the evolution of cavity sizes in their host networks does, however, prove difficult. For example, in He hydrates, the sequence $I_h \rightarrow II \rightarrow I_c$ does not follow a trend that could be related to Figure 6.11. It seems instead that, not surprisingly, the hydrates' host networks correlate to the most stable ice phase in a particular pressure regime (these stability ranges, as calculated from the different functionals, are indicated in Figure 6.6). Comparing different guest species, however, a familiar trend emerges: larger guests favour, under comparable conditions, networks with larger cavities; hence a predicted region of stability for a Ne-S_χ hydrate, and the only metastable filled-ice Ar hydrate, partially filled Ar-S_χ.

6.5.2 Pressure vs volume of the hydrates

In the previous subsection, we examined the pressure evolution of the cavity size of different host water structures. Results indicate that the cage size of empty host water networks decreases upon increasing pressure (Figure 6.11). Therefore, this subsection is dedicated to a rather more detailed study on the effect of pressure on the hydrates. In this case, we focus on the change of unit cell volume as a function of pressure instead of the cavity radius. The main reason for this focus is that it is difficult to define the cavity size in some host water networks, especially the spiral water networks found in S_χ structure.

Our previous definition of measuring the cavity size (i.e. to find the largest sphere that is able to inscribe in the water host structures without touching the host oxygen lattices) might not work very well in this S_χ structure. Thus, the measurement in terms of volume is rather more straightforward.

Intuitively, encapsulations of guest molecules would expand to the size of the host network. However, this idea is not always true for the hydrates as was proposed by Falenty et al. on the neutron diffraction studies of filled neon hydrates and empty hydrates based on sII clathrate [41]. Their studies suggested that in the presence of neon guest atoms, the volume is smaller than empty clathrate. This indicates the importance of the interaction between the water host and neon guest. The shrinkage of volume upon guest intake process highlights a new stability mechanism of filled and empty clathrates. Although there are several ab initio studies on the guest-induced changes to the host water frameworks, none of these are employed DFT studies. Thus, in this section, we present the pressure-volume plots of the noble gas hydrates and their corresponding host water networks (Figure 6.13).

Hydrate phases in the He-H_2O and Ne-H_2O systems were relaxed in order to retrieve their unit cell volumes at pressure from 1 bar to 10 kbar, using rPW86-vdW2 functional. Results from fully-filled and empty hydrate structures in both systems are plotted in Figure 6.13. Neon hydrates (dotted lines) always have larger volume per water molecule than helium hydrates (dotted-dashed lines).

In the presence of the guest species, similar trends of having the unit cell expansion were observed in all types of guest species and host water networks. For example, fully-filled helium hydrate based on ice-II (green colour) has larger volume per water molecule than its empty host phase.

In both ice-I_h (red) and ice-I_c (cyan) host water phases, unit cell expansions are observed in both fully-filled He- and Ne- hydrates compared to their empty phases. The ice-I_c based phases have larger volume expansion than those ice-I_h based hydrates because the ice-I_c host water network has smaller cavity size than the ice-I_h (Figure 6.11 and Figure 6.12).

Fully-filled helium hydrate phase based on the S_χ host structure also have larger unit cell volume per water molecule than its empty S_χ phase (shown in blue).

Additionally, we also performed stoichiometry tests with different guest filling ratios of the host water networks. Results of different guest filling ratios in the S_χ and ice-II host water network are plotted in Figure 6.14. As can be seen in Figure 6.14, the changes in the unit cell volume per water molecule are also governed by the guest filling ratios. Overly-filled hydrates always cause the unit cell expansion; whereas small amount of the guest filling ratios (if compared to its actual filling capacity) tends to have smaller expansion of the unit cell volume.

Higher amount of the guests tends to increase the unit cell size. Moreover, the bigger the size of the guest speies, the larger the unit cell expansion.

In summary, the unit cell volume per water molecule always increases in the presence of the guest gas. The amount of the unit cell expansion depends linearly on the guest size and the amount of guest atoms.

6.5.3 Corrections to the host-guest interaction

The phase diagrams of helium and neon hydrates obtained from four different first-principles descriptions (using the rPW86-vdW2, optPBE-vdW, PBE+D2, and PBE exchange-correlation functionals) produce qualitatively very similar results, as seen in Figure 6.6 and Figure 6.8, respectively. In addition, the same stable phases and transition sequences are predicted with all functionals for He and Ne filled-ice hydrates. However, the predicted transition *pressures* and stability *ranges* of specific phases depend on the specific functional used. This is due to the different descriptions of the host-guest interactions by these functionals. For instance, as seen in Figure 6.3 and Table 6.2, the rPW86-vdW2 approach provides accurate host-guest equilibrium separations, but tends to overestimate the interaction energy. This overbinding effect may shift the phase stabilities of hydrate phases towards lower pressures than seen experimentally. In our ground state energy calculations, the rPW86-vdW2 functional suggests the stabilities of some phases at pressure as low as P=1 atm. The pairwise PBE+D2 correction suffers from combined effects of too-short equilibrium separations and overbinding of the host-guest interaction. While overbinding prefers to stabilize the hydrate mixtures at low pressures, a significant compression of the network structures is needed to benefit from the attractive part of the host-guest potential energy surface. As a result, the PBE+D2 calculations yield narrower regions of stability, which commence at higher pressures than in the rPW86-vdW2 calculations. In the case of PBE, the host-guest binding energy is slightly overestimated, while providing an almost correct equilibrium separation. However, PBE and other semilocal GGA functionals tend to overestimate the stability ranges of molecular ice networks by almost an order of magnitude (see Figure 6.3)[63], and are only appropriate to describe ice phases at much higher pressures [60, 61]. It is then likely that the stability ranges of the gas hydrates are similarly overestimated. In fact, studies on the phase transitions of molecular ice phases using various functionals have shown that the rPW86-vdW2 approach

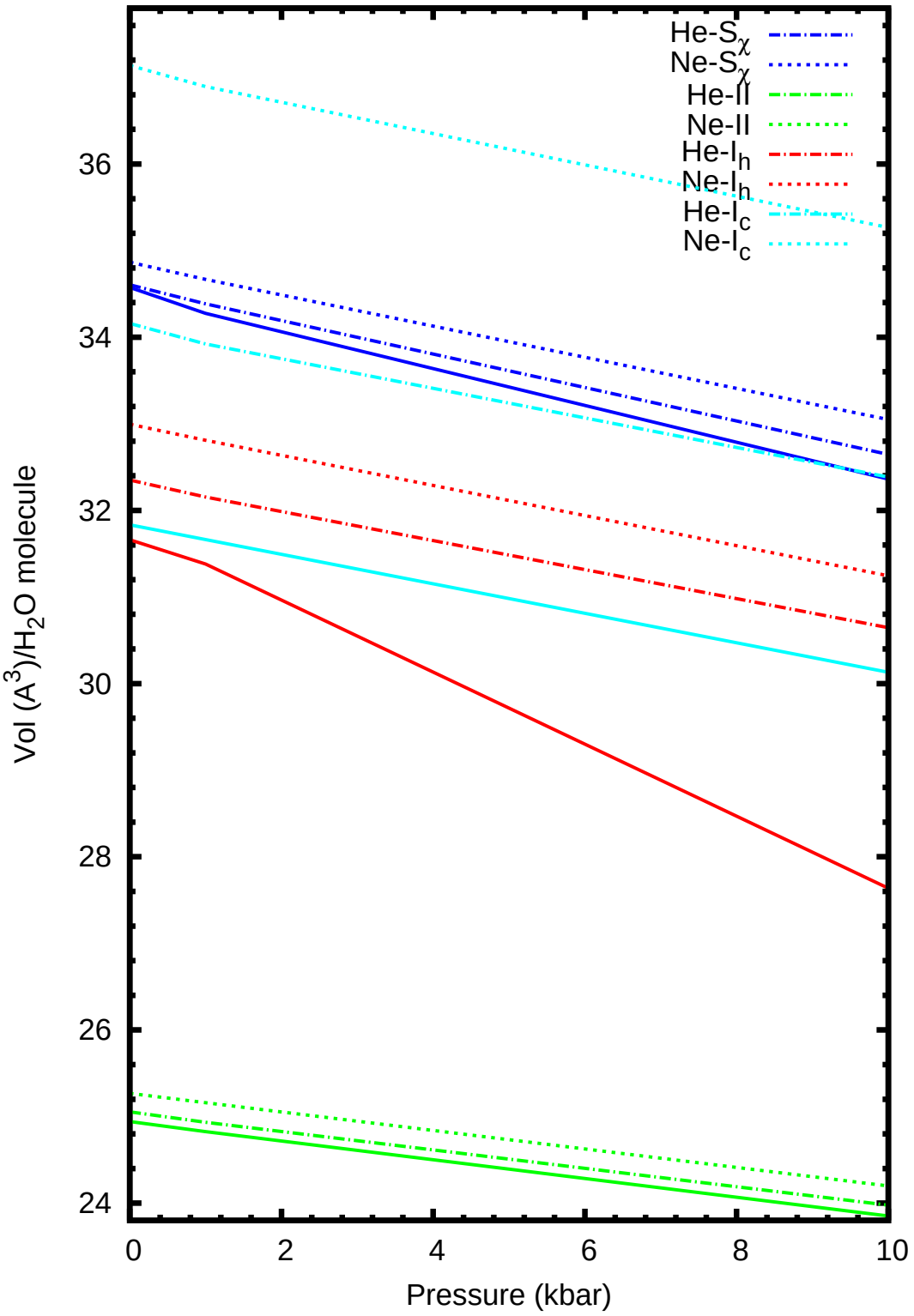

Figure 6.13 *Pressure versus volume plots of empty host water phases (solid lines), fully-filled He-H_2O hydrates (dotted-dashed lines) and Ne-H_2O phases (dotted lines), showing results from rPW86-vdW2 functional.*

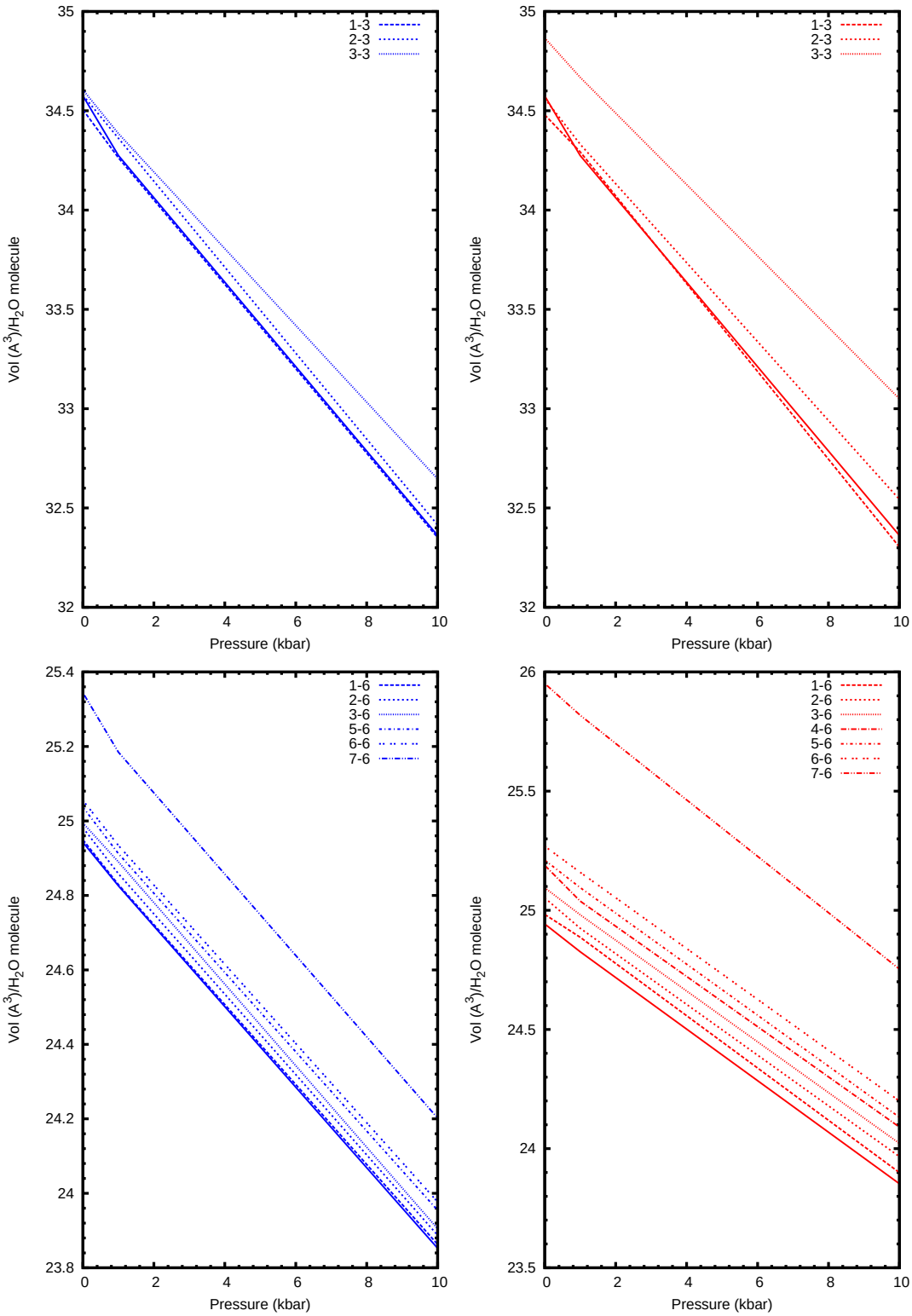

Figure 6.14 *Pressure vesus volume plots of empty, partially-filled, fully-filled He- (left) and Ne hydrates (right) based on S_χ (top) and ice-II (bottom) host water network. Solid lines represent empty hydrates; whereas dotted lines are filled hydrate phases with guest filling ratios indicated in the label.*

provides very good agreement with experiment [136, 137]. Therefore, we assume that the rPW86-vdW2 approach will be the most accurate method for comparing the relative enthalpies of systems comprising different water networks.

An ad-hoc correction is possible, using the quantum chemical potential energy surface of He-H_2O shown in Figure 6.3. We can correct the total energy of the hydrate phases by performing a many-body decomposition of the total energy into monomer and dimer terms; and replacing the guest-water dimer rPW86-vdW2 interaction energies with CCSD(T) values:

$$\Delta H_f(\mathrm{He_n(H_2O)_m}) = \Delta H_f^{\mathrm{DFT}}(\mathrm{He_n(H_2O)_m}) + \Delta H_{corr}$$

$$\Delta H_{corr} = \int dr g_O(r)(E_{PES}^{\mathrm{CCSD(T)}}(r) - E_{PES}^{\mathrm{DFT}}(r)) \qquad \text{(Eq. 6.1)}$$

Here, the relative enthalpy of formation is corrected by subtracting the DFT overbinding and adding the CCSD(T) interaction energy for the host-guest interaction instead. The energies $E_{PES}(r)$ are shown in Figure 6.3, and weighted with the radial oxygen distribution $g_O(r)$ at distance r from the guest atoms. Figure 6.15 illustrates the influence of the correction term. There, the guest-oxygen neighbour histogram is shown, the difference between the rPW86-vdW2 and CCSD(T) dimer potential energy surfaces shown in Figure 6.3, and the resulting energy correction according to equation above (Eq. 6.1). The integrated DFT overbinding in the hydrate is estimated to be 40 meV per guest atom, and is dominated by the first water coordination shell, which makes up the cavity.

By supplanting the total energies from the rPW86-vdW2 functional with CCSD(T) results for the He-H_2O dimers for each phase and pressure, the convex hull plots (such as Figure 6.5 for He-H_2O and Figure 6.7 for Ne-H_2O) can be adjusted. The revised relative enthalpies of formation are compared to the original results in Figure 6.16 for He at P = 1kbar, Figure 6.17 and Figure 6.18 for Ne at P = 1bar and P = 1kbar, respectively.

A convex hull plot of the helium hydrates at 1 kbar after adding a correction is shown in Figure 6.16. New tie lines are shown in brown colour whereas the previous tie line are shown in green colour. Arrows indicate the amount of correction energy. Small symbols represent previous results; whereas large symbols are the corrected CCSD(T) values to those previous results. According

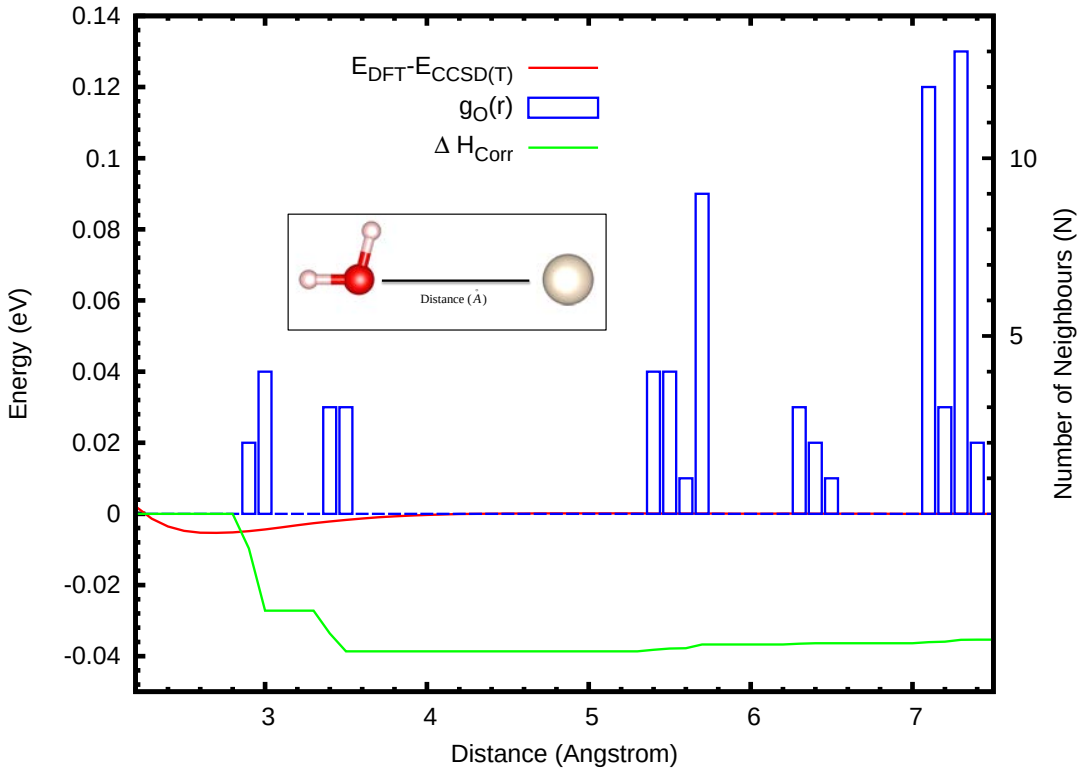

Figure 6.15 *He-H_2O in the filled ice-I_h framework at 1 bar: He-O neighbour histogram as bar plot; the difference between the DFT and CCSD(T) potential energy surface for the configuration shown in the inset (red); and the integrated energy correction (green).*

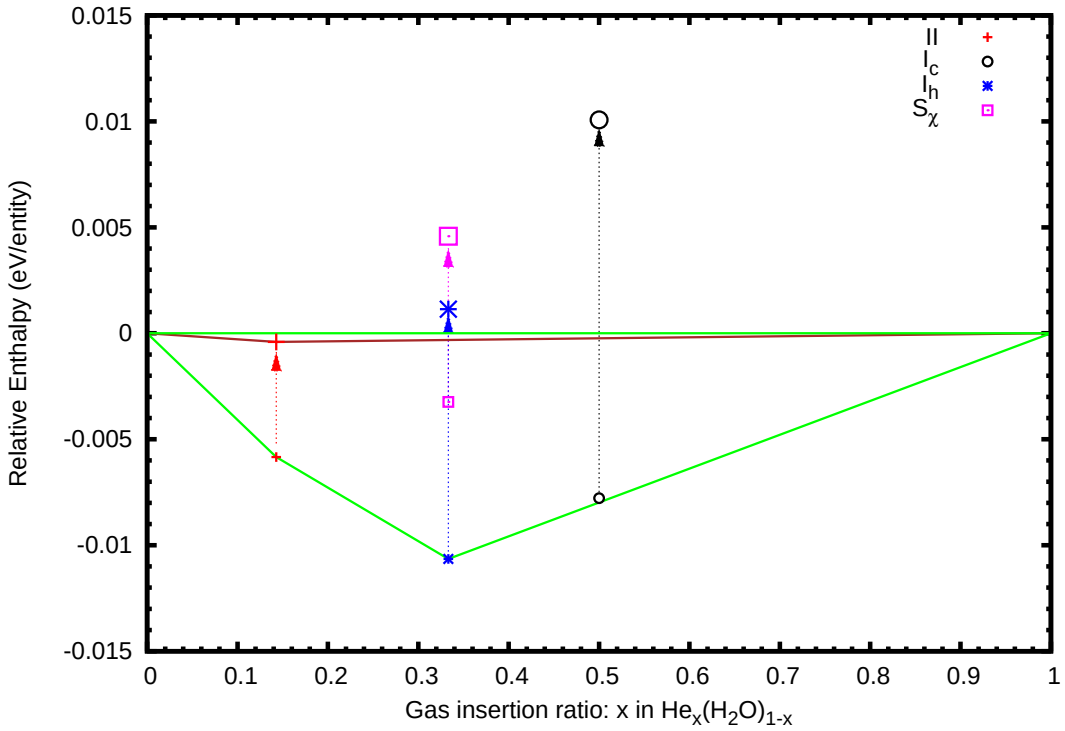

Figure 6.16 *Comparison of the relative ground state enthalpies of formation for fully-filled He-H_2O phases at $P = 1$ kbar, showing results from rPW86-vdW2 (small symbols) and the corrected CCSD(T) values for the He-H_2O interaction (large symbols), respectively.*

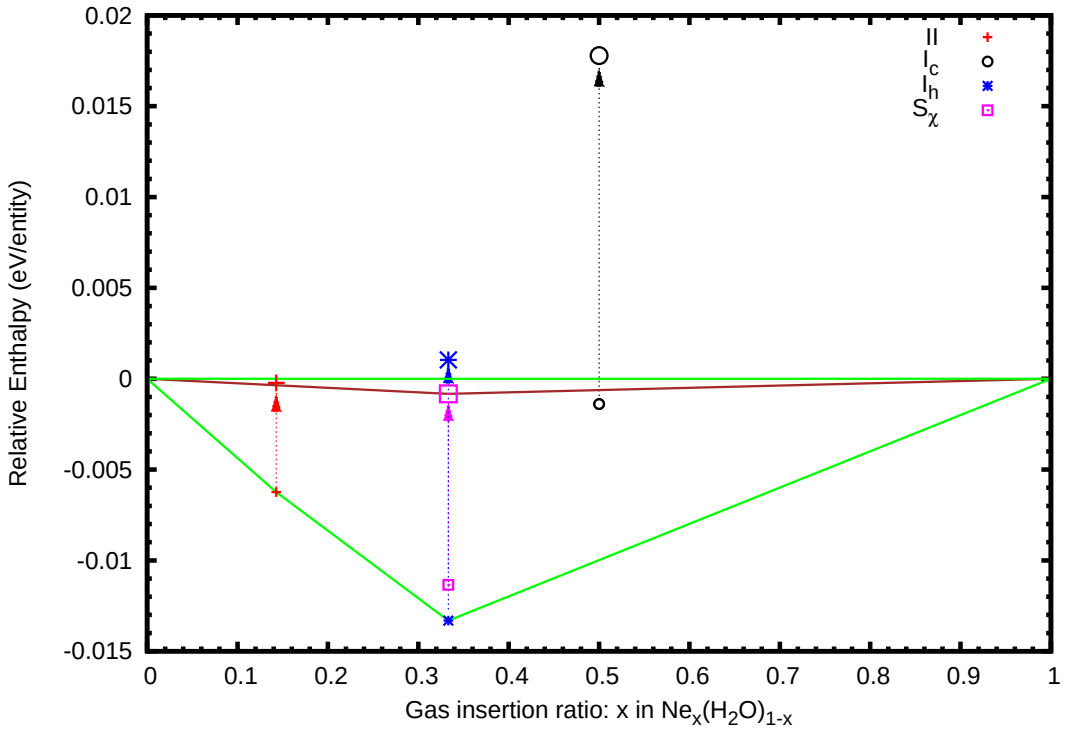

Figure 6.17 *Relative ground state enthalpies of formation for fully-filled Ne-H_2O phases at $P = 1$ atm, showing results from rPW86-vdW2 (small symbols) and the corrected CCSD(T) values for the Ne-H_2O interaction (large symbols), respectively.*

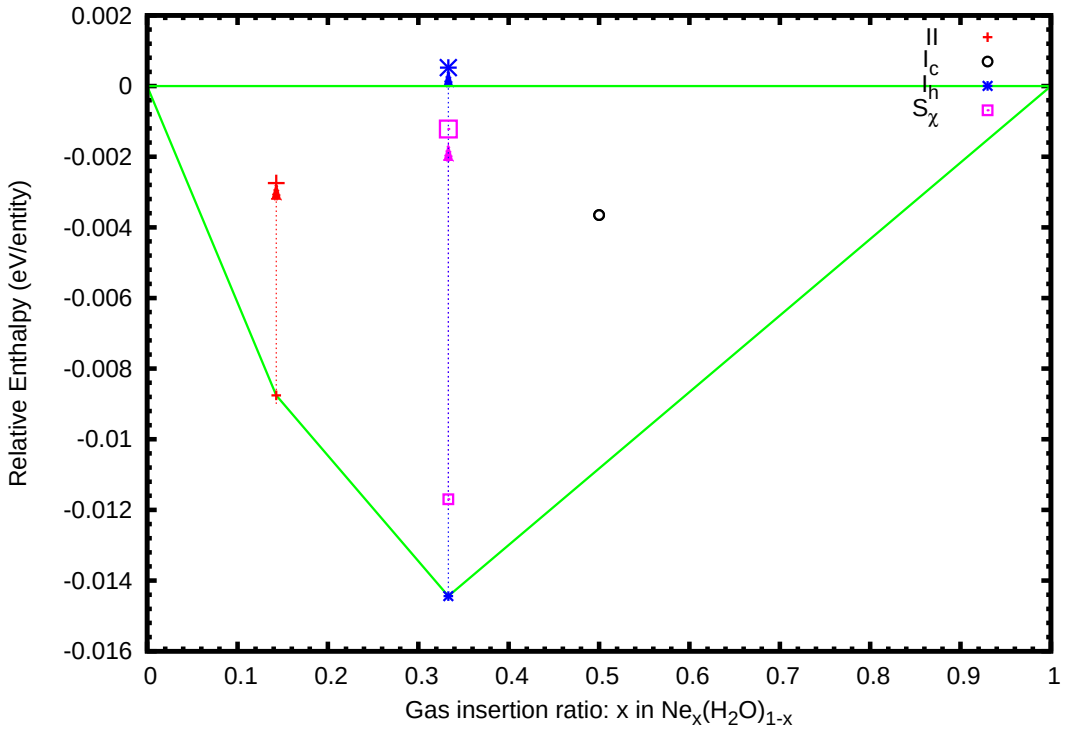

Figure 6.18 *Relative ground state enthalpies of formation for fully-filled Ne-H_2O phases at $P = 1$ kbar, showing results from rPW86-vdW2 (small symbols) and the corrected CCSD(T) values for the Ne-H_2O interaction (large symbols), respectively.*

to Figure 6.16, only ice-II based hydrate is stable in the He-H_2O system after adding the correction. Note that the relative enthalpy of formation of the helium hydrate phase based ice-II is very small (< 1 meV). The stability pressure range of the ice-II based phase is very narrow, we cannot see its stability at the previous and next studied pressure (i.e. at 1 bar and 10 kbar).

Corrections made to the neon hydrates are shown in Figure 6.17 and Figure 6.18. At 1 bar, only C_0 phases is stable after adding the correction, while ice-II is metastable (with very minute amount of energy from the tie lines). The result at P = 1 bar is in contrast to the results before the correction; that is, the C_0 phase is predicted to be stable rather than the ice-I_h phase. The stability pressure range of the C_0 phase is less than 1 kbar since we can only find the ice-II phase to be stable at 1 kbar (Figure 6.18). The hydrate phase based on ice-II water structure are predicted to be stable up to 30 kbar.

It is, however, not clear whether density functional theory overestimates the host-guest interaction in the condensed phase to the same extent as seen in the He/Ne-H_2O dimer. Comparison between DFT and quantum chemistry results on the $He(H_2O)_{12}$ cluster suggests less overestimation energy than those found in the dimer. This implies that the energy overestimation might be smaller in the solid phases. Delocalization of electron densities and screening effects could lead to a better density functional-based description of the solid phases than the gas phase dimer; therefore, the corrected relative enthalpies of formation from Figures 6.16 and 6.17 represent upper bounds for these hydrates. Moreover, the He/Ne-H_2O interaction depends quite strongly on the relative orientation of the water molecule to the noble gas atom.

Ultimately, using for instance the local-MP2 approach or a many-body decomposition of the total energy such as implemented in the method of increments would replace the simple energy correction in this work in a more general and systematic manner. This would enable better judgement on the quality of density functional theory to describe these gas hydrates [39, 116, 147].

6.6 Conclusions

In summary, the ground state phase diagrams of noble gas-water compounds have been predicted, based on first-principles calculations of various filled-ice

structures. Four distinct host water networks, namely ices I_h, II, and I_c, as well as the new water network S_χ are used to determine stable phases for both the helium and neon compound systems.

The predicted phase evolution of the He-water system agrees very well with the stable structures found in the hydrogen-water system: stable phases based on the host water networks of ice I_h, II, and I_c were found, in that order, upon increasing pressure. At very low pressure, the recently discovered water network S_χ was found to form a stable Ne hydrate. Note that this is functional dependent - three out of four functionals tested in this work indicated the stable S_χ hydrate. Since the S_χ might be a competitive phase at low pressure, the phase sequence of stable Ne-water compounds is summarized as (S_χ), ice-I_h, ice-II, and ice-I_c host water networks, in that order, upon increasing pressure. The S_χ host water network has not yet been found by experimentalists in the Ne-H_2O system. Therefore, this work suggests a possibility of finding a new phase in the neon hydrate system at low pressure. Regarding possible filled-ice Ar-water mixtures, only one metastable structure was found, based on the S_χ host network, with partial occupancy of the guest sites. Such a partial occupancy in S_χ structure is observed in large guest species (e.g. CO_2) as well. This S_χ hydrate is metastable with respect to the well-known clathrate structure I (sI) and structure II (sII).

Although having quantitative differences, different exchange-correlation functionals showed qualitative agreement irrespective of the particular density functional used. Accurate prediction on stability range depends on the chosen functional. The results also indicated that the interaction energy between the host and guest species tend to be overestimated with all the density functional methods used. While this overbinding might be less pronounced in the extended state, it could lead to an overestimation of the stability of the hydrate mixtures, as compared to the separated constituents. A simple correction of the pairwise host-guest interaction, using coupled cluster results for the dimer potential energy surface, should providing an upper bound for the hydrate binding energies was used. Such a correction led to metastability of most of the considered hydrates structures. Specialized treatment of the weak host-guest interactions, for example with local-MP2 or incremental methods, might be instructive and lead to further insight into these systems. In collaboration with the Prof. Paulus' Group in Berlin on the noble gas-water cluster $Ng(H_2O)_{12}$, the charater of these interactions was studied. The binding energy obtained by using the method of increments and local MP2 approaches indicated that slightly less overbinding occurred in the

large cluster than the dimer. This might imply that the overbinding effect from density functional methods has less influence in the solid phase than the dimer test system. However, further studies on the effect of the dispersion energy in a solid system are still required.

Chapter 7

Hydrogen Hydrates

7.1 Introduction

Hydrogen hydrates have received much attention among the gas hydrate systems due to their potential materials for an alternative environmentally clean energy replacing fossil fuels [149]. In addition, icy moons or planets have been found to be composed of a mixture of water ice and hydrogen, which forms hydrogen hydrates under pressure [51]. Therefore, the study of the hydrogen hydrates provides useful information i.e. at what pressure conditions the hydrogen hydrates were formed and their structure at that pressure.

Like other clathrate hydrates, hydrogen hydrates are found to be stabilised at low temperatures and small applied pressures, in kbar region. Hence, experiment, mostly by x-ray diffraction, has been performed to obtain the crystal structures of the hydrogen-water compounds at the pressure lower than 0.2 GPa. Limited studies at higher pressure above 0.2 GPa lead to unclear structural details at high pressure. Although the missing information on the crystal structures are often inferred from other clathrate hydrates having similar guest's size such as helium hydrates, some evidence suggest that different clathrate structures form in the hydrogen and the helium hydrate system [32].

One of the difficulties in finding crystal structures in the hydrogen hydrate system is due to the fact that hydrogen is so light, having less pronounced scattering from the electron cloud if using x-ray diffraction technique. Thus, alternative method such as neutron diffraction is required for obtaining the crystal structures of the

hydrogen hydrate system. However, neutron facilities are far less accessible than the x-ray resources. Consequently, not so much work has been performed in the investigation of the crystalline structures in this compound system.

Computational studies in this chapter are useful in filling in the experimental gaps. Theoretical structural predictions are proven to be one of the alternative tools in the gas-clathrate studies, especially when there are unresolved mechanisms or crystal structures. There are two main topics in computational studies. First, static studies i.e. to obtain crystalline structural information, to predict the structure having lowest energy at specific pressure and then contruct phase diagrams. Second, dynamics studies i.e. to investigate the mobility and diffusing of guest gas molecules embedded in the host water networks and hence establish the transition states. This work contains both parts. First, to investigate the missing structural information and/or to confirm the already existed structures by constructing the hydrogen hydrates' phase diagrams upto 10 GPa. Additionally, we also probe the ability of the DFT's exchange-correlation functionals on which functional is suitable to describe the hydrogen hydrates. Second, to study the dynamics of the hydrogen guest molecule along the channels and cavities in different host water structures.

7.2 Previous Experimental Studies

So far, experimental studies of the hydrogen hydrates, mostly by x-ray diffractions, report four known host water phases based on sII, S_χ, ice-II, and ice-I_c upon increasing pressure. Out of those four host water structures, the clathrate structure II (sII) and the two ice based hydrates, C_1 based on ice II and C_2 based on ice I_c, have been extensively studied [165, 166].

The C_1 and C_2 phases were the first phase discovered in the hydrogen hydrate system by Vos et al [166] at the pressure between 0.75 and 3.1 GPa (295 K). A combination of high-pressure optical and x-ray diffraction studies helped determining the structure of this C_1 phase to be a rhombohedral unit cell. This rhombohedral hydrate is similar to the structure of ice-II, which has already been found in the helium hydrate system [105]. Raman studies estimated water:hydrogen ratio between 10:1 and 5:1 [166]. Above 2.3 GPa, this rhombohedral phase transformed to a cubic phase, that has a unit cell similar to that of ice-I_c. Raman spectroscopy technique suggested the C_2 phase had a 1:1

water:hydrogen content [165]. In 1999, Dyadin et al can reproduced the same dissociation curve and suggested a cubic clathrate hydrate at a lower pressure between 0.2 and 0.4 GPa [33]. This cubic clathrate structure was later resolved in 2002 to be based on sII clathrate by Mao et al at pressure around 0.2 GPa [109].

Having used several techniques i.e. infared, Raman, x-ray and neutron diffraction, Mao et al [109] were able to determine the exact number of hydrogens inside both the large and small cages. The results suggested 4 and 2 hydrogen molecules per large and small cage, respectively. In 2004, Mao and her co-workers refined the measurement and suggested 4 and 1 hydrogen molecule per cage at low temperature [103]. The pressure and temperature dependencies govern the amount of hydrogens in both cages.

The phase C_0 was just recently discovered by Efimchenko et al. in 2011 via x-ray powder diffraction having a trigonal unit cell (with $P3_112$ symmetry with a = 6.33 Å and c = 6.20 Å) at the pressure between the phase sII and C_1 (around P = 5 kbar) [37] . Strobel et al refined the unclear diffraction peaks found by Efimchenko by collecting in-situ x-ray data and concluded that the C_0 diffraction pattern is similar to an α- or β-quartz, or the tetragonal structure (sT) [148]. Thus, two more structures had been proposed, namely the tetragonal sT' structure ($P4_2/mnm$ with a = 6.25 Å and c = 10.67 Å) and the α-quartz trigonal structure ($P3_221$ with a = 6.24 Å and c = 6.18 Å). Smirnov et al. performed a classical molecular dynamics study and suggested that C_0 had a spiral structure containing hydrogen molecules in the channels [145]. Recent in situ XRD study in 2016 by Strobel et al [150] concluded that the oxygen sublattice was closely matched with the one proposed by Smirnov et al but with hexagonal symmetry. A neutron diffraction study of the empty C_0 water network recovered to ambient pressure had been proposed to have hexagonal symmetry ($P6_122$) [131]. While there is a significant amount on the suggested structural data on the C_0 network, limited studies have been performed to retrieve a full determination of its structural data. Most recently, in 2017, neutron and x-ray diffraction studies performed by Amos et al. [3] refined the structural data observed in both CO_2 and H_2 hydrates based on C_0 network and proposed a hydrogen-bond network S_χ with spacegroup $P6_522$. This chapter uses the structure proposed by Amos et al [3] and adopted the structure S_χ to refer to the host water network C_0 instead of the ambiguous notation C_0, which has several structures proposed by different researchers.

Thus, in summary, the experimentally known host water networks in the hydrogen hydrates system are sII (P = 0.2 GPa), S_χ (P = 0.5 GPa), ice-II (P = 0.75 - 3.1 GPa), ice-I_c (P > 4.6 GPa) [3, 109, 165, 166].

Theoretical Study

A recent computational paper by Qian et al [125] explored the H_2-H_2O system having almost all the currently known host water networks mentioned above namely sII, C_0, C_1, and C_2 by DFT calculations in the pressure range 0-100 GPa. In addition they also proposed two novel theoretical predicted phases named "I_h-C_0" and C_3. These two phases were produced by the evolutionary algorithm USPEX [120]. The "I_h-C_0" phase had a stability range and a guest insertion ratio similar to that of C_0 (2:1 water:hydrogen ratio) and represents a fully filled ice-I_h water network. Although both the C_2 and C_3 phases are based on ice-I_c water host water framework (with 1:1 and 1:2 water to hydrogen ratio, respectively), they differ in whether the guest molecules are located at the middle or at the edge of the host water network's cavities. According to their results, the phase diagram of hydrogen hydrates is theoretically proposed as follows: a novel clathrate structure C_0 (P < 0.24 GPa), "I_h-C_0" (P = 0.24 - 2.1 GPa), C_1 (P < 3 GPa), C_2 (P = 1.7 - 10 GPa), C_3 (P > 40 GPa).

Although the theoretical phase diagram prediction by Qian et al [125] provide us with an intuitive idea for the phase sequence in the hydrogen hydrate systems. They have found the sII phase to be metastable with a 0.013 eV/molecule higher energy than the stable decomposition constituents. In addition, there is little detailed information provided on the sII phase employed in their paper, i.e. stoichiometry and spacegroup. This incomplete data does not confirm the experimental existance of the sII based phase. This chapter also focuses on testing the DFT functionals because dispersion interactions play significant role in the water ice [137] and no research so far has been performed to test which is the right DFT functional suitable to describe the interactions in the gas-water compounds. Various dispersion corrections in the exchange-correlation functionals (semi-local, semi-empirical, and non-local density based functionals) have been employed. Results obtained from this study will be used as a test chart to compare with experimental data. This might help to find the reason why sII phase is computationally found to be metastable [125].

Although several theoretical and experimental studies have been performed to figure out the guest ocupancies in the structure sII [103, 109], little DFT

study has been conducted due to the large unit cell size of the structure sII. The right amount of the the guest hydrogen might govern the stability of the gas-water compound based on this sII hydrate. Therefore, in this study, the hydrogen occupancies inside both small and large cages of the sII hydrate are computationally investigated to obtain the suitable amount of hydrogens having lowest energy at each pressure studied (upto 10 GPa).

7.3 Methodology

At each pressure step, the crystal structures were relaxed by using density functional theory (DFT) [71, 91] and the projector augmented wave (PAW) method [17, 94] implemented in the VASP code [93]. The plane wave cutoff energy ($E_c = 875$ eV) and Monkhorst-Pack k-point meshes [114] (density $20/\text{Å}^{-1}$) were chosen to be large enough to fully converge total energies. The relaxation's criteria were set as the net forces were less than 2 meV/Å, the final energy difference between the self-consistency loop is less than 10^{-7} eV/ unit cell. Dispersion corrections of long-range electronic correlation effects were included in the structural relaxations along with the standard Perdew-Burke-Ernzerhof (PBE) exchange-correlation functional [122]. Both semi-empirical PBE+D2 [50] and the non-local dispersion functional electron density-based vdW-DF approach [27] were used in this study. Several dispersion correction functionals in the vdW-DF family [27] had been employed: rPW86-vdW2 [100], optPBE-vdW, optB86b-vdW, optB88-vdW [83, 84].

Information on relaxed crystallograpic structures at 1kbar using rPW86-vdW2 functional for solid hydrogen, pure water ice, and hydrogen hydrates used in this chapter are tabulated in Appendix B.

7.4 Effect of proton configurations in hydrogen hydrate compounds

Rich varieties of the proton-ordered phases and their proton-disordered counterparts are found in the phase diagram of ice. It is also known that the arrangement of protons in the ice structure contributes to the phase transitions. The advent of the theoretical proposed anti-ferroelectric structure for proton ordered ice I_h

with spacegroup $Pna2_1$ that was found to be more computational stable than the ferroelectric model $Cmc2_1$ [26]. This has attracted attention from researchers in this field. Thus, the existence of proton-ordering structures found in water ice networks governs the phase transition pressure of water ice.

In Chapter 5, several investigations on the effect of proton ordering in water ice networks (ice-I_h, ice-II, S_χ, clathrate structure I, II, T) have been performed. Unsurprisingly, the energetic contribution among various arrangements of hydrogen positions in the pure water network is very small (in the order of 10 meV/water molecule). This energy gap agrees very well with other computational results [69]. Nevertheless, we may not conclude that this protonic effect is also trivial in the gas-water compound. Therefore, calculations on the gas-water compound using the same sets of proton configurations in the host water networks are computed.

In the hydrogen hydrate system, the theoretically predicted phase similar to the ice-I_h structure named "I_h-C_0" with a spacegroup Cc was found to be a competitive phase at low pressure [125]. Note that the phase based on ice-I_h network is still not found experimentally to exist in the hydrogen hydrates, although it is found in noble gas hydrates (both helium and neon hydrates). Thus, in this research, those three different proton-orderred ice-I_h phases are studied by calculating their enthalpies with a function of pressure. The comparison among these three configurations will provide insight on how much the effect of the protonic arrangement is in the host water ice network with the hydrogen hydrate system.

Full information on the host water networks, their enthalpy differences between the configurations having the highest and the lowest enthalpy, and the numbers of tested configurations are listed in Table 7.1. Calculations were performed using rPW86-vdW2 functionals at P = 1 bar.

According to Table 7.1, the enthalpy differences of the hydrates with various host water networks are mostly around 2-4 meV per water molecule. Except for the hydrogen hydrate phase based on ice-II structure, 12.3 meV/H_2O molecule was predicted for the enthalpy difference between the configurations having the highest and the lowest enthalpy. This value is about a half of the enthalpy difference found in pure ice-II. This implied that, the enthalpy spread among various proton configurations based on ice-II structure is smaller in the presence of the guest gas species. In contrary, for both sI and sII host water networks, slightly higher spread of the enthalpies were observed in the hydrogen hydrates

Hydrogen hydrate structure	Δ H (meV/H_2O molecule)	Numbers of tested configurations
ice-I_h	2	3
ice-II	12.3	22
sI	4	4
sII	4	4

Table 7.1 *Host water networks, their enthalpy spreads between the configurations having the highest and lowest enthalpy, and the numbers of tested configurations in the hydrogen hydrates. Calculations were performed at the rPW86-vdW2 level of theory at P = 1kbar,*

compared to pure host water clathrates. Note that, only certain configurations of the host water structures were used in this comparison. Thus, there is still insufficient data to draw a valid conclusion on the effects of proton configurations in the gas hydrate compounds.

7.5 Dispersion Effects in H_2O-H_2 dimer system

To understand the dispersion effects in this hydrogen-hydrate system, different functionals are tested in this study. These include the non-local density-based approaches (i.e. vdW-DF family: rPW86-vdW2, optPBE-vdW, optB88-vdW, and optB86b-vdW), the semi-empirical PBE+D2, and the semi-local PBE functionals. As mentioned in the previous chapter, it is still unclear which functionals are best suited to describe the gas hydrate system. Therefore, the calculations using these functionals should provide insightful results to help understanding the dispersion interaction in the hydrogen hydrate systems.

Before investigating the hydrates, we want to test the dispersion effects in a simple decomposed system - in this case it is a dimer of a hydrogen molecule and a water molecule. Results from a dimer system with various functionals will be compared to those obtained from a solid system. Comparison between the dispersion effects in a dimer and a solid system would provide us an idea of how important the dispersion corrections in both systems are.

The potential energy surface of a hydrogen molecule and a water molecule is computed by DFT using VASP program (with various functionals mentioned above) and compared to results from quantum chemistry approach (second-order Moller-Plesset perturbation theory (MP2) [112] and coupled-cluster calculations

Methods	H_2
MP2	(3.42, -3.04)
CCSD	(3.30, -3.15)
CCSD(T)	(3.31, -3.47)
PBE	(3.40, -3.54)
PBE+D2	(3.10, -9.86)
optB86b-vdW	(3.60, -6.23)
optB88-vdW	(3.70, -2.72)
optPBE-vdW	(3.30, -14.97)
rPW86-vdW2	(3.20, -9.06)

Table 7.2 *Hydrogen-water interactions from various methods. The interaction results of each hydrogen molecule (equilibrium distance d_{O-H_2} in Å, binding energy E_0 in meV).*

(CCSD(T) level) [23] using Gaussian program [45]. Those calculations used augmented quadruple-zeta correlation consistent basis sets (aug-cc-pVQZ). The results of the hydrogen-water interaction from different methods are shown in Figure 7.1. Table 7.2 lists the equilibrium distance d_{O-H_2} in Å, binding energy E_0 in meV. It is clear that the PBE binding energy deviates least from the gold-standard CCSD(T) result, while other DFT functionals tend to overestimate the binding energy significantly. However, all the vdW-DF family functionals predict quite accurately the equilibrium separations d_{O-H_2}. This implies they should provide accurate geometries of the hydrates, while strong overbinding could mean an artificial stabilisation of the compounds compared to the constituents. The results indicate that there is not a lot of difference in the binding energy and the equilibrium distance among all the vdW-DF family functionals.

Note that such overestimation of the interaction energy of the dispersion-corrected density functional theory is also found in the noble gas-water dimer system (Figure 6.3, Table 6.2). While the semilocal PBE still deviates least from the CCSD(T) result in the noble gas-water dimer, it still overestimates the binding energy about a factor of 1.4 in the helium water dimer. This overestimation is quite high compared to the PBE result in the hydrogen-water dimer system, which matches up very well to the CCSD(T) potential energy surface. However, the overestimation of the binding energy found in the dispersion-corrected DFT functionals is speculated to be lower in the solid phase than the dimer, as was found in the noble gas system.

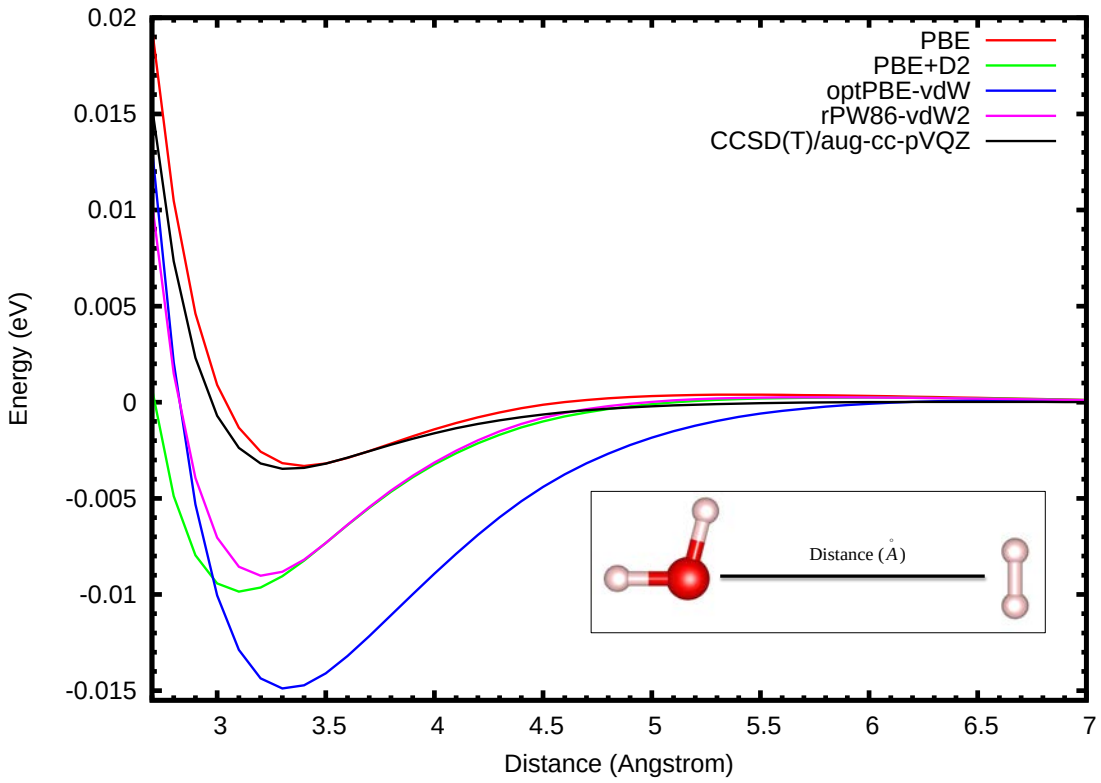

Figure 7.1 *Potential energy surface showing the interaction of a hydrogen molecule and a water molecule (geometry shown in inset) as a function of distance, comparing various density- and wavefunction-based approaches.*

7.6 Hydrogen hydrate results

7.6.1 Static

H_2-H_2O compound system

In this work, we explored the possible phases in the H_2-H_2O system via ground state energy calculations. The pressure range in this study is from 1 bar to 100 kbar. Six phases were tested. These include sII, ice-I_h, S_χ (C_0), ice-II (C_1), ice-I_c (C_2), ice-I_c (C_3). The notations in the round bracket are commonly used in the hydrogen-hydrate system to refer to the stable phases in a sequence of increasing pressure (i.e. from C_0 to C_3).

For each host water network, the energies upon varying the guest contents (filling ratios) were computed and compared. The stoichiometry study of the compounds will help us verify the experimental results, especially the hydrates based on sII structure. Various guest filling ratios were applied in order to identify the correct occupancies of the hydrogen molecules in both cavities of sII (small and large). The number of tested hydrogen molecules varies between 1-2 in small cavitiess and 1-4 in large cavities. For other host water network, different guest filling ratios were tested: one guest molecule per cavity ("fully-filled"), more than one per cavity ("overly-filled") and no filling in some cavities ("partially-filled").

rPW86-vdW2

As a representative example according to the convex hull plot (Figure 7.2) at 1 kbar, the hydrogen-water system adopts a hydrate based on fully-filled S_χ (H_2O:H_2 ratio of 2:1). A hydrate based on fully-filled Ice-I_h network (the same 2:1 H_2O:H_2 ratio) is a metastable phase and is energetically not far from the phase based on S_χ (less than 0.1 meV/entity). In fact, the phase transition between these two phases was computationally predicted to occur at a slightly higher pressure, P = 1.13 kbar. Therefore, their relative enthalpies at 1 kbar are almost identical. Another stable phase at 1 kbar is the compound based on ice II network (H_2O:H_2 ratio of 6:1). The hydrates based on sII network are meta-stable ($>$ 7 meV/entity from the tie line). The stoichiometry test based on the sII network suggests that 1 hydrogen molecule per small cage and 4 hydrogen molecules per large cage is the most stable stoichiometry among various hydrogen contents. Although, several hydrogen fillings of both small and large cages in

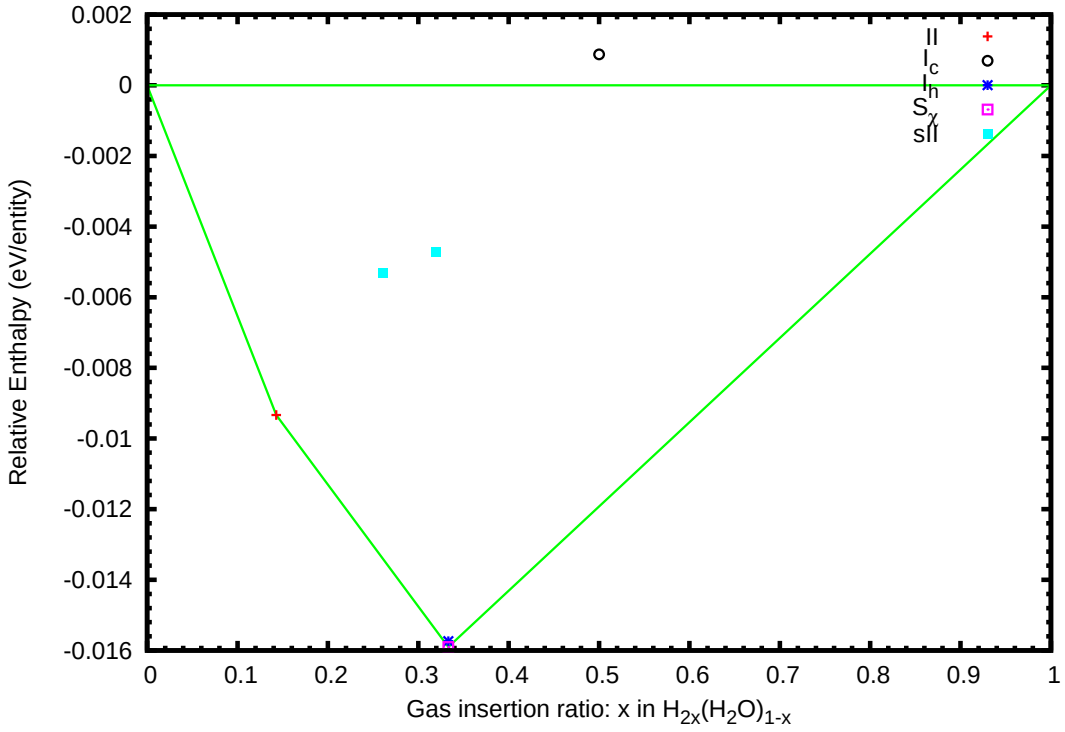

Figure 7.2 *Convex hull plot showing all the phases in this work including sII at P = 1 kbar at the rPW86-vdW2 level. The cyan points represent 1 hydrogen molecule (guest:host content 0.26) and 2 hydrogen molecules (guest:host ratio 0.32) in the small cage of the sII clathrate.*

the sII network are studied in this chapter, for clarity only 2 stoichiometries were shown in Figure 7.2. These are 1 hydrogen molecule per small cage and 2 hydrogen molecule per small cage. Both have 4 hydrogen molecules in the large cages. In Figure 7.2, the cyan point on the left (1 hydrogen per small cage) is more stable than the cyan one the the right (2 hydrogens per small cage). This result agrees with the experiments by Mao [103]. However, it is known that the hydrate based on sII structure should be found at lower pressure than the phase based on S_χ network. At rPW86-vdW2 level of theory, the result suggest its meta stability thus contradicting the experiment.

A convex hull plot is constructed in order to compare the enthalpies of the compounds having different stoichiometries but at one particular pressure. Several convex hulls were plotted (i.e. one at each calculated pressure). Each was analysed in terms of stable hydrate phases. Then, summarised results from the convex hull plots were concluded in Figure 7.3.

According to our data plotted in Figure 7.3, the S_χ hydrate is stable upto P =

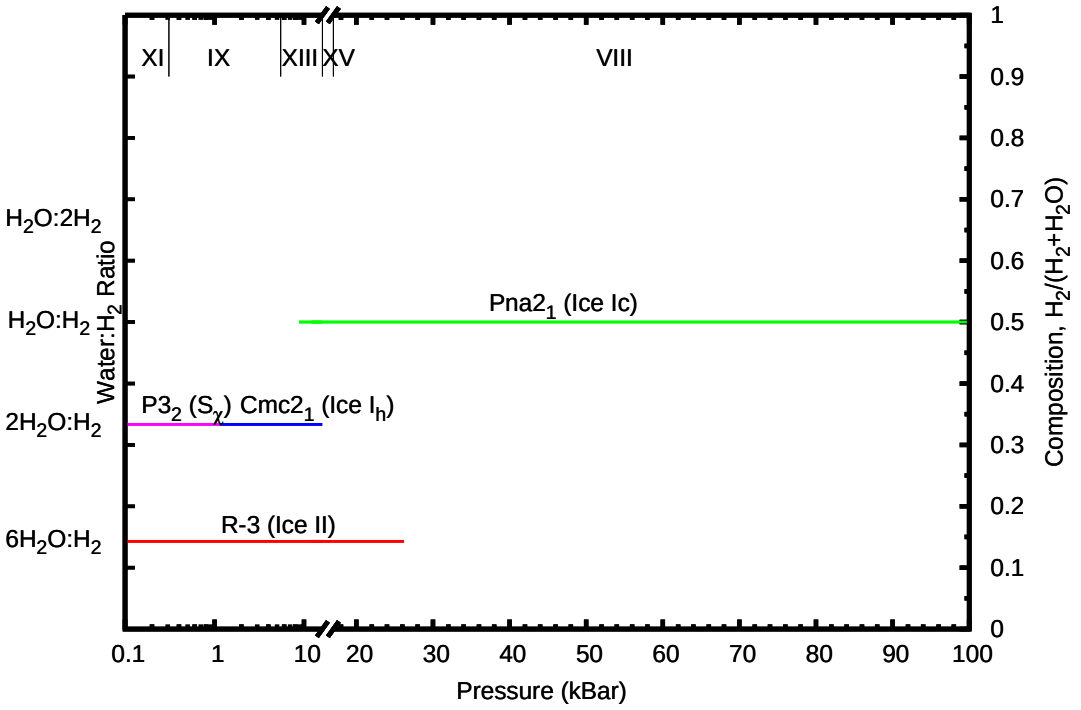

Figure 7.3 *Phase diagram of hydrogen hydrates system using rPW86-vdW2 functional.*

1.15 kbar. Fully-filled ice-I_h hydrate is stable from $P = 1.15$ kbar upto $P = 15.97$ kbar and the stability range of the fully-filled ice-II phase is from $P = 0.086$ kbar to $P = 26.23$ kbar. Finally, hydrogen hydrates adopt fully-filled ice-I_c (C_2) from $P = 8.81$ kbar to the maximum studied range $P = 100$ kbar.

Other functionals

The stability ranges as a function of pressure obtained from some selected functionals implemented in this research are shown in Figure 7.4 and listed in Table 7.3. All functionals indicate that hydrogen hydrates do not adopt sII host water network, although the phase based on sII structure is metastable (i.e. stable against decomposition into water ice and solid hydrogen). However, the results suggested similar trends of phase stability although having different stability range among various functional applied. All the vdW-DF family also have similar results. This might be due to similar pair-wise interactions (equilibrium distance and binding energy), as described in section 7.5.

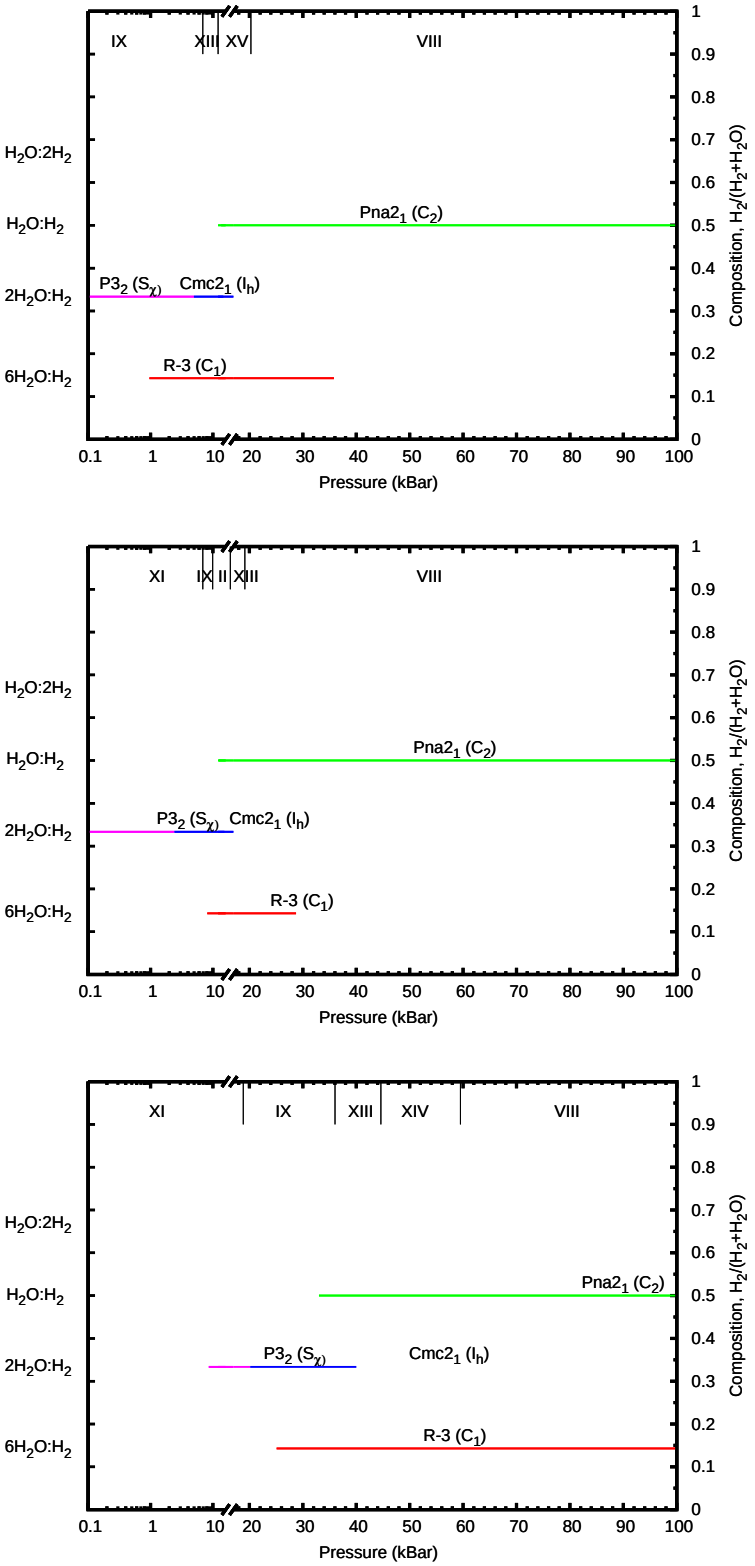

Figure 7.4 *Stability ranges as a function of pressure of the ground state phases in the H_2-H_2O system, using optPBE-vdW (top), PBE+D2 (middle), PBE (bottom). Information about the host spacegroups following by their water networks' name listed in brackets are indicated above the stability ranges. The upper line on each graph shows stability of the ice phases.*

Methods	S_χ (C_0)	ice-I_h	ice-II (C_1)	ice-I_c (C_2)
rPW86-vdW2	0.001-1.15	1.15 - 15.97	0.086 - 26.23	8.81 - 100
optPBE-vdW	0.001-4.96	4.96 - 14.67	0.96 - 35.83	13.59 - 100
optB88-vdW	0.001-2.32	2.32 - 19.48	0.001 - 30.87	11.80 - 100
optB86b-vdW	0.001-5.25	5.25 - 15.42	0.98 - 34.54	12.39 - 100
PBE+D2	0.001 - 2.42	2.42 - 15.26	8.12 - 28.73	12.45 - 100
PBE	8.59 - 20.14	20.14 - 40.02	25.21 - 100	33.02 - 100

Table 7.3 *Stability ranges in the H_2-H_2O system as a function of pressure (unit is in kbar) in different host water networks having fully-filled guest occupancy, using a sequence of functionals given in the first column.*

7.6.2 Dynamics

At low pressure (around 1 kbar), three competitive phases based on S_χ, ice-I_h and ice-II are found to be stable in the hydrogen-water compound (see Figure 7.3). In this subsection, these three competing host water networks are chosen to be studied further regarding their dynamics, i.e. the energy barriers required by the hydrogen guest molecules if such hydrogen molecules are permitted to move along certain pathways. As there are several pathways, this research filters out the unlikely choices by considering the pathways containing the largest open space only.

Nudged Elastic Band (NEB) Theory [47] is used to compute the energy barrier for the hydrogen molecules moving along the pathway. The idea of the NEB theory is to connect all the replica (images) of hydrogen molecules' configurations by some forces (i.e. spring forces). These forces connect all the images together so that they restricted the movements of hydrogens to only certain directions along the pathway. Twelve images of linearly displaced hydrogens are initially produced to represent the initial coordinates of hydrogen along the pathway. Calculations in this subsection are performed at rPW86-vdW2 level of theory.

S_χ host water network

The S_χ host water Previously was computationally found to be (meta)stable in some of the noble gas hydrates [153], stable in the hydrogen hydrates [3, 125]. Thus, the dynamics of the S_χ host water network is carefully analysed. This includes the energy-barrier calculations for H_2 diffusion along the channel.

Figure 7.5 illustrates the initial setup providing the coordinated motion of an entire H_2 chain along the pathway in the channel in the S_χ structure. Results

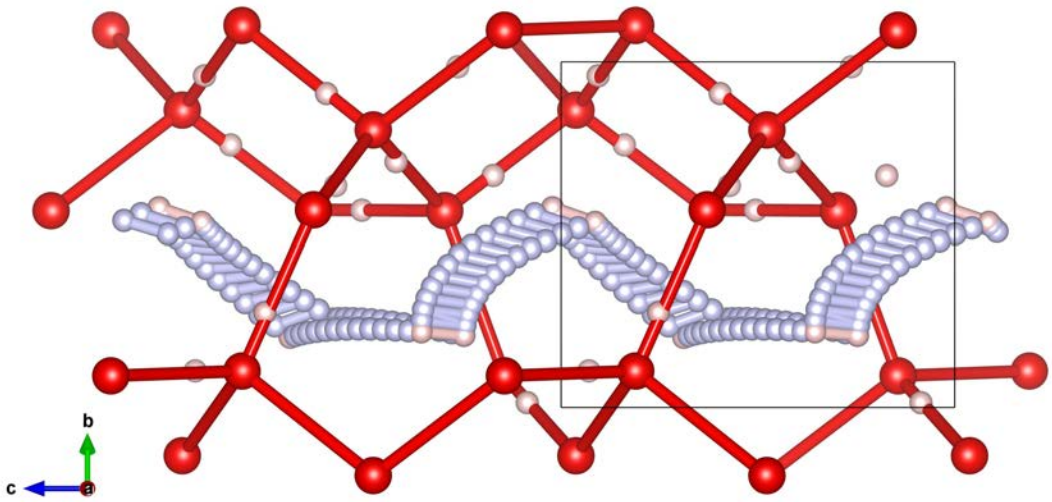

Figure 7.5 *An overlay of all initial H_2 positions along the channel of the S_χ host water network used for the NEB calculations, created by a linear interpolation between the guest sites.*

from NEB calculations based on these initial hydrogens' positions are shown in Figure 7.6. Relaxing the energetic pathway by the NEB method helps finding the energy barrier of hydrogen molecules if they are allowed to hop from one local minima to the next adjacent one. The NEB results turn out to be 80 meV/cell at 1 kbar (or 26 meV/hydrogen molecule) for the fully-filled hydrate.

The energy barrier is slightly reduced upon increasing pressure, i.e. to 72 meV/cell (24 meV/hydrogen molecule) at 10 kbar. In summary, as pressure increases, the energy barrier required for concerted diffusion of an entire chain of hydrogen molecules to move along the channel provided by the S_χ host water network gradually reduces in the range of 1-2 meV/hydrogen molecule.

Ice-II host water network

The energy barrier of the hydrogen hydrates based on ice-II host water network is calculated by NEB method. In this system in the conventional unit cell, there are 6 hydrogen molecules located along 3 channels along z-axis (Figure 7.7). By focusing on the hydrogens' movement along 1 channel (2 hydrogen molecules per channel), the energy required for those two hydrogens to move along the channel was calculated. At rPW86-vdW2 level of theory, the results indicate that 0.337 eV/cell (or 168 meV/hydrogen molecule) is required at 1 kbar in order to move all hydrogens along one channel in the z-axis. As pressure increases, a slightly larger amount of energy is needed to overcome the energy barrier (Figure 7.8).

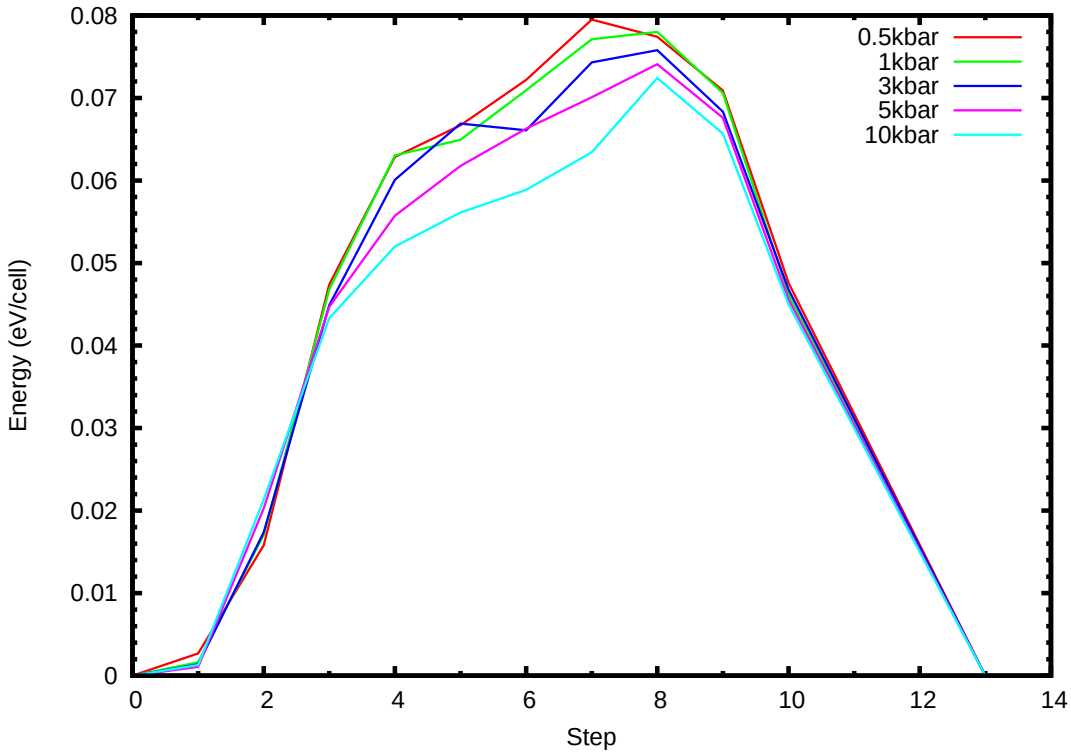

Figure 7.6 *NEB calculations showing energies required for hydrogen molecules to move along the channel in a fully-filled C_0 hydrate under various pressures.*

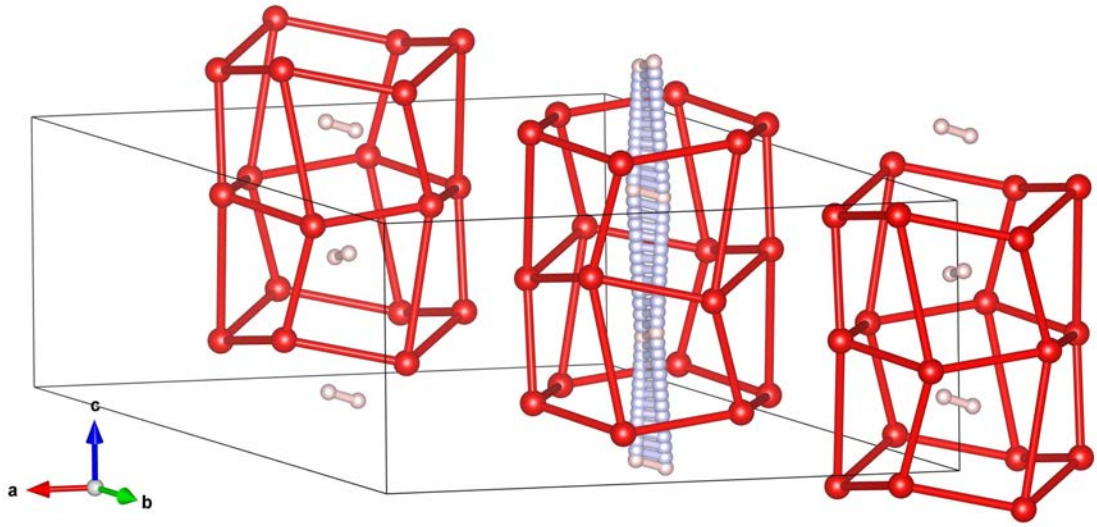

Figure 7.7 *A picture of an overlay of initial hydrogen positions along [001] direction of the ice-II hydrate used for NEB calculations. Waters' protons are omitted for clarity.*

This upward trend is in contrast to the reduction of the energy barrier required to move the guest hydrogen molecules in S_χ network.

Ice-I_h host water network

Both Ice-I_h and S_χ have the same stoichiometries when fully-filled with hydrogen molecules. Thus, it is worthwhile to study the energy barrier required for hydrogen molecules to hop from one site to the adjacent position in this network. Additionally, both two phases are competitive at low pressure. In this research, three different models illustrating diffusion of hydrogen molecules in the ice-I_h network are studied. The first model considered the hydrogen molecules moving along zigzag channel (i.e. in the a-b plane along the [010] direction. The second model focuses the hydrogen molecules along a straight channel (along the [110] direction in the a-b plane). The third model studies the movement of hydrogen molecules in a straight channel along c axis (along [001] direction). Those three models are illustrated graphically in Figure 7.9 in respective order.

Results of the energy barriers required by the hydrogen molecules in order to move along three different models (channels) are plotted in Figure 7.10. According to the results, the channel along [001] direction has the smallest energy barrier (i.e. 0.213 eV/cell or 107 meV/hydrogen molecule at 1kbar), followed by the zigzag channel along the [010] direction (i.e. 0.320 eV/cell or 160 meV/hydrogen molecule at 1 kbar). The straight channel along the [110] direction has the highest energy barrier (i.e. 0.595 eV/cell or 297 meV/hydrogen molecule at 1 kbar). As

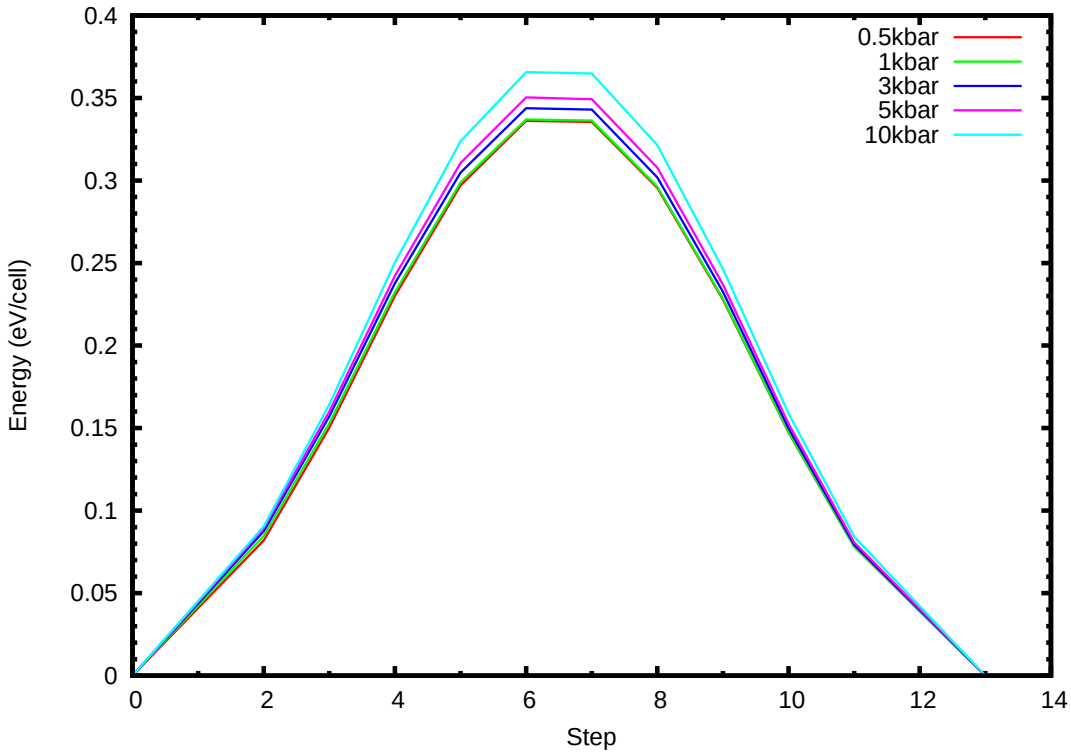

Figure 7.8 *Energies required for hydrogen molecules to move along the channel along [001] direction at various pressures. Calculations were performed based on the fully-filled ice-II host water structure.*

pressure increases, the energy barriers are slightly elevated. However, the channel along c axis always has the smallest energy barrier among the three.

Comparison of the energy barriers among three host water networks

Energy barriers for all three host water networks (S_χ , ice-II, and ice-I_h) are shown in Figure 7.11. The amount of energy required to move hydrogen molecules in the ice-I_h and ice-II network are about 4-6 times higher than in the S_χ network. This suggests the guest hydrogen molecules are more localised in the ice-II and ice-I_h and significantly more mobile in S_χ. Additionally, the energy barrier is about the room temperature contribution's effect (25 meV). Thus, the hydrogen molecules in the S_χ are expected to be even more mobile at higher temperature if having vacancy defects in the system. The high mobility of the guest hydrogen molecules in the S_χ is also experimentally been confirmed [3].

7.7 Pressure-volume curve

Similar to the study in chapter 6, we performed the pressure-volume studies in order to see the effects upon encapsulation process. In the previous chapter, we found the volume expansion of filled hydrates compared to their empty host networks in both helium and neon guest gases. However, sII clathrate was not included in the previous study. Neutron diffraction studies of neon hydrates based on sII suggested the unit cell shrinkage in the presence of guest species [41]. Thus, in the hydrogen hydrate system, we included the sII as the host structure since we have already performed the structural relaxations based on the sII clathrate.

According to Figure 7.12, the fully-filled hydrates based on pure ice structures (solid lines) always have larger volume than their empty host water networks (dashed lines). Ice-II based hydrate has slightly expansion with the hydrogen guest molecules; whereas the ice-I_c based hydrates has the largest difference between the fully-filled- and empty- hydrates. This is due to the ice-II has larger cavity sizes than the ice-I_c (the cavity size of ice-I_h is also larger than ice-I_c). These expansions in volume in the hydrates based on pure ice structures are in constrast to the sII hydrates (shown in solid brown colour), which has a decrease in volume compared to the empty sII clathrate. This shrinkage of volume in the sII hydrates (volume shrinkage of 3.3% in the H_2 hydrate system) is similar to those found experimentally in the neon hydrate system, with 0.4% volume

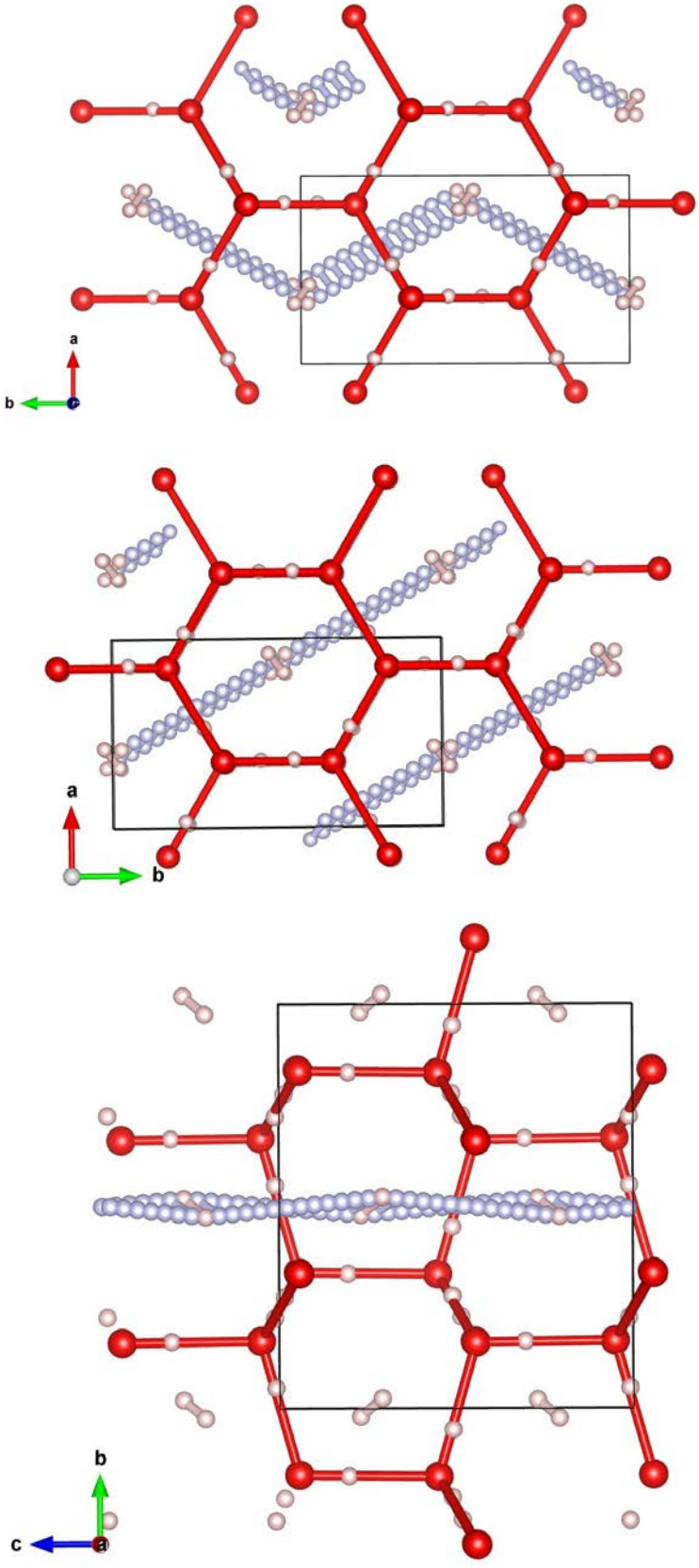

Figure 7.9 *Initial models of hydrogen molecules' displacements in the ice-I_h network along the [010] (top), [110] (middle), [001] (bottom) directions.*

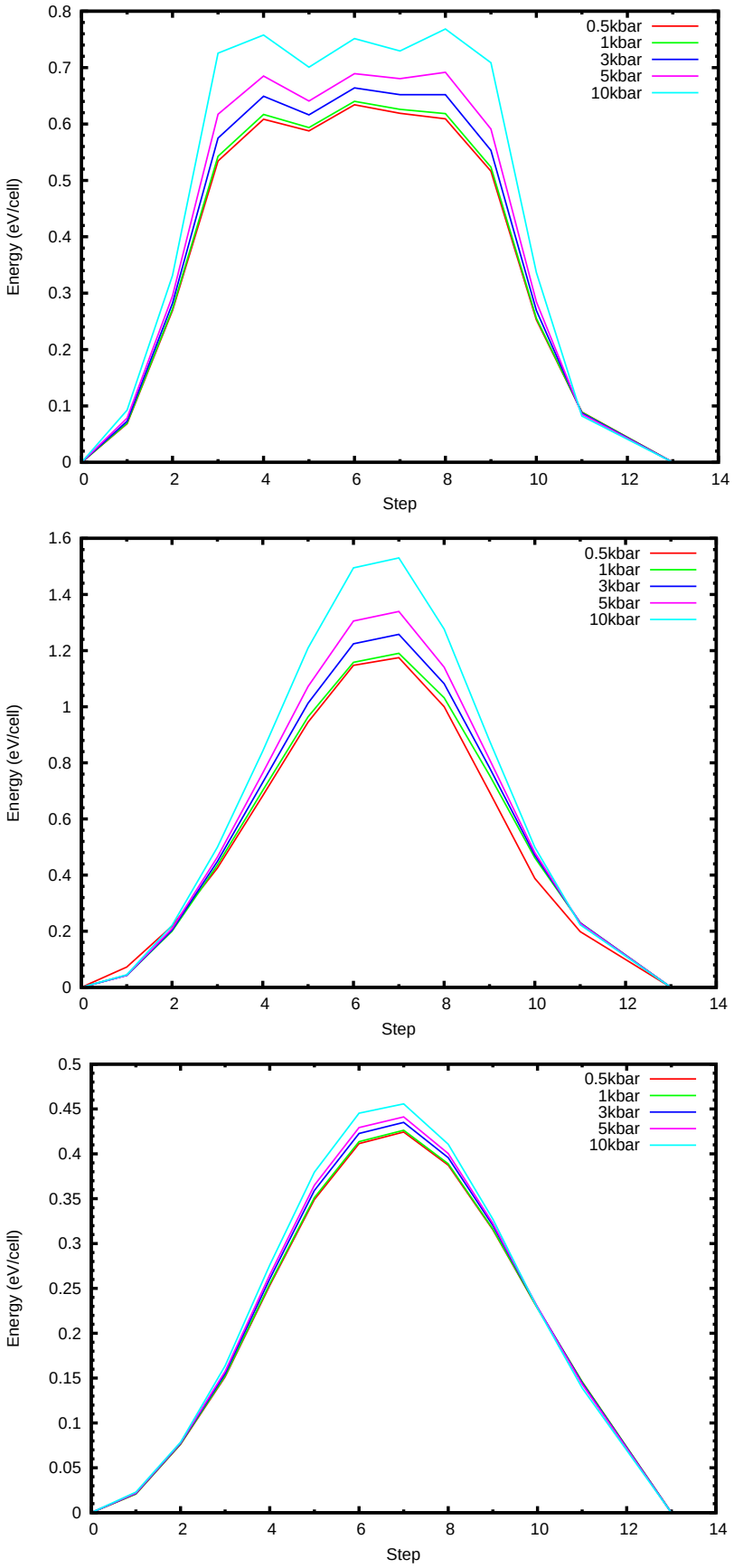

Figure 7.10 *Energy barriers as a function of pressure of the hydrogen molecules in the ice-I_h network along the [010] (top), [110] (middle), and [001] (bottom) direction.*

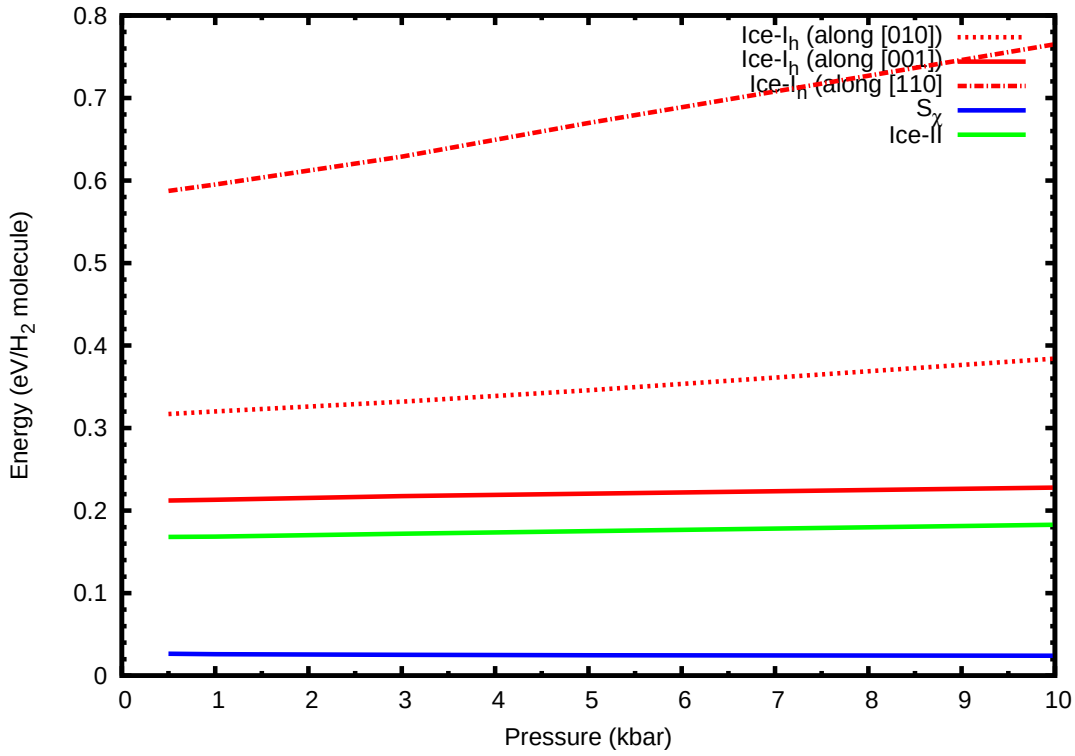

Figure 7.11 *Energy barriers for H_2 diffusion as a function of pressure calculated by NEB approach for fully-filled hydrates with the ice-I_h (red), ice-II (green) and S_χ (blue) host water network.*

reduction [41].

7.8 Discussion

According to the computationally predicted stability ranges obtained by various DFT functionals in this research listed in Table 7.3, all the functionals can predict phase sequences similar to those found experimentally, i.e. $S_\chi \rightarrow$ ice-II $\rightarrow$ ice-I_c, except only for the sII phase. Although the stability pressure ranges differ among functionals, the predicted stable pressure for each hydrate is within or close to the experiments. For example, the experimentally known stability pressure for S_χ host water network is P = 0.5 GPa (rPW86-vdW2 functional predicted to be stable from P = 1 bar to 0.1 GPa). The predicted stability range varies among the functionals used, i.e. from P = 1 bar to 0.5 GPa for optPBE-vdW, P = 1bar to 0.23 GPa for optB88-vdW, P =1 bar to 0.53 GPa for optB86b-vdW, P = 1 bar to 0.24 GPa for PBE+D2, and P = 0.86 GPa to 2.01 GPa for PBE functional.

It is worth mentioning that there is no experimentally stable phase based on ice-I_h hydrate; however, our computations predict its stability. Thus, the predicted pressure range of the hydrogen hydrates based on S_χ structure would be extended if omitting the ice-I_h hydrates.

For the phase adopting ice-II host water network, experiments suggest its existence in the pressure between 0.75 - 3.1 GPa, which is in the stability range obtained by all functionals in this chapter. Especially, all the vdW-corrected functionals propose the stability pressure up to around 2.6 - 3.6 GPa. For the ice-I_c host water network, pressure above 4.6 GPa is suggested, which is also in the predicted pressure ranges of all functionals. Note that we predicted quite broad stability range; whereas narrower stability ranges are reported in experiments. This might be due to our calculations which are performed at 0 K in contrast to at a specific temperature. However, the predicted stability range of the hydrogen hydrate system would provide insightful data on which phase sequence and at what pressure the new hydrates might be found.

The ranges of stable pressure obtained by the functionals in the vdW-DF family are almost identical. This suggest there is not so much difference among the results calculated via any of the vdW-DF functionals in this hydrogen hydrate compound systems. The semi-empirical vdW-D2 also predicted valid stability

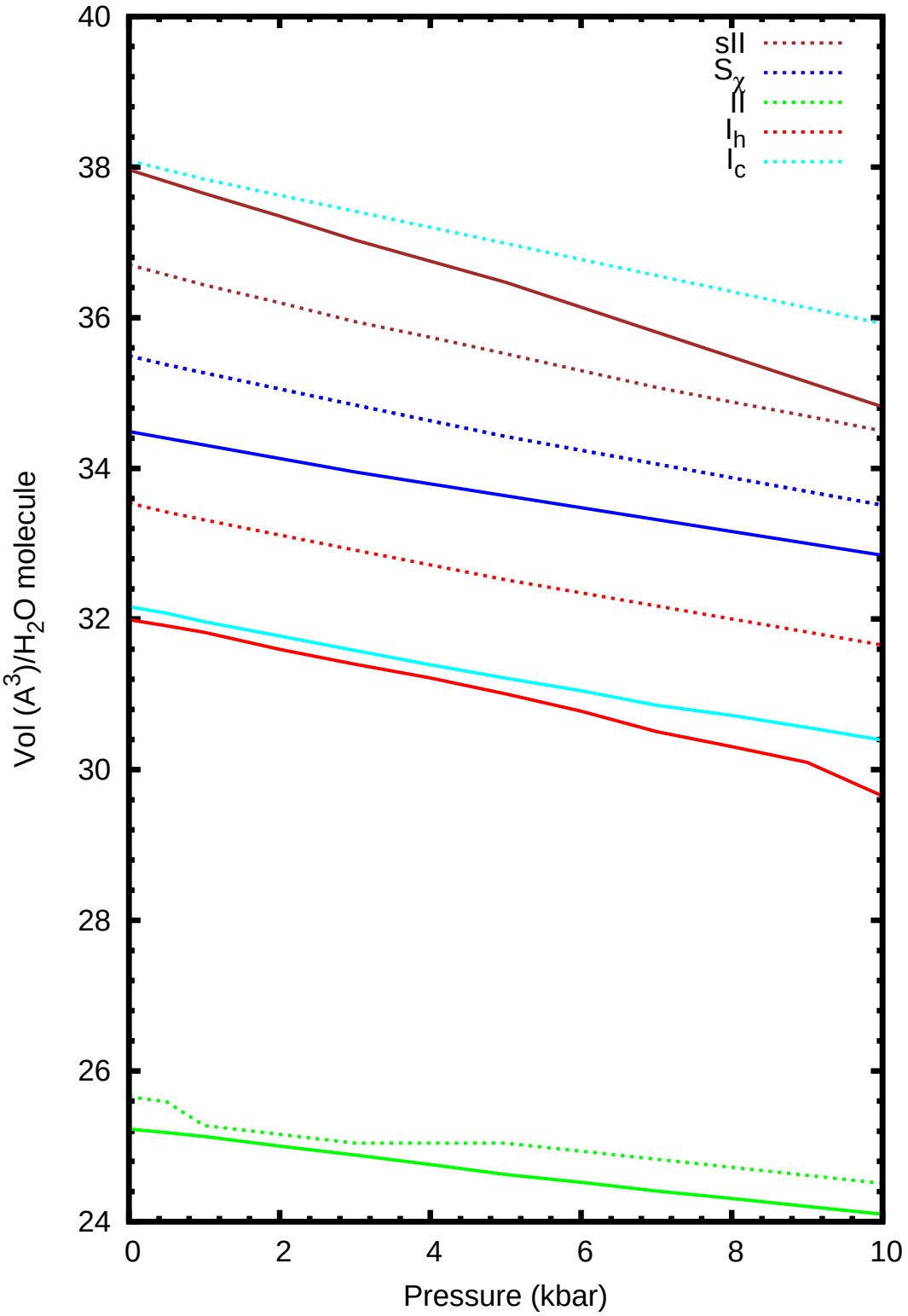

Figure 7.12 *Pressure vs volume plots of pure host water networks (solid lines) and the hydrogen hydrates based on those host structures (dashed lines). Calculations were performed at rPW86-vdW2 level of theory.*

pressure for most of the phases, although having wider stability pressure range than those found experimentally. Alghough the semi-localPBE functional could provide the same phase sequence, the stability range predicted by PBE deviated most from the experimental results. This suggests the significance of vdW-corrected functionals in DFT calculations in the gas hydrates.

We obtained a similar phase diagram as proposed by Qian [125], except for the C_3, which is out of range from our studied pressure. This confirms the validity of Qian's results.

The sII clathrate hydrate phase was also found to be metastable with all functionals employed in this research. Varying the guest hydrogen content does not help shifting this sII phase from the metastability region to the stable one. Energetic difference from various proton configurations in the sII hydrate was not that much to help it become stable either. The energy difference between the sII base structure and the more stable phases are about 7-8 meV/entity, which is a relatively considerable amount. Although there are several ways of arranging protons in the sII host water network, the test based on pure ices upon assigning those hydrogens yield only 3 meV/entity. Thus, the assumption of not having suitable hydrogen configurations is insufficient to explain the metastabliity of the sII base hydrates. Dispersion effects have also been tested to figure out the discrepancy. The results show that no stable phases based on sII are found with any DFT functionals used. The reason why the sII structure is calculated to be metastable in the phase with respect to the other host water networks but found experimentally at low pressure might be due to its dynamics and entropic mechanism. Since this study was focused only at zero temperature but in reality the sII phase is studied around 70-100 K, the temperature effect might influence the entropic behaviour to stabilize the sII network.

Dynamics studies suggest that the guest hydrogen molecules are much more mobile in the S_χ than both the ice-I_h and ice-II host water networks. There are also opposite trends of the energy barriers found among the three host networks. While the energy barriers increase in both the ice-I_h and ice-II host water networks as pressure elevates, slight decrease of the energy barrier is found in the S_χ network.

Additionally, the energy barrier is about the room temperature contribution in C_0 suggesting the possibility of hydrogen's mobilisation along the channel at moderate temperature if having vacancy defects.

As expected, the transition states in pure water ice models are situated when the hydrogen guest molecules are at the middle of a plane formed by six water molecules. Those six water molecules can be viewed as a face of a polyhedron forming a cavity encapsulating a guest molecule. Two adjacent polyhedrons are connected by this six water ring. Thus, the guest has to transport through this ring in order to move to the next cavity site.

Note that the S_χ network differ from other filled ice networks in the sense that the water molecules form spiral cages providing larger space than those in filled ice structures. This helps the guest species to easily move along the channel than the tightly limited space in the filled networks. This is also true for the guest diffusion in clathrates. However, there usually will be more than one guest molecule per cage in those clathrate structures and there are a large number of pathways which need to be considered. The energy barriers in the clathrate were excluded from this work.

For the ice-I_h, three different pathways are considered namely along [010], [110], and [001] direction. The NEB result along the [010] direction (see Figure 7.11) shows that in step 4 and 8 one hydrogen molecule is located at the middle of the ring while the other one is at the middle of the cage. While in step number 5-7, two hydrogen molecules are situated at the same cage. This suggests a step-wise process along the [010] direction instead of those concerted motions found along the [110] and [001] directions.

Of all three models in the ice-I_h network, the model having the pathway along [001] direction has the lowest energy barrier because of more space for the guest hydrogen molecule to move in the pathway along [001] compared to the other two. In both [010] and [110] pathways, their energy barriers significantly increase. This is also due to the setup having only one unit cell and having the cell volume fixed. Such restrictions limit the expansion of the O-O bond lengths of the nearby water molecules (i.e. forming cages encapsulated the guest hydrogen inside) if the guest hydrogen molecules were to pass through to the adjacent cage. Periodic boundary condition also restricts the calculations performed in one unit cell because there is quite limited adjustable space for the water molecules to relax. Hence, the energy barrier obtained by using one unit cell might be overestimated than those calculations in larger cell size.

7.9 Conclusions

In summary, a comprehensive study of the ground state phase diagrams of hydrogen-water compounds based on first-principles calculations of various filled-ice structures has been presented. Calculations, which determine stable phases for the hydrogen compound system based on five distinct host water networks, namely clathrate structure II (sII), ices I_h, II, and I_c, as well as the new S_χ water network, were also demonstrated. The predicted sequence of stable hydrogen-water compounds compares very well to the stable structures found in the helium and neon-water system: stable phases based on the host water networks of the novel clathrate S_χ, ice I_h, II, and I_c were found, in that order, upon increasing pressure. At low pressure, the sII base host water network is found to be metastable independent of the dispersion functional used. Dynamics studies of hydrogen diffusions along the empty channels suggest that the S_χ host water network has the lowest energy barrier among the three host water structures (S_χ, ice I_h and ice II).

Chapter 8

Conclusions

In chapter 5, the effects of proton configurations in pure water ice structures were explored. Both "exhaustive tree-based search with backtracking" and "graph invariant topology" methods were used in order to assign protons to the experimentally known oxygen lattices of several host water networks to construct different proton configurations in those structures. The study of the effects of different proton configurations in pure water ice structures has two main benefits.

First, it helps constructing complete proton-ordered host water networks for the calculations used in gas hydrate systems in later chapters. Regarding computational study, exact protons' positions must be known in order to compute their electronic contributions. However, there are some limitations in resolving the exact hydrogen positions in experiments because a hydrogen atom is so light causing a difficulty in getting its scattering if using the XRD technique. Additionally, neutron diffraction studies often provide hydrogens' positions in terms of partial occupancies. Therefore, producing such complete proton networks in ice structures is worthwhile as it helps experimentalists solve the incomplete/missing protons' positions.

Second, the examination of the effect of different proton configurations in pure ice structures also helps us crudely approximate such effect in the gas hydrate systems. To save computational resources, we only take a few structures of the host water networks, the structures having the lowest enthalpy and the next lowest, as a representative for the host water networks in the gas hydrate systems studied later.

The enthalpy spreads between the structures having the highest and the lowest enthalpy among various ice networks usually vary in the order of 0.5 meV to 4 meV per water molecule, which is about the same order in other research [69]. However, unlike other host water networks, ice-II has the enthalpy spread of 25 meV. The structure having the lowest enthalpy is the experimentally found structure. This significant spread of the enthalpy in the ice-II network might inform us as to why we only find ice-II in proton-ordered structure.

Pressure effect on the enthalpy spread is also trivial. The energy gaps between the structures having the highest and the lowest enthalpy are almost constant (i.e. independent of applied pressure).

In chapter 6, we proposed the phase diagrams of noble gas hydrates (He, Ne, and Ar). The relative enthalpies as a function of pressure can be calculated by adopting both experimentally discovered and theoretically proposed host water networks in these gas hydrate systems, plus the host water structures observed in other gas hydrate systems which have a similar guest size. (i.e. He, Ne and H_2),

Convex hulls are used to help us visualize the stability of the compounds at a specific pressure. By constructing several convex hull plots at various studied pressures, we can produce phase diagram plots of the noble gas hydrates.

In He-H_2O system, the predicted phase evolution agrees very well with the stable structures found in the H_2-H_2O system, i.e. stable phases based on ice-I_h, ice-II, ice-I_c host water networks, upon increasing pressure.

In Ne-H_2O system, the recently discovered host water network S_χ was predicted at low pressure. That said, this proposed phase based on the S_χ is functional dependent. Our results provide compelling evidence for experimentalists in investigating neon hydrates based on the S_χ structure.

In Ar-H_2O system, we found that none of the host water networks based on pure ice structures are stable in this system. This might be due to argon being too big to fit into the space provided by those pure ice networks. The only stable phase is based on partially-filled (2/3 filling ratio) S_χ structure. However, this S_χ phase is metastable if compare to the traditional clathrate I (sI) and II (sII).

We also tested and compared the dispersion effects using different methods. Dimers' interaction energy calculations suggested that the DFT dispersion-

corrected functionals tend to have significant overbinding energy compared to results from the CCSD(T) method. However, these overbinding effects are less pronounce in cluster calculations. This suggests that the overbinding effect caused in DFT functionals might be even less in extended systems.

Crudely approximations to the DFT results based on the difference of CCSD(T) and DFT's pair-wise interactions have been proposed. Such corrections yield us new phase diagrams. Although the corrections are not accurate, these approximations could provide an upper bound for the binding energies of the hydrates. Other metods with specialized treatment of the weak host-guest interactions are required.

In chapter 7, hydrogen hydrates were explored. Phase diagram studies on this gas hydrate system have been computed with various functionals and compared with both experimentally known and theoretically proposed phase diagrams. Our results agree very well with both of these. However, the phase sequence of the hydrogen hydrates depends on the functional used. Qualitatively, different functionals can predict the same phase sequences. However, the range of phase stability and the phase transition pressure are quantitatively different among functionals. This functional dependent effect is also observed in noble gas hydrate system.

Unlike the experimental studies, the hydrogen hydrates based on sII networks was found to be metastable. This suggests that other effect besides the proton configuration effect should be taken into account. These include zero-point energy calculations or finite temperature effect.

Dynamic studies of hydrogen diffusions in different host water networks were also conducted. Although, only selected possible pathways were used in the computations, the results are fruitful in providing estimated energies if moving hydrogens along these paths. Computational results suggested the guest hydrogen molecules are more localised in both ice-II and ice-I_h than found in S_χ. In the S_χ phase, hydrogen molecules are likely to have high mobility. This finding is also consistent with the experiments [3].

We also tested the pressure-volume curves in both noble gas and hydrogen hydrate systems, and the results in both systems are virtually identical. Results suggested the volume expansion of filled hydrates compared to empty hydrates are found in most water networks, except only in the sII. In the sII host water network, the shrinkage of volume upon adding the hydrogen guest molecules are found. This

finding is analogous to the experimental result, which found a decrease in volume of the filled sII clathrate compared to the empty one [41].

In addition to the studies in this thesis, there are some possibilities for future research. Two approaches can be envisaged. First, similar calculations used in this thesis can be applied to explore other gas hydrate systems. We have presented the ground state enthalpy calculations based on different host water networks to predict the phase diagrams in noble gas hydrates and hydrogen hydrates. The same method can be applied to oxygen hydrates as well. In oxygen hydrates, there are still unclear stoichiometries of the guest oxygen molecules in sII clathrate [159]. Thus, we can compute the enthalpies of the structure having various stoichiometries to figure out how many oxygen molecules are in both large and small cages of the sII hydrate. Moreover, argon and oxygen have size similarity. Results from argon hydrates study might be able to apply or compare to the results from oxygen hydrate systems because the oxygen hydrate based on sII structure is the only phase found in experiments so far.

Mixed hydrate systems can also be explored. Some host water networks have found to be host water structures for several guest species. For example, H_2 and CO_2 have found to adopt S_χ host water network, helium and neon are found in ice-II structure. Thus, such binary compound studies are compelling, and of course, the same methods of computing their ground state enthalpies can be applied.

Second, we can implement different methods to the same systems studied before. All of the calculations in this thesis were performed at zero kelvin temperature. Finite temperature calculations would provide invaluable data representing the actual experimental parameters. Zero-point energy effects and also finite temperature entropies can be calculated using phonon calculations. Those corrections will then change the enthalpies in this thesis into Gibbs' free energies, which are more related to experimental results.

Moreover, we can perform molecular dynamics (MD) calculations to obtain the structural information and phase transition points as functions of pressure and temperature. Classical MD, although it is inexpensive, is often inaccurate because it omits the quantum effects in bond breaking and charge transfering. Additionally, the force field implemented in the classical MD is often not suitable for the calculations of materials under pressure. Quantum-mechanical (QM) MD can be tested and compared to the results from the classical MD simulations.

These may provide insight into the requirement of more accurate but expensive QM MD method in the gas hydrate system. If the classical MD calculation is sufficient, then it will save lots of computational resources.

Appendix A

List of Publications

[1] Teeratchanan, P., and Hermann, A. "Computational phase diagrams of noble gas hydrates under pressure" *J. Phys. Chem.* **143**, 154407 (2015).

[2]. Amos, D.M., Donnelly, M.E., Teeratchanan, P. Bull, C.L., Falenty A., Kuhs, W.F., Hermann, A., and Loveday J.S. "A Chiral GasHydrate Structure Common to the Carbon Dioxide Water and HydrogenWater Systems" *Phys. Chem. Lett.* **8**, 4295-4299 (2017).

Appendix B

Atomic coordinates

This appendix contains atomic coordinates of selective stable water ice structures and the gas-water compounds used in the calculations. Each structure's atomic coordinate (relaxed with DFT + rPW86-vdW2 or optPBE-vdW functional at the pressure stated in the bracket, 0 K) is listed in Table I (for pure ices), Table II (for He hydrates), Table III (for Ne hydrates), Table IV (for Ar hydrates), Table V (for H_2 hydrates).

- All atomic coordinates are given in crystal lattice unit.

- Three lattice parameters are given in the unit of Å.

Phase (Pressure)	Space group # H_2O Molecules	Lattice parameters (Å, °)	Atomic coordinates (fractional)	
I_h	$Cmc2_1$	a=4.351, b= 7.567, c= 7.108	O1	0.0000 0.6662 0.0593
(Ferroelectric)	8	α=β=γ = 90	O2	0.0000 0.3336 -0.0652
(1 bar)			H1	0.0000 0.6646 0.2007
			H2	0.0000 0.5394 0.0173
			H3	0.1848 0.2680 -0.0170
I_h	$Pna2_1$	a=7.167, b= 7.547, c= 4.435	O1	0.0621 0.4176 0.0091
(Antiferroelectric)	8	α=β=γ = 90	O2	0.0630 -0.0817 0.4907
(1 bar)			H1	0.5168 0.5257 0.3006
			H2	0.7984 0.5801 0.5070
			H3	0.4858 0.2942 -0.0063
			H4	0.5210 0.0228 0.1989
I_c	$I4_1md$	a=b= 4.356, c= 6.178	O1	0.0000 0.0000 0.7537
(1 bar)	8	α=β=γ = 90	H1	0.0000 0.3154 -0.0940
IX	$P4_12_12$	a=b= 6.53423, c= 6.96480	O1	0.61425 0.81147 0.26965
(1bar)	8	α=β=γ = 90	O2	-0.10000 -0.10000 0.00000
			H1	0.48964 0.84249 0.19166
			H2	0.61509 0.65934 0.28350
			H3	0.80296 0.86483 0.10615
XIII	$P2_1/a$	a=9.03942, b= 7.37225, c= 10.10014	O1	0.25763 0.05993 0.25460
(1bar)	28	α=γ= 90, β= 109.33478	O2	0.46645 0.30350 0.40291
			O3	0.05698 0.31045 0.09665
			O4	0.27137 -0.09897 0.50146
			O5	0.20410 -0.09755 0.00123
			O6	0.41550 0.60847 0.23505
			O7	0.12281 0.61051 0.26630
			H1	0.34537 0.14612 0.29961
			H2	0.24800 -0.00856 0.33640
			H3	0.11908 0.21511 0.16158
			H4	0.47212 0.41442 0.34903
			H5	0.57316 0.24958 0.44297
			H6	-0.04562 0.25100 0.04887
			H7	0.23392 -0.04706 0.09802
			H8	0.31383 -0.00839 0.57854
			H9	0.17431 0.85721 0.51666
			H10	0.30232 0.86472 -0.01485
			H11	0.07691 0.51253 0.19732
			H12	0.31502 0.63869 0.24982
			H13	0.37973 0.54872 0.14114
			H14	0.04295 0.70846 0.25115
II	$R\bar{3}$	a=b= 12.624, c= 6.167	O1	0.8077 0.0289 0.0486
(5 kbar)	12	α=β= 90, γ = 120	O2	0.1441 0.4379 0.1903
			H1	0.4683 0.2852 0.3250
			H2	0.7860 0.0090 0.2040
			H3	0.2243 0.7699 0.1845
			H4	0.2662 -0.0953 0.1064
XIV	$P2_12_12_1$	a=8.195, b= 8.150, c= 3.950	O1	-0.0049 0.2517 0.1243
(10 kbar)	12	α=β=γ = 90	O2	0.3628 0.5040 0.2456
			O3	0.2541 0.8878 -0.0057
			H1	-0.0965 0.2920 0.2665
			H2	-0.0506 0.1616 -0.0166
			H3	0.2816 0.4736 0.4217
			H4	0.4262 0.5932 0.3578
			H5	0.3489 0.8292 0.8930
			H6	0.2258 -0.0309 0.8151

Phase (Pressure)	Space group # H_2O Molecules	Lattice parameters (Å, °)	Atomic coordinates (fractional)	
XV	$P\bar{1}$	a= 5.723, b= 6.127, c= 6.129	O1	0.2399 0.7553 0.2498
(10 kbar)	10	α= 89.337, β= 89.676,	O2	0.6171 0.4817 0.2443
		γ = 89.87	O3	0.6255 0.0341 0.2537
			O4	0.8633 0.7556 -0.0303
			O5	0.8551 0.7477 0.5229
			H1	0.0130 0.7503 0.4561
			H2	0.0147 0.7555 0.0484
			H3	0.3519 0.6309 0.2463
			H4	0.3469 0.8821 0.2497
			H5	0.6253 0.3197 0.2543
			H6	0.8716 0.7472 0.6844
			H7	0.7001 0.5420 0.3716
			H8	0.7017 -0.0442 0.3776
			H9	0.7052 -0.0338 0.1273
			H10	0.7745 0.6356 0.0425
VIII	$I4_1amd$	a=b= 4.758, c= 6.869	O1	0.0000 0.2500 0.6091
(30 kbar)	8	α=β=γ = 90	H1	0.0000 0.0851 0.6963

Table B.1 *Lattice parameters of pure ice structures (given in Å) relaxed with optPBE-vdW functional at stable pressure shown in the bracket and T=0 K.*

Phase (Pressure)	Space group # H_2O molecules : # He atoms	Lattice parameters (Å, °)	Atomic coordinates (fractional)	
I_h	$Pna2_1$	a= 7.025, b= 7.771, c= 4.519	O1	0.5564 0.4160 -0.0047
(1bar)	8 : 4	α=β=γ= 90	O2	0.5576 -0.0818 0.5048
			H1	0.0134 0.5255 0.3187
			H2	0.3014 0.5826 0.5002
			H3	-0.0122 0.2965 -0.0014
			H4	0.0152 0.0238 0.1796
			He1	0.7447 0.2511 0.5018
I_h	$Cmc2_1$	a= 4.485, b= 7.816, c= 7.019	O1	0.0000 0.6688 0.0529
(1bar)	8 : 4	α=β=γ = 90	O2	0.0000 0.3365 -0.0609
			H1	0.0000 0.6662 0.1952
			H2	0.0000 0.5465 0.0125
			H3	0.1786 0.2718 -0.0161
			He1	0.0000 0.0003 0.7555
C_1	$R\bar{3}$	a=b= 12.613, c= 5.999	O1	0.2219 0.1951 0.0479
(10 kbar)	36 : 6	α=β = 90, γ = 120	O2	0.5232 0.8973 0.1482
			H1	0.8173 0.5331 0.3204
			H2	0.2234 0.2178 0.2065
			H3	0.4375 0.8810 0.1500
			H4	0.5724 -0.0251 0.2318
			He1	0.0000 0.0000 0.7243
C_2	$I4_1md$	a=b= 4.342, c= 6.165	O1	0.0000 0.0000 0.1921
(30 kbar)	4 : 4	α=β=γ = 90	H1	0.0000 0.8155 0.2896
			He1	0.0000 0.0000 0.7087
C_2	$Pna2_1$	a= 4.345, b= 6.146, c= 4.352	O1	0.5062 0.8748 0.0551
(30 kbar)	4 : 4	α=β=γ = 90	H1	0.3160 0.7826 0.0604
			H2	0.5000 0.0330 0.7446
			He1	0.0077 0.8750 0.5717

Phase (Pressure)	Space group # H_2O molecules : # He atoms	Lattice parameters (Å, °)	Atomic coordinates (fractional)	
C_2 (30 kbar)	$P4_12_12$ 4 : 4	a=b= 4.347, c= 6.150 α=β=γ = 90	O1	0.2440 0.2440 0.0000
			H1	0.7502 0.5661 0.5922
			He1	0.7421 0.7421 0.0000
C_3 (90 kbar)	$P4_12_12$ 4 : 8	a=b= 4.921, c= 6.947 α=β=γ = 90	O1	0.7575 0.7575 0.0000
			H1	0.2492 0.4292 0.5909
			He1	0.5052 0.2498 0.8773

Table B.2 *Lattice parameters of fully-filled He hydrate structures (given in Å) relaxed with optPBE-vdW functional at the pressure shown in the bracket and T= 0 K.*

Phase (Pressure)	Space group # H_2O molecules : # Ne atoms	Lattice parameters (Å, °)	Atomic coordinates (fractional)	
C_0 (1 bar)	$P3_2$ 6 : 3	a=b= 6.177, c= 6.054 α=β = 90, γ = 120	O1	0.2342 0.4721 0.8019
			O2	0.7648 0.5306 0.2941
			H1	0.6927 0.0618 0.5684
			H2	0.5735 0.2343 0.8347
			H3	0.3151 -0.0608 0.0757
			H4	0.3476 0.7695 0.2581
			Ne1	-0.0647 0.7868 0.7669
I_h (1 kbar)	$Cmc2_1$ 8 : 4	a= 4.568, b= 7.980, c= 6.894 α=β=γ = 90	O1	0.0000 0.6699 0.0488
			O2	0.0000 0.3377 -0.0557
			H1	0.0000 0.6669 0.1936
			H2	0.0000 0.5500 0.0092
			H3	0.1754 0.2731 -0.0134
			Ne1	0.0000 0.0013 0.7539
I_h (1 kbar)	$Pna2_1$ 8 : 4	a= 4.568, b= 7.980, c= 6.894 α=β=γ = 90	O1	0.0000 0.6699 0.0488
			O2	0.0000 0.3377 -0.0557
			H1	0.0000 0.6669 0.1936
			H2	0.0000 0.5500 0.0092
			H3	0.1754 0.2731 -0.0134
			Ne1	0.0000 0.0013 0.7539
C_1 (10 kbar)	$R\bar{3}$ 36 : 6	a=b= 12.673, c= 6.017 α=β = 90, γ = 120	O1	0.2228 0.1966 0.0454
			O2	0.5236 0.8974 0.1466
			H1	0.8184 0.5344 0.3198
			H2	0.2244 0.2188 0.2045
			H3	0.4384 0.8815 0.1496
			H4	0.5729 -0.0253 0.2297
			Ne1	0.0000 0.0000 0.7361
C_2 (50 kbar)	$I4_1md$ 4 : 4	a=b= 4.409, c= 6.251 α=β=γ = 90	O1	0.0000 0.0000 0.1937
			H1	0.0000 0.8192 0.2898
			Ne1	0.0000 0.0000 0.7066
C_2 (50 kbar)	$Pna2_1$ 4 : 4	a= 4.410, b= 6.239, c= 4.415 α=β=γ = 90	O1	0.0071 0.8747 0.0568
			H1	0.8204 0.7842 0.0624
			H2	-0.0003 0.0348 0.7430
			Ne1	0.5049 0.8750 0.5696
C_2 (50 kbar)	$P4_12_12$ 4 : 4	a=b= 4.412, c= 6.243 α=β=γ = 90	O1	0.2432 0.2432 0.0000
			H1	0.7504 0.5703 0.5905
			Ne1	0.7448 0.7448 0.0000

Table B.3 *Lattice parameters of fully-filled Ne hydrate structures (given in Å) relaxed with optPBE-vdW functional at the pressure shown in the bracket and T= 0 K.*

Phase (Pressure)	Space group # H_2O molecules : # Ar atoms	Lattice parameters (Å, °)	Atomic coordinates (fractional)	
C_0	P1	a= 6.215, b= 6.224, c= 6.284	O1	0.2388 0.2257 0.8010
(1 kbar)	6 : 2	α= 89.88, β = 89.72, γ = 61.02	O2	0.5241 0.2319 0.4676
			O3	0.2525 0.5038 0.1352
			O4	0.7732 0.7550 0.3018
			O5	0.4910 0.7468 -0.0303
			O6	0.7571 0.4758 0.6366
			H1	0.6834 0.3786 0.5772
			H2	-0.0559 0.6802 0.2461
			H3	0.3882 -0.0857 -0.0877
			H4	0.5892 0.6478 0.8451
			H5	0.7621 0.5767 0.5153
			H6	0.6735 0.7515 0.1794
			H7	0.3325 0.5978 0.0809
			H8	0.0669 0.3045 0.7497
			H9	0.6228 0.0615 0.4139
			H10	0.3556 0.4029 0.2560
			H11	0.2409 0.3292 -0.0790
			H12	0.4203 0.2251 0.5860
			Ar1	-0.0695 0.8902 0.7948
			Ar2	0.0958 0.0768 0.2995

Table B.4 *Lattice parameters of partially-filled (with 2/3 cavity occupancy) Ar hydrate structures (given in Å) relaxed with optPBE-vdW functional at the pressure shown in the bracket and T= 0 K.*

Phase (Pressure)	Space group # H_2O molecules : # He atoms	Lattice parameters (Å, °)	Atomic coordinates (fractional)	
C_0	$P3_2$	a=b= 6.289, c= 6.215	O1	0.8939 0.8025 0.4778
(1 bar)	6 : 3	α=β = 90, γ = 120	O2	0.4314 0.8599 -0.0368
			H1	0.7515 0.2157 0.2435
			H2	0.7948 0.2183 0.3542
			H3	0.7243 0.7106 0.4201
			H4	0.8936 -0.0917 0.5964
			H5	0.3295 0.7594 0.8402
			H6	0.6012 -0.0403 -0.0931
I_h	Cc	a= 4.640, b= 8.105, c= 7.082	O1	0.8498 0.1678 0.0511
(1 kbar)	8 : 4	α=β=γ= 90	O2	0.8490 0.1643 0.4448
			H1	0.3209 0.0220 0.2681
			H2	-0.0787 0.4743 0.2095
			H3	0.0308 0.2216 0.0096
			H4	0.8585 0.0510 0.0095
			H5	0.8476 0.1671 0.3046
			H6	0.0254 0.2250 0.4840
C_2	$I4_1md$	a=b= 4.570, c= 6.324	O1	0.00000 0.00000 0.19373
(30 kbar)	4 : 4	α=β=γ = 90	H1	0.00000 0.57999 -0.04485
			H2	0.00000 0.82658 0.28833

Table B.5 *Lattice parameters of fully-filled H_2 hydrate structures (given in Å) relaxed with rPW86-vdW2 functional at the pressure shown in the bracket and T= 0 K.*

Bibliography

[1] "Prof. Singer's research group.", 2017. `https://cbc-wb01x.chemistry.ohio-state.edu/~singer/Hbond.html`.

[2] Amos, D. *High Pressure Hydrates of CO2 Materials for Carbon Storage.* Ph.D. thesis, School of Physics and Astronomy, The University of Edinburgh, 2015.

[3] Amos, D., et al. "A Chiral Gas-Hydrate Structure Common to the Carbon Dioxide-Water and Hydrogen-Water Systems." *J. Phys. Chem. Lett.* 8, 4295-4299.

[4] Antoncik, E. "A new formulation of the method of nearly free electrons." *Czech. J. Phys.* 4, 439.

[5] ———. "Approximate formulation of the orthogonalized plane-wave method." *J. Phys. Chem. Solids* 10, 314.

[6] B. Kamb, A. P., and C. Knobler. "Structure of Ice V." *Acta Crystallogr.* 22: (1967) 706–715.

[7] Bader, F., et al. "Encapsulation of noble gases in hydrates: A LCCSD(T) study with the method of increments." *Proc. Int. CMMSE* .

[8] Baldereschi, A. "Mean-Value Point in the Brillouin Zone." *Phys. Rev. B* 7, 5212.

[9] Bauer, M., et al. "Hexagonal ice transforms at high pressures and compression rates directly into "doubly metastable" ice phases." *J. Chem. Phys.* 131: (2009) 224,514.

[10] Belosludov, R., et al. "Lattice dynamics of helium gas hydrates based on ice framework: dynamic and thermodynamic stability." *Solid State Commun.* 109: (1999) 157–162.

[11] ———. "Accurate description of phase diagram of clathrate hydrates at the molecular level." *J. Chem. Phys.* 131, 244510.

[12] ———. "Stability and Composition of Helium Hydrates Based on Ice Ih and II at Low Temperaturesbility and Composition of Helium Hydrates

Based on Ice Ih and II at Low Temperatures." *J. Phys. Chem. C* 118: (2014) 2587–2593.

[13] Bernal, J., and R. Fowler. "A Theory of Water and Ionic Solution, with Particular Reference to Hydrogen and Hydroxyl Ions." *J. Chem. Phys.* 1, 8: (1933) 515–548.

[14] Bernstein, J. *Polymorphism in Molecular Crystals*. Oxford University Press, 2002.

[15] Birch, F. "Finite Elastic Strain of Cubic Crystals." *Phys. Rev.* 71, 809.

[16] B.J. Murray, D. K., and A. Bertram. "The formatioin of cubic ice under conditions relevant to Earth's atmosphere." *Nature* 10, 434: (2005) 202–205.

[17] Blochl, P. "Projector augmented-wave method." *Phys. Rev. B* 50, 24: (1994) 17,953–17,979.

[18] Bozhko, Y., et al. "Theoretical Investigation of Structures, Compositions and Phase Transitions of Neon Hydrates Based on Ices Ih and II." *J. Eng. Thermophys.* 23, 1: (2014) 20–26.

[19] Bridgman, P. "Water, in the Liquid and Five Solid Forms, under Pressure." *Proc. Am. Acad.* 47, 13.

[20] C. Fiolhais, F. N., and M. Marques. *A Primer in Density Functional Theory*. Springer, 2002.

[21] Ceperley, D., and B. Alder. "Ground State of the Electron Gas by a Stochastic Method." *Phys. Rev. Lett.* 45: (1980) 556–559.

[22] Chachiyo, T. "Communication:Simple and accurate uniform electron gas correlation energy for the full range of densities." *J. Chem. Phys.* 145, 021101.

[23] Cizek, J. "On the Correlation Problem in Atomic and Molecular Systems." *J. Chem. Phys.* 45, 11.

[24] Coester, F. "Bound states of a many-particle system." *Nucl. Phys.* 7, 421.

[25] Cohen, M., and V. Heine. "Cancellation of kinetic and potential energy in atoms, molecules, and solids." *Phys. Rev.* 122, 1821.

[26] Davidson, E., and K. Morokuma. "A proposed antiferroelectric structure for proton ordered ice Ih." *J. Chem. Phys.* 81, 3741.

[27] Dion, M., et al. "Van der Waals Density Functional for General Geometries." *Phys. Rev. Lett.* 92, 24: (2004) 246,401.

[28] Donnelly, M. *Neutron Diffraction of Hydrogen Inclusion Compounds Under Pressure*. Ph.D. thesis, School of Physics and Astronomy, The University of Edinburgh, 2016.

[29] D.R. Hamann, M. S., and C. Chiang. "Norm-consering pseudopotentials." *Phys. Rev. Lett.* 43: (1979) 1494–1497.

[30] Dubrovinskaia, N., et al. "Terapascal Static Pressure Generation with Ultrahigh Yield Strength Nanodiamond." *Sci. Adv.* 2, 7.

[31] Dubrovinsky, L., et al. "The Most Incompressible Metal Osmium at Static Pressure above 750 Gigapascals." *Nature* 525, 7568: (2015) 226–229.

[32] Dyadin, Y., et al. "Clathrate formation in water-noble gas (hydrogen) system at high pressure." *J. Struct. Chem.* 40, 5: (1999) 790–795.

[33] ———. "Clathrate hydrate of hydrogen and neon." *Mendeleev Commun.* 9, 5: (1999) 209–210.

[34] E. Hult, H. R., and B. Lundqvist. "Unified treatment of aymptotic van der Waals forces." *Phys. Rev. B* 59, 7: (1999) 4708–4713.

[35] E. Whalley, D. D., and J. Heath. "Dielectric Properties of Ice VII. Ice VII: A New Phase of Ice." *J. Chem. Phys.* 45, 11: (1966) 3976–3982.

[36] E.D. Sloan, J. "Fundametal principles and applications of natural gas hydrates." *Nature* 426: (2003) 353–359.

[37] Efimchenko, V., et al. "New phase in the water-hydrogen system." *J. Alloy Compd.* 509: (2011) 860–863.

[38] Engelhardt, H., and E. Whalley. "Ice IV." *J. Chem. Phys.* 56, 6: (1972) 2678–2684.

[39] Erba, A., et al. "DFT and Local-MP2 Periodic Study of the Structure and Stability of Two Proton-Ordered Polymorphs of Ice." *J. Phys. Chem. B* 113: (2009) 2347–2354.

[40] F. Ortmann, F. B., and W. Schmidt. "Semiempirical van der Waals correction to the density functional description of solids and molecular structures." *Phys. Rev. B* 73, 205101.

[41] Falenty, A., et al. "Formation and properties of ice XVI obtained by emptying a type sII clathrate hydrate." *Nature* 516, 231-233.

[42] Finch, E., et al. "Neutron-Diffraction Study of Ice Polymorphs. II. Ice II." *J. Chem. Phys.* 49, 10: (1968) 4361–4365.

[43] Fock, V. "Näherungsmethode zur Lösung des quantenmechanischen Mehrkörperproblems." *Z. Phys. A* 61, 126.

[44] Fortes, A., I. Wood, J. Brodholt, and L. Vocadlo. "Ab initio simulation of the ice II structure." *J. Chem. Phys.* 119: (2003) 4567.

[45] Frisch, M., et al. "Gaussian09 Revision D.01." Gaussian Inc. Wallingford CT 2009, 2009.

[46] Fuentes-Landete, V., et al., editors. *Crystalline and amorphous ices.* Proceedings of the International School of Physics, 2015.

[47] G. Henkelman, H. J., B.P. Uberuaga. "A Climbing image nudged elastic band method for finding saddle points and minimum energy paths." *J. Chem. Phys.* 113.

[48] Giauque, W., and J. Stout. "The entropyof water and the third law of thermodynamics. The heat capacity of ice from 15 to 273 K." *J. Am. Chem. Soc.* 58: (1936) 1144.

[49] Grimme, S. "Accurate Description of van der Waals Complexes by Density Functional Theory Including Empirical Corrections." *J. Comput. Chem.* 25, 12: (2004) 1463–1473.

[50] ———. "Semiempirical GGA-Type Density Functional Constructed with a Long-Range Dispersion Correction." *J. Comput. Chem.* 27: (2006) 1787–1799.

[51] Guillot, T. "Interiors of Giant Planets Inside and Outside the Solar System." *Science* 286, 5437: (1999) 72–77.

[52] H. Fukazawa, S. I., and S. Mae. "Incoherent inelastic neutron scattering measurements on ice XI: the proton-ordered phase of ice Ih doped with KOH." *Chem. Phys. Lett.* 282: (1998) 215.

[53] Hakim, L., K. Koga, and H. Tanaka. "Novel neon-hydrate of cubic ice structure." *Physica A* 389: (2010) 1834–1838.

[54] Handa, Y., D. Klug, and E. Whalley. "Difference in energy between cubic and hexagonal ice." *J. Chem. Phys.* 84, 12: (1986) 7009–7010.

[55] Hartree, D. "The Wave Mechanics of an Atom with a Non-Coulomb Central Field. Part I." *Math. Proc. Cambridge Philos. Soc.* 24, 03: (1928) 426.

[56] ———. "The Wave Mechanics of an Atom with a Non-Coulomb Central Field. Part II." *Math. Proc. Cambridge Philos. Soc.* 24, 01: (1928) 111.

[57] Henkelman, G., et al. "A Climbing image nudged elastic band method for finding saddle points and minimum energy paths." *J. Chem. Phys.* 113, 9901.

[58] Hermann, A. *Electronic Structure Theory.* Lecture note, 2017.

[59] ———. *Review in computational chemistry: Chemical bonding at high pressure*, volume 30. Wiley, 2017.

[60] Hermann, A., N. Ashcroft, and R. Hoffmann. "High pressure ices." *Proc. Natl. Acad. Sci. U.S.A.* 109: (2012) 745–750.

[61] ———. "Isotopic differentiation and sublattice melting in dense dynamic ice." *Phys. Rev. B* 88, 214113: (2013) 214,113.

[62] Hermann, A., and P. Schwerdtfeger. "Ground-State Properties of Crystalline Ice from Periodic Hartree-Fock Calculations and a Coupled-Cluster-Based Many-Body Decomposition of the Correlation Energy." *Phys. Rev. Lett.* 101, 183005: (2008) 183,005.

[63] ———. "Blueshifting the Onset of Optical UV Absorption for Water under Pressure." *Phys. Rev. Lett.* 106, 187403: (2011) 187,403.

[64] Herring, W. "A new method for calculating wave functions in crystals." *Phys. Rev.* 57, 1169.

[65] Herring, W., and A. Hill. "The theoretical constitution of metallic beryllium." *Phys. Rev.* 58, 132.

[66] Hirai, H. "Phase changes of CO2 hydrate under pressure and low temperture." *J. Chem. Phys.* 133, 12.

[67] Hirai, H., et al. "Pressure-induced phase changes of argon hydrate and methane hydrate at room temperature." *P. Jpn. Acad. B-Phys.* 78, 3: (2002) 39–44.

[68] ———. "Structural Changes of Argon Hydrate under High Pressure." *J. Phys. Chem. B* 106, 43: (2002) 11,089–11,092.

[69] Hirsch, T., and L. Ojamae. "Quantum-Chemical and Force-Field Investigations of Ice Ih: Computational of Proton-Ordered Structures and Presiction of Their Lattice Energies." *J. Phys. Chem. B* 108, 15856-15864.

[70] Hobbs, P. *Ice Physics*. Oxford Classic Texts in the Physical Sciences Oxford Classic. Oxford University Press, 2010.

[71] Hohenberg, P., and W. Kohn. "Inhomogeneous Electron Gas." *Phys. Rev.* 136, 3B: (1964) 864–871.

[72] Holzwarth, N., et al. "Comparison of the projector augmented-wave, pseudopotential, and linearized augmented-plane-wave formalisms for density-functional calculations of solids." *Phys. Rev. B* 55: (1997) 2005–2017.

[73] J.E. Bertie, L. C., and E. Whalley. "Transformations of ice VI and ice VII at atmosperic pressure." *Can. J. Chem.* 42, 6: (1964) 1373–1378.

[74] Jonsson, H., et al. "Nudged elastic band method for finding minimum energy paths of transitions." *Lecture Note Chapter 16* .

[75] Jr., E. S., and C. Koh. *Clathrate Hydrate of Natural Gases.* Chemical Industries. CRC Press, 2007, third edition.

[76] K. Berland, K. L. E. S. T. T. P. H., V.R. Cooper, and B. Lundqvist. "van der Waals forces in density functional theory: a review of the vdW-DF method." *Rep. Prog. Phys.* 78, 066501.

[77] Kamb, B. "Ice II: A Proton-Ordered Form of Ice." *Acta Crystallogr.* 17: (1964) 1437–1449.

[78] ———. "Structure of Ice VI." *Science* 150, 3693: (1965) 205–209.

[79] Kamb, B., and B. Davis. "Ice VII, The densest form of ice." *Proc. Natl. Acad. Sci. U.S.A.* 52: (1964) 1433–1439.

[80] Kamb, B., W. Hamilton, S. Laplaca, and A. Prakash. "Ordered Proton Configuration in Ice II, from Single-Crystal Neutron Diffraction." *J. Chem. Phys.* 55, 4: (1971) 1934–1945.

[81] Kamb, B., and A. Prakash. "Structure of Ice III." *Acta Crystallogr.* 24: (1968) 1317–1327.

[82] Kawada, S. "Dielectric dispersion and phase transition of KOH doped ice." *J. Phys. Soc. Jpn.* 32, 5: (1972) 1442.

[83] Klimes, et al. *J. Phys.: Cond. Matt.* 22, 022201.

[84] Klimes, J., D. Bowler, and A. Michaelides. "Van der Waals density functionals applied to solids." *Phys. Rev. B* 83, 19: (2011) 195,131.

[85] Klimes, J., and A. Michaelides. "Perspective: Advances and challenges in treating van der Waals dispersion forces in density functional theory." *J. Chem. Phys.* 137, 120901.

[86] Klotz, S., et al. "Metastable ice VII at low temperature and ambient pressure." *Nature* 398: (1999) 681–684.

[87] Knight, C., and S. Singer. "Prediction of a Phase Transition to a Hydrogen Bond Ordered Form of Ice VI." *J. Phys. Chem. B* 109, 44: (2005) 21,040–21,046.

[88] ———. "A re-examination of the ice III/IX hydrogen bond ordering phase transition." *J. Chem. Phys.* 125, 6: (2006) 064,506.

[89] ———. "Hydrogen bond ordering in ice V and the transition to ice XIII." *J. Chem. Phys.* 129, 16: (2008) 164,513.

[90] Knight, C., et al. "Hydrogen bond topology and the ice VII/VIII and Ih/XI proton ordering phase transitions." *Phys. Rev. E* 73: (2006) 056,113.

[91] Kohn, W., and L. Sham. "Self-Consistent Equations Including Exchange and Correlation Effects." *Phys. Rev.* 140, 4A: (1965) 1133–1138.

[92] Koster, K., et al. "Dynamics enhanced by HCL doping triggers full Pauling entropy release at the ice XII-XIV transition." *Nature Commun.* 6, 7349.

[93] Kresse, G., and J. Furthmuller. "Efficient iterative schemes for ab initio total-energy calculations using a plane-wave basis set." *Phys. Rev. B* 54, 16: (1996) 11,170–11,186.

[94] Kresse, G., and D. Joubert. "From ultrasoft pseudopotentials to the projector augmented-wave method." *Phys. Rev. B* 59, 3: (1999) 1758–1775.

[95] Kuhs, W., et al. "Structure and hydrogen ordering in ices VI, VII, and VIII by neutron power diffraction." *J. Chem. Phys.* 81, 8: (1984) 3612–3623.

[96] ———. "Cage occupancy and compressibility of deuterated N2-Clathrate hydrate by neutron diffraction." *J. Inclusion. Phenom.* 29: (1997) 65–77.

[97] Kuo, J., and S. Singer. "Graph invariants for periodic systems: Towards predicting physical properties from the hydrogen bond topology of ice." *Phys. Rev. E* 67, 1: (2003) 016,114.

[98] Kuo, J., et al. "On the use of graph invariants for efficiently generating hydrogen bond topologies and predicting physical properties of water clusters and ice." *J. Chem. Phys.* 114, 6: (2001) 2527–2540.

[99] L.D. Rosso, M. C., and L. Ulivi. "New porous water ice metastable at atmospheric pressure obtained by emptying a hydrogen-filled ice." *Nature Commun.* 7, 13394.

[100] Lee, K., et al. "Higher-accuracy van der Waals density functional." *Phys. Rev. B* 82, 081101.

[101] Lobban, C., J. Finney, and W. Kuhs. "The structure and ordering of ices III and V." *J. Chem. Phys.* 112, 16: (2000) 7169–7180.

[102] ———. "The p-T dependency of the ice II crystal structure and the effect of helium inclusion." *J. Chem. Phys.* 117, 8: (2002) 3928–3934.

[103] Lokshin, K., et al. "Structure and Dynamics of Hydrogen Molecules in the Novel Clathrate Hydrate by High Pressure Neutron Diffraction." *Phys. Rev. Lett.* 93, 12: (2004) 125,503.

[104] Londono, D., J. Finney, and W. Kuhs. "Formation, stability, and structure of helium hydrate at high pressure." *J. Chem. Phys.* 97, 1: (1992) 547–552.

[105] Londono, D., W. Kuhs, and J. Finney. "Enclathration of helium in ice II: the first helium hydrate." *Nature* 332: (1988) 141–142.

[106] Loveday, J., and R. Nelmes. "High-pressure gas hydrate." *Phys. Chem. Chem. Phys.* 10: (2008) 937–950.

[107] Manakov, A., et al. "Argon Hydrates: Structural Studies at High Pressures." *Phys. Chem.* 378: (2001) 148–151.

[108] ———. "Structural Investigations of Argon Hydrates at Pressures up to 10 kbar." *J. Inclusion. Phenom.* 48: (2004) 11–18.

[109] Mao, W., et al. "Hydrogen Clusters in Clathrate Hydrate." *Science* 297, 5590: (2002) 2247–2249.

[110] Martin, R. *Electronic Structure: Basic Theory and Practical Methods.* Cambridge University Press, 2012.

[111] McFarlan, R. "The Structure of Ice III." *J. Chem. Phys.* 4, 253.

[112] Moller, C., and M. Plesset. "Note on an Approximation Treatment for Many-Electron Systems." *Phys. Rev.* 46, 618.

[113] ———. "Note on an Approximation Treatment for Many-Electron Systems." *Phys. Rev.* 46, 618.

[114] Monkhorst, H., and J. Pack. "Special points for Brillouin-zone integrations." *Phys. Rev. B* 13, 12: (1976) 5188–5192.

[115] van Mourik, T., and R. Gdanitz. "A critical note on density functional theory studies on rare-gas dimers." *J. Chem. Phys.* 116, 22: (2002) 9620–9623.

[116] Muller, C., and B. Paulus. "Wavefunction-based electron correlation methods for solids." *Phys. Chem. Chem. Phys.* 14: (2012) 7605–7614.

[117] ———. "Wavefunction-based electron correlation methods for solids." *Phys. Chem. Chem. Phys.* 14: (2012) 7605–7614.

[118] Murnaghan, F. "The Compressibility of Media under Extreme Pressures." *Proc. Natl. Acad. Sci. U.S.A.* 30, 9: (1944) 244–247.

[119] Nagle, J. "Lattice statistics of hydrogen bonded crystals. I. The residual entropy of ice." *J. Math. Phys.* 7, 8: (1966) 1484.

[120] Oganov, A., and C. Glass. "Crystal structure prediction using ab initio evolutionary techniques: Principles and applications." *J. Chem. Phys.* 124.

[121] Pauling, L. "The Structure and Entropy of Ice and of Other Crystals with Some Randomness of Atomic Arrangement." *J. Am. Chem. Soc.* 57, 12: (1935) 2680–2684.

[122] Perdew, J., K. Burke, and M. Ernzerhof. "Generalized Gradient Approximation Made Simple." *Phys. Rev. Lett.* 77, 18: (1996) 3865–3868.

[123] Perdew, J., and A. Zunger. "Self-interaction correction to density-functional approximations for many-electron systems." *Phys. Rev. B* 23: (1981) 5048–5079.

[124] Philips, J., and L. Kleinman. "New method for calculating wave functions in crystals and molecules." *Phys. Rev.* 116, 287.

[125] Qian, G., et al. "Novel Hydrogen Hydrate Structures under Pressure." *Sci. Rep.* 4, 5606: (2014) 5606.

[126] Quapp, W. "Comment "On the quadratic reaction path evaluated in a reduced potential energy surface model and the problem to locate transition states"." *J. Comput. Chem.* 22, 537.

[127] Quapp, W., and J. Bofill. "A comment to the Nudged Elastic Band Method.", 2010. `www.math.uni-leipzig.de/~quapp/mTasc.html`.

[128] Rapcewicz, K., and N. Ashcroft. "Fluctuation attraction in condensed matter: A nonlocal functional approach." *Phys. Rev. B* 44, 8: (1991) 4032–4035.

[129] Raza, Z., et al. "Proton ordering in cubic ice and hexagonal ice: a potential new ice phase-XIc." *Phys. Chem. Chem. Phys.* 13: (2011) 19,788–19,795.

[130] Roman-Perez, G., and J. Soler. "Efficient Implementation of a van der Waals Density Functional: Application to Double-Wall Carbon Nanotubes." *Phys. Rev. Lett.* 103, 096102.

[131] del Rosso, L., et al. "Refined Structure of Metastable Ice XVII from Neutron Diffraction Measurements." *J. Phys. Chem. C* 120, 26955-26959.

[132] S. Grimme, S. E., J. Antony, and H. Krieg. "A consistent and accurate ab initio parametrization of density functional dispersion correction (DFT-D) for 94 elements H-Pu." *J. Chem. Phys.* 132, 154104.

[133] Salzmann, C., P. Radaelli, E. Mayer, and J. Finney. "Ice XV: A New Thermodynamically Stable Phase of Ice." *Phys. Rev. Lett.* 103: (2009) 105,701.

[134] Salzmann, C., et al. "The Preparation and Structures of Hydrogen Ordered Phases of Ice." *Science* 311: (2006) 1758–1761.

[135] ———. "Detailed crystallographic analysis of the ice VI to ice XV hydrogen ordering phase transition." *J. Chem. Phys.* 145, 204501.

[136] Santra, B., et al. "Hydrogen Bonds and van der Waals Forces in Ice at Ambient and High Pressures." *Phys. Rev. Lett.* 107, 18: (2011) 185,701.

[137] ———. "On the Accuracy of van der Waals Inclusive Density-Functional Theory Exchange-Correlation Functionals for Ice at Ambient and High Pressures." *J. Chem. Phys.* 139: (2013) 154,702.

[138] Schwager, B., et al. "Melting curve of H2O to 90 GPa measured in a laser-heated diamond cell." *J. Phys.: Cond. Matt.* 16: (2004) s1177–s1179.

[139] Sheppard, D., et al. "Optimization methods for finding minimum energy paths." *J. Chem. Phys.* 128, 134106.

[140] Shimizu, H., et al. "Optical microscopy and Raman scattering of a single crystalline argon hydrate at high pressures." *Chem. Phys. Lett.* 368: (2003) 132–138.

[141] Sinanoglu, O. "Many-Electron Theory of Atoms and Molecules. I. Shells, Electron Pairs vs Many-Electron Correlations." *J. Chem. Phys.* 36, 2.

[142] Singer, S., et al. "Hydrogen-Bond Topology and the Ice VII/VIII and Ice Ih/XI Proton-Ordering Phase Transitions." *Phys. Rev. Lett.* 94: (2005) 135,701.

[143] ———. "Hydrogen-Bond Topology and the Ice VII/VIII and Ice Ih/XI Proton-Ordering Phase Transitions." *Phys. Rev. Lett.* 94: (2005) 135,701.

[144] Slater, J. "The Theory of Complex Spectra." *Phys. Rev.* 34, 10: (1929) 1293–1322.

[145] Smirnov, G., and V. Stegailov. "Toward Determination of the New Hydrogen Hydrate Clathrate Structures." *Journal of Physical Chemistry Letters* 4: (2013) 3560–3564.

[146] v. Stackelberg, V. M. "Feste Gashydrate." *Naturwissenschaften* 36: (1949) 327–333.

[147] Stoll, H. "On the correlation energy of graphite." *J. Chem. Phys.* 97: (1992) 8449–8454.

[148] Strobel, T., M. Somayazulu, and R. Hemley. "Phase Behavior of H2 + H2O at High Pressures and Low Temperatures." *J. Phys. Chem. C* 115: (2011) 4898–4903.

[149] Strobel, T., et al. *Chem. Phys. Lett.* 478, 4: (2009) 97–109.

[150] ———. "Toward Determination of the New Hydrogen Hydrate Clathrate Structures." *J. Am. Chem. Soc.* 138, 13786-13789.

[151] T. Thonhauser, S. L. A. P. P. H., V.R. Cooper, and D. Langreth. "Van der Waals density functional: Self-consistent potential and the nature of the van der Waals bond." *Phys. Rev. B* 76, 125112.

[152] Tajima, Y., T. Matsuo, and H. Suga. "Phase transition in KOH-doped hexagonal ice." *Nature* 299: (1982) 810–812.

[153] Teeratchanan, P., and A. Hermann. "Computational phase diagrams of noble gas hydrates under pressure." *J. Phys. Chem.* 143.

[154] T.H. Dunning, J. "Gaussian basis sets for use in correlated molecular calculations. I. The atoms boron through neon and hydrogen." *J. Chem. Phys.* 90: (1989) 1007–1023.

[155] Tkatchenko, A., J. R.A. DiStasio, R. Car, and M. Scheffler. "Accurate and Efficient Method for Many-Body van der Waals Interactions." *Phys. Rev. Lett.* 108, 23: (2012) 236,402.

[156] Tkatchenko, A., and M. Scheffler. "Accurate Molecular Van Der Waals Interactions from Ground-State Electron Density and Free-Atom Reference Data." *Phys. Rev. Lett.* 102, 073005.

[157] Tonkov, E., and E. Ponyatovsky. *Phase Transformations of Elements Under High Pressure.* CRC Press, 2004.

[158] Troullier, N., and J. Martins. "Efficient pseudopotentials for plane-wave calculations." *Phys. Rev. B* 43: (1991) 1993–2006.

[159] Tse, J., Y. Handa, C. Ratcliffe, and B. Powell. "Structure of Oxygen Clathrate Hydrate by Neutron Powder Diffraction." *J. Inclusion. Phenom.* 4: (1986) 235–240.

[160] Tyagi, A., and S. Banerjee. *Materials Under Extreme Conditions (Recent Trends and Future Prospects).* Elsevier, 2017.

[161] Vanderbilt, D. "Soft self-consistent pseudopotentials in a generalized eigenvalue formalism." *Phys. Rev. B* 41, 11.

[162] V.F. Petrenko, R. W. *Physics of Ice.* Oxford University Press, 1999.

[163] V.G. Ruiz, E. Z. M. S., W. Liu, and A. Tkatchenko. "Density-Functional Theory with Screened van der Waals Interactions for Modeling of Hybrid Inorganic-Organic Systems." *Phys. Rev. Lett.* 108, 146103.

[164] Vinet, P., et al. "A universal equation of state for solids." *J. Phys. C. Solid State Phys.* 19, 20.

[165] Vos, W., L. Finger, R. Hemley, and H. Mao. "Pressure dependence of hydrogen bonding in a novel H2O-H2 Clathrate." *Chem. Phys. Lett.* 257: (1996) 524–530.

[166] Vos, W., et al. "Novel H2-H2O Clathrates at High Pressures." *Phys. Rev. Lett.* 71, 19: (1993) 3150–3153.

[167] Vydrov, O., and T. Voorhis. "Nonlocal van der Waals Density Functional Made Simple." *Phys. Rev. Lett.* 103, 06004.

[168] ———. "Dispersion interactions from a nonlocal polarizability model." *Phys. Rev. A* 81, 062708.

[169] Wang, Y., and J. Perdew. "Correlation hole of the spin-polarized electron gas, with exact small-wave-vector and high-density scaling." *Phys. Rev. B* 44: (1991) 13,298–13,307.

[170] Wheatley, J. "Experimental properties of superfluid He3." *Rev. Mod. Phys.* 47, 415.

[171] Wigner, E. "On the interaction of electrons in metals." *Phys. Rev. Lett.* 46: (1934) 1002–1011.

[172] Wilks, J. *The Properties of Liquid and Solid Helium*. Oxford University Press, 1967.

[173] Woon, D., and J. T.H. Dunning. "Gaussian basis sets for use in correlated molecular calculations. III. The second row atoms, Al-Ar." *J. Chem. Phys.* 98: (1993) 1358–1371.

[174] Y. Andersson, D. L., and B. Lundqvist. "van der Waals Interaction in Density-Functional Theory." *Phys. Rev. Lett.* 76, 1: (1996) 102–105.

[175] Young, A. *Phase diagrams of the Elements*. Oxford University Press, 1990.

[176] Yu, X., et al. "Crystal structure and encapsulation dynamics of ice II-structured neon hydrate." *Proc. Natl. Acad. Sci. U.S.A.* 111, 29: (2014) 10,456–10,461.

[177] Zhang, Y., and W. Yang. "Comment on Gerneralized Gradient Approximation Made Simple." *Phys. Rev. Lett.* 80, 4: (1998) 890.